DESY-THESIS-1999-011
January 1999

Inaugural - Dissertation

zur
Erlangung der Doktorwürde
der
Naturwissenschaftlich-Mathematischen
Gesamtfakultät
der
Ruprecht-Karls-Universität
Heidelberg

vorgelegt von
Thorsten Wengler, MA
aus Elsterwerda

Tag der mündlichen Prüfung: 27. Januar 1999

Measurement of π°-Meson Cross Sections at low Bjorken-x in Deep-Inelastic ep - Collisions at $\sqrt{s} = 300$ GeV

Gutachter: Prof. Dr. Franz Eisele
Prof. Dr. Otto Nachtmann

Abstract

High p_T π°-meson production cross sections for small polar angles θ_π with respect to the incident proton direction have been measured in deep-inelastic positron-proton scattering at low Bjorken-x. The analysis is based on an integrated luminosity of 5.8 pb^{-1} taken with the H1 detector at HERA in 1996. The π° cross sections are measured as a function of Q^2, as a function of x, and as a function of the transverse momentum $p_{T,\pi}$ and pseudorapidity η_π of the π°-mesons. The measurement extends over two orders of magnitude in x down to $x \approx 5{\cdot}10^{-5}$. High p_T particle production is shown to be strongly correlated to the underlying parton dynamics. The π° cross sections exhibit a strong rise towards low x and Q^2. The relative rate of π°-meson production in DIS events is determined and shows no dependence on x, but decreases with decreasing Q^2 for fixed x. Calculations using $\mathcal{O}(\alpha_s)$ QCD matrix elements and DGLAP-like parton cascades cannot describe the π° cross sections at low x. Including processes where the virtual photon is resolved leads to an improved description of the data. Renormalization and factorization scale uncertainties however limit the precision of the predictions especially for the resolved contributions. A calculation within the BFKL formalism is in good agreement with the data, implying that this approach is a valid approximation of QCD in the considered phase space.

Messung von π°-Meson-Wirkungsquerschnitten bei kleinen Bjorken-x in tief-inelastischen ep - Kollisionen mit $\sqrt{s} = 300$ GeV

Zusammenfassung

Vorgestellt werden Wirkungsquerschnitte für die Produktion von π°-Mesonen mit hohem transversalen Impuls und unter kleinen Winkeln zur Richtung des einlaufenden Protons in tief-inelastischer Positron-Proton Streuung bei kleinen Bjorken-x. Die Messung basiert auf einer Datenmenge von 5.8 pb^{-1}, die 1996 mit dem H1-Detektor an der Beschleunigeranlage HERA aufgezeichnet wurde. Die π° Wirkungsquerschnitte wurden gemessen als Funktion von Q^2 und Bjorken-x sowie als Funktion des transversalen Impulses $p_{T,\pi}$ und der Pseudorapidität η_π der π°-Mesonen. Die Produktion von Teilchen mit hohem Transversalimpuls ist stark korreliert zur Dynamik des partonischen Endzustandes. Die Messung erreicht Werte von $x \gtrsim 5{\cdot}10^{-5}$ und erstreckt sich über zwei Größenordnungen in x. Die Wirkungsquerschnitte zeigen einen starken Anstieg zu kleinen Q^2 und x. Die relative Rate der π°-Produktion in tief-inelastischen Streuereignissen ist nicht von x abhängig, sinkt aber mit kleiner werdendem Q^2 für festes x. Berechnungen unter Benutzung von $\mathcal{O}(\alpha_s)$ Matrixelementen und DGLAP-Partonkaskaden sind nicht kompatibel mit den Daten. Die zusätzliche Berücksichtigung von Prozessen, bei denen die hadronischen Eigenschaften des virtuellen Photons aufgelöst werden, führt zu einer besseren Beschreibung der gemessenen Verteilungen. Die Aussagekraft wird hierbei aber durch eine starke Abhängigkeit dieser Beiträge von der Wahl der Renormierungs- und Faktorisierungsskala begrenzt. Eine Rechnung im Rahmen des BFKL-Formalismus ist in guter Übereinstimmung mit den gemessenen Werten und impliziert damit die Gültigkeit dieser Näherungslösung der QCD im betrachteten Phasenraum.

To my parents and to Joannah.

Uncertainty,
in the presence of vivid hopes and fears,
is painful,
but must be endured
if we wish to live
without the support
of comforting fairy tales.

Bertrand Russel

Contents

Introduction **1**

1 The Theory of Deep-Inelastic Scattering **3**

1.1 Kinematical Variables in DIS 3

1.2 The Cross Section for Deep-Inelastic ep Scattering 5

1.3 The Quark-Parton Model 6

1.4 Partons in Quantum Chromodynamics 8

1.5 The DGLAP Evolution Equations 13

1.6 The BFKL Equation 15

1.7 The CCFM Equation and the Linked Dipole Chain Model 16

1.8 The Merits of High p_T Particle Observables 18

1.9 QCD Models 22

2 The ep Collider HERA **26**

3 The H1 Detector **28**

3.1 Tracking 30

3.2 Calorimetry 33

3.3 Luminosity System and Time of Flight Counters 37

3.4 Triggering and Data Acquisition 40

3.5 Detector Simulation 41

4 The Selection of Deep-Inelastic Scattering Events **42**

4.1 Basic Selection of the ep Data Sample 42

4.2 The available DIS Phase Space at low Q^2 43

4.3 Identification of the Scattered Positron 44

5 Identification of Neutral Pions **49**
5.1 The π° Phase Space 49
5.2 Selection Strategy 50
5.3 Shower Shape Estimators 53
5.4 Modeling of the Detector Response 58
5.5 Efficiency, Purity and Resolution of the selected π° Sample 64

6 Measurement of Neutral Pion Production Cross Sections **67**
6.1 The Observables 68
6.2 Trigger Efficiency for Events containing a π° Candidate 69
6.3 The Unfolding Procedure 74
6.4 Background and Systematic Uncertainties 80
6.5 Results 84

7 Interpretation **89**
7.1 The Relative Rate of π° Production 90
7.2 Phenomenological QCD Models 90
7.3 BFKL Calculation in Order $\mathcal{O}(\alpha_s)$ and Fragmentation Functions . . . 91
7.4 Comparisons to the Data 92

Summary **99**

A Cross Sections **101**

B Variation of Model Parameters **106**

Bibliography **111**

Acknowledgments **115**

List of Tables

4.1 Quality criteria for the selection of DIS events. 48

5.1 Phase space for the measurement of forward π° cross sections. 50
5.2 Shower shape conditions for the π° selection. 58
5.3 The number of clusters left in each cluster class when successively applying the shower shape cuts. 61

6.1 Summary of quantities measured. 68
6.2 Setup of trigger s002 for 1996 70
6.3 Summary of systematic uncertainties. 83

A.1 The numerical values of the differential π° cross section as a function of Q^2 for $p_{T,\pi} > 2.5$ GeV as shown in Figure 6.11. 101
A.2 The numerical values of the differential π° cross section as a function of x for $p_{T,\pi} > 2.5$ GeV in three regions of Q^2 as shown in Figure 6.9. 102
A.3 The numerical values of the differential π° cross section as a function of $p_{T,\pi}$ for $p_{T,\pi} > 2.5$ GeV in three regions of Q^2 as shown in Figure 6.10 (a). 103
A.4 The numerical values of the differential π° cross section as a function of η_π for $p_{T,\pi} > 2.5$ GeV in three regions of Q^2 as shown in Figure 6.10 (b). 104
A.5 The numerical values of the differential π° cross section as a function of x for $p_{T,\pi} > 3.5$ GeV as shown in Figure 6.12 (a). 105
A.6 The numerical values of the differential π° cross section as a function of Q^2 for $p_{T,\pi} > 3.5$ GeV as shown in Figure 6.12 (b). 105

List of Figures

1.1 Four-vectors used to construct Lorentz-invariant kinematical quantities in deep-inelastic scattering. 4
1.2 The quark-parton model 6
1.3 The proton structure function $F_2^P(x, Q^2)$ 9
1.4 Gluon radiation and scaling violations 11
1.5 Factorization of the ep cross section 12
1.6 Feynman graphs for splitting functions. 14
1.7 Ladder diagram to visualize the parton evolutions in QCD. 15
1.8 The LDC model: fan diagram for a DIS event with n initial emissions. 17
1.9 The transverse energy flow as a function of pseudorapidity in the hadronic cms. 18
1.10 Forward jet cross sections 19
1.11 Parton jet – π°-meson correlations. 21
1.12 Tree level diagrams for γP scattering. 22
1.13 Parton cascades in deep-inelastic scattering 23
1.14 Fragmentation models. 24

2.1 Schematic overview of the HERA accelerator complex. 27

3.1 An isometric view of the H1 collider detector at HERA. 29
3.2 Side view of the H1 tracking system. 30
3.3 Schematic outlay of the four BDC double layers. 32
3.4 Side view of the liquid argon calorimeter. 33
3.5 Position of the di-photon invariant mass peak before and after the correction for uninstrumented material. 34
3.6 Calibration of electromagnetic energies for the scattered positron. . . 36
3.7 Side view of the backward region of the H1 detector. 37

3.8 The H1 luminosity system. 38

4.1 The kinematic plane in terms of the invariant quantities Q^2 and x. . . 43
4.2 Distributions of variables used in the selection of the scattered positron. 45
4.3 Properties of the scattered positron. 46
4.4 Distribution of the z coordinate of the primary event vertex and the distribution of $\sum (E - p_z)$ 47

5.1 Opening angle of two photons from the reaction $\pi^\circ \to 2\gamma$. 51
5.2 Energy depositions in the LAr calorimeter of a two photon configuration from a π° decay. 52
5.3 The shower shape estimators Ω_{em} and Ω_{hc} for the signal, background, and hybrid class of clusters. 54
5.4 The shower shape estimators Ω_{td} and Ω_{le} for the signal, background and hybrid class of clusters. 56
5.5 Correlations of the shower shape estimators. 57
5.6 The effect of reweighting the simulated events on the shower shape estimators Ω_{hc} and Ω_{td} 59
5.7 The effect of reweighting the simulated events on the shower shape estimators Ω_{em} and Ω_{le} 60
5.8 Transverse Energy and pseudorapidity of π° candidate clusters 61
5.9 Behavior of the estimator Ω_{hc} with the successive application of the selection cuts. 62
5.10 The shower shape estimators after the application of all selection cuts. 63
5.11 Transverse energy flow around cluster candidates. 64
5.12 Angular and transverse momentum resolution for π°-mesons after all selection cuts. 65

6.1 Stability of trigger s002. 71
6.2 Efficiency of trigger s002 for $d\sigma_\pi/dx$, $d\sigma_\pi/d\eta_\pi$ and $d\sigma_\pi/dp_{T,\pi}$. 72
6.3 Efficiency of trigger s002 for $d\sigma_\pi/dQ^2$ ($p_{T,\pi} > 2.5$ GeV), and for the higher threshold of $p_{T,\pi} > 3.5$ GeV for $d\sigma_\pi/dQ^2$ and $d\sigma_\pi/dx$ 73
6.4 Bin migrations for $d\sigma_\pi/dx$, $d\sigma_\pi/d\eta_\pi$ and $d\sigma_\pi/dp_{T,\pi}$. 76
6.5 Bin migrations for $d\sigma_\pi/dQ^2$ ($p_{T,\pi} > 2.5$ GeV), and for the higher threshold of $p_{T,\pi} > 3.5$ GeV for $d\sigma_\pi/dQ^2$ and $d\sigma_\pi/dx$. 77
6.6 Correction functions for $d\sigma_\pi/dx$, $d\sigma_\pi/d\eta_\pi$ and $d\sigma_\pi/dp_{T,\pi}$. 78

6.7 Correction functions for $d\sigma_\pi/dQ^2$ ($p_{T,\pi} > 2.5$ GeV), and for the higher threshold of $p_{T,\pi} > 3.5$ GeV for $d\sigma_\pi/dQ^2$ and $d\sigma_\pi/dx$. 79
6.8 The two photon invariant mass distribution before and after recalibration. 81
6.9 Differential π°-meson production cross sections as a function of x in three regions of Q^2. 85
6.10 Differential π°-meson production cross sections as a function of $p_{T,\pi}$ and η_π in three regions of Q^2. 86
6.11 Differential π°-meson production cross sections as a function of Q^2. . 87
6.12 Differential π°-meson production cross sections as a function of Q^2 and x for $p_{T,\pi} > 3.5$ GeV. 88

7.1 Differential π°-meson production cross sections and the rate of π° production in DIS events as a function of x in three regions of Q^2. . . 93
7.2 Differential π°-meson production cross sections as a function of $p_{T,\pi}$ and η_π in three regions of Q^2. 94
7.3 Differential π°-meson production cross sections and the rate of π° production in DIS events as a function of Q^2. 96
7.4 Differential π°-meson production cross sections and the rate of π° production in DIS events as a function of Q^2 and x. 98

B.1 The effect of input parameter variations for QCD models: LEPTO 6.5, HERWIG 5.9 and RAPGAP 2.06 compared to the differential π°-meson cross sections as a function of x in three regions of Q^2. . . . 107
B.2 The effect of input parameter variations for QCD models: ARIADNE 4.10 compared to the differential π°-meson cross sections as a function of x in three regions of Q^2. 108

Introduction

For the structure of matter, the current understanding is that all matter is made up of point-like particles (leptons and quarks). Their interactions are mediated by exchange particles (bosons). The theoretical framework of particle physics is provided by the *Standard Model*, which describes all the known fundamental forces except gravity. Gravity appears to be much too weak to be significant for ordinary particle processes. The electromagnetic and the weak force are mediated by the massless photon and the massive $Z^\circ/W^\pm$-bosons respectively. This thesis is mainly concerned with the strong force which is responsible for the interactions of quarks and gluons. Quarks are confined in hadrons and cannot be isolated for investigation. It is therefore necessary to study the structure of hadrons.

In this analysis deep-inelastic positron-proton scattering events are used to investigate the properties of the strong interaction. The experimental environment is provided by the accelerator facility HERA which collides counter-rotating positron and proton beams at a center of mass energy of $\sqrt{s} = 300$ GeV. The reaction products of scattering events are recorded by the H1 detector built around the northern of the four collision regions of HERA.

Two problems immediately appear if one tries to compare the measurements to the predictions made by the theory. Firstly, calculations are made for the interacting quarks and gluons, but only the hadrons in which they are confined can be observed. Secondly, although the basic equations of the theory are available, they can only be solved in various approximations. The region of validity for these approximations is not known a priori. It is hence very interesting to measure observables which a) retain the characteristics of the partonic final state after hadronization, and b) explore regions of the phase space where the approximations become critical.

The large amount of data taken by H1 in recent years provides the possibility to study an observable which fulfills both requirements: The production of high transverse momentum ($\gtrsim 2$ GeV) particles at low values of the kinematical quantity Bjorken-x ($x \gtrsim 5{\cdot}10^{-5}$). Especially interesting is the region close to the proton remnant (called the 'forward' region), since here predictions of different approximations differ strongly. Experimentally π°-mesons turn out to be the most suitable particle for this measurement. The observables measured in this analysis are therefore differential forward high p_T π°-meson production cross sections at low Bjorken-x.

The structure is as follows: In Chapter 1 the theoretical framework is developed to the necessary extent. The theory provides the motivation for this measurement and guides the interpretation of the results. The experimental results themselves, however, are of course independent of this framework. The experimental apparatus is introduced in Chapters 2 and 3. Chapter 4 is devoted to the selection of deep-inelastic scattering events from the available data. The necessary information is mostly obtained from the identification and measurement of the scattered positron. The selection of π°-mesons is described in Chapter 5. Neutral pions decay almost exclusively into two photons. The shape of the resulting electromagnetic shower in the calorimeter is analyzed in detail and used to statistically select π°-mesons over the often dense hadronic background. This strategy takes advantage of the very fine granularity of the H1 main calorimeter. In Chapter 6 the neutral pion production cross sections are determined. The distributions are corrected for detector effects and for the influence of QED radiation. Sources of systematic uncertainties are studied to estimate the resulting uncertainty for the neutral pion cross sections. The results are then given including the statistical and the systematic uncertainties associated with each data point. Finally in Chapter 7 the results are interpreted in terms of the available theoretical models. Last but not least the dependency of the predictions given by the various models on some of their respective input parameters is studied in the appendix.

Chapter 1

The Theory of Deep-Inelastic Scattering

The framework for the present analysis is provided by the theory of deep-inelastic positron-proton scattering (DIS). Both the motivation for the measurement and the interpretation of the results are based on this theory. Extensive reviews of theoretical issues in DIS are available [1, 2]. In this chapter the formalism is developed to the extent necessary to position the measurement within the framework available today.

First a number of kinematical quantities are defined which are commonly used to describe DIS processes. The cross section for deep-inelastic positron-proton scattering is introduced and interpreted in terms of the quark-parton model (QPM). Subsequently necessary modifications when considering the influence of the strong interaction as described by Quantum Chromodynamics (QCD) are discussed. Emphasis is placed on the treatment of parton emissions at small values of the Bjorken scaling variable x. The basic features of several parton emission mechanisms are given. The need for observables sensitive to the dynamical features of the emitted partons directly motivates the measurement of high p_T particle cross sections. The sensitivity of high p_T particles to the underlying parton dynamics is demonstrated.

Based on the mechanisms for emitting partons mentioned above, different models are available to predict the properties of the partonic final state. The main features of these models are discussed in some detail. Finally the partons have to be converted into hadrons to allow direct comparisons to the observed particle production. The main features of two hadronization models are described.

1.1 Kinematical Variables in DIS

The kinematics of deep-inelastic ep scattering can be described by two independent variables (such as the polar angle and the energy of the scattered positron) once

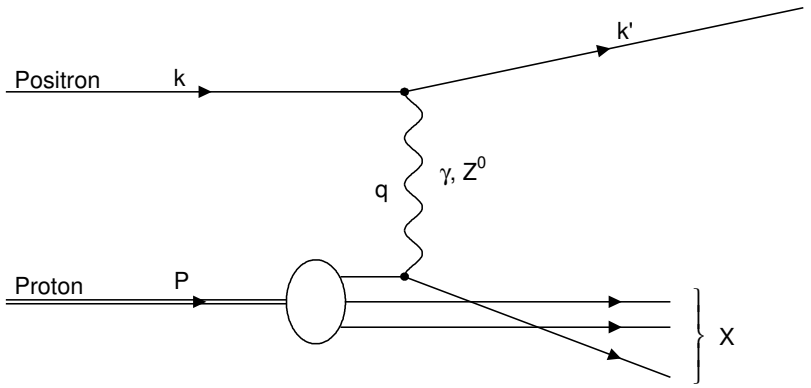

Figure 1.1: Four-vectors used to construct Lorentz-invariant kinematical quantities in deep-inelastic scattering.

the center of mass energy is given by the energies of the incident particles. In many cases it is convenient to use a set of Lorentz invariant quantities.

From the four-vectors of the incoming positron (k) and proton (P) (see Figure 1.1) one first of all obtains the center of mass energy squared

$$s = (P + k)^2 . \tag{1.1}$$

With the four-vector of the outgoing lepton (k') the invariant mass squared of the exchanged virtual boson is

$$Q^2 = -q^2 = -(k - k')^2 . \tag{1.2}$$

The two dimensionless variables x and y are also very commonly used. They are constructed using Q^2, P and k such that their values are confined to the range $0 \leq x, y \leq 1$

$$x = \frac{Q^2}{2 \cdot P \cdot q} \tag{1.3}$$

$$y = \frac{P \cdot q}{P \cdot k}. \tag{1.4}$$

The invariant mass squared of the outgoing hadronic system X in Figure 1.1 is given by

$$W^2 = (q + P)^2 . \tag{1.5}$$

Neglecting the lepton and nucleon masses, the following relations hold between these quantities:

$$Q^2 = s \cdot y \cdot x , \qquad W^2 = Q^2 \frac{1 - x}{x} . \tag{1.6}$$

1.2 The Cross Section for Deep-Inelastic ep Scattering

The basic process of deep-inelastic positron-proton scattering is

$$e + P \rightarrow e' + X\,, \tag{1.7}$$

where e and e' are the incoming and the outgoing lepton respectively, P is the incoming proton and X denotes the hadronic final state resulting from the scattering process. The interaction proceeds via the exchange of a neutral (γ/Z°) or charged ($W^\pm$) boson. In the latter case the final state positron is replaced by a neutrino. This analysis is only concerned with neutral current (NC) processes. The NC cross section can be written as

$$\sigma_{\mathrm{NC}} = \sigma(\gamma) + \sigma(Z^\circ) + \sigma(\gamma Z^\circ). \tag{1.8}$$

The first and second term describe the contribution from γ and from Z° exchange respectively, the last term is the γZ° interference. Contributions from Z° exchange, however, are suppressed due to the large mass of the Z°-boson:

$$\frac{\sigma(\gamma Z^\circ)}{\sigma(\gamma)} = \frac{Q^2}{Q^2 + M_{Z^\circ}^2} \qquad \text{and} \qquad \frac{\sigma(Z^\circ)}{\sigma(\gamma)} = \left(\frac{Q^2}{Q^2 + M_{Z^\circ}^2}\right)^2 . \tag{1.9}$$

The Z° mass squared $M_{Z^\circ}^2$ is about 84000 GeV^2 [3]. In this analysis only scattering events with $Q^2 < 100$ GeV^2 are considered. The contribution from Z° exchange and γZ° interference can therefore be neglected.

The differential cross section for inelastic positron-proton scattering may be then written as [1]:

$$\frac{d^2\sigma_{\mathrm{e^+P}}^{\mathrm{NC}}(x,Q^2)}{dxdQ^2} = \frac{4\pi\alpha^2}{xQ^4}\left[xy^2F_1(x,Q^2) + (1-y)F_2(x,Q^2)\right] , \tag{1.10}$$

where α is the electromagnetic coupling constant. A third structure function F_3 takes the parity violating Z° exchange into account, which can be neglected here for the reasons given in (1.9). The other two structure functions $F_1(x,Q^2)$ and $F_2(x,Q^2)$ are required since the cross section has two independent contributions from the absorption of transversely (σ_{T}) and longitudinally (σ_{L}) polarized virtual photons. $F_1(x,Q^2)$ describes σ_{T} and $F_2(x,Q^2)$ describes the sum $\sigma_{\mathrm{T}} + \sigma_{\mathrm{L}}$. A longitudinal structure function $F_L(x,Q^2)$ and the ratio R

$$F_L := F_2 - 2xF_1 \qquad R := \frac{F_L}{F_2 - F_L} = \frac{F_2 - 2xF_1}{2xF_1} = \frac{\sigma_{\mathrm{L}}}{\sigma_{\mathrm{T}}} \tag{1.11}$$

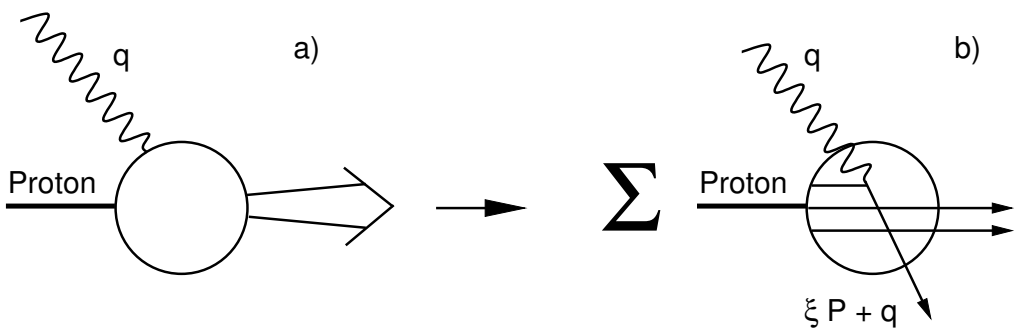

Figure 1.2: The quark-parton model: The interaction at the hadronic vertex is taken to be the sum of incoherent scatterings from the point-like constituents (quarks) of the Proton.

are commonly used, resulting in the following three equivalent expressions for the differential cross section

$$\frac{d^2\sigma^{\mathrm{NC}}_{\mathrm{e^+P}}(x,Q^2)}{dxdQ^2} = \frac{4\pi\alpha^2}{xQ^4}\left[xy^2F_1(x,Q^2) + (1-y)F_2(x,Q^2)\right] \quad (1.12)$$

$$= \frac{4\pi\alpha^2}{xQ^4}\left[\left(1-y+\frac{y^2}{2}\right)F_2(x,Q^2) - \frac{y^2}{2}F_L(x,Q^2)\right] \quad (1.13)$$

$$= \frac{4\pi\alpha^2}{xQ^4}\left[1-y+\frac{y^2}{2}\frac{1}{1+R}\right]F_2(x,Q^2)\,. \quad (1.14)$$

As yet the structure functions thus defined cannot be calculated but have to be determined from experimental data.

1.3 The Quark-Parton Model

The quark-parton model (QPM) was introduced by Feynman [4] in an attempt to interpret the scaling behavior of the structure functions. According to a prediction by Bjorken [5], the structure functions in the limes of $Q^2 \to \infty$ and $P \cdot q \to \infty$ depend only on the dimensionless variable $x = Q^2/(2{\cdot}P{\cdot}q)$:

$$F_1(x,Q^2) \longrightarrow F_1(x) \quad (1.15)$$

$$F_2(x,Q^2) \longrightarrow F_2(x)\,. \quad (1.16)$$

In the first high energy deep-inelastic electron scattering experiments at SLAC [6] F_2 was indeed observed to be independent of Q^2 for the range $1 < Q^2 < 10$ GeV^2. The quark-parton model is based on two assumptions:

- The hadron participating in the scattering process is made of point-like constituents (partons) which travel in the direction of the hadron. The momentum of the hadron is distributed among the partons. The partons were soon taken to be equivalent to the quarks introduced by Gell-Mann [7] to explain the structure of hadrons.

- At large Q^2 the quarks behave as if they were free inside the hadron during the interaction. The photon-hadron interaction can therefore be expressed as the sum of incoherent scatterings from the point-like constituents (see Figure 1.2).

The argument is that the short time-scale of order $1/\sqrt{Q^2}$ causes the photon to see a frozen state of non-interacting quarks and that the final hadronization process occurs long afterwards. If this is the case, the differential cross section for $e + P \to e' + X$ is of the form

$$\frac{d^2\sigma^{\mathrm{NC}}_{\mathrm{e^+P}}(x,Q^2)}{dxdQ^2} = \sum_i \int d\xi f_i(\xi) \frac{d^2\sigma_i(\xi,Q^2)}{d\xi dQ^2}\,, \tag{1.17}$$

where $f_i(\xi)$ is the probability of finding the quark of flavor i in the proton with a fraction ξ of its momentum. The cross section for electron-quark elastic scattering is [1]

$$\frac{d^2\sigma_i(\xi,Q^2)}{d\xi dQ^2} = \frac{4\pi\alpha^2}{Q^4} e_i^2 \frac{1}{2}\left[(1-y) + \frac{y^2}{2}\right]\delta(x-\xi)\,, \tag{1.18}$$

where the δ-function arises from energy-momentum conservation and from neglecting the mass of the outgoing quark, that is $(\xi P + q)^2 = 0$ which then gives $\xi = Q^2/(2{\cdot}P{\cdot}q) = x$. e_i is the electric charge of the respective quark. Inserting (1.18) into (1.17) and integrating out the δ-function yields

$$\frac{d^2\sigma^{\mathrm{NC}}_{\mathrm{e^+P}}(x,Q^2)}{dxdQ^2} = \frac{4\pi\alpha^2}{Q^4}\left[(1-y) + \frac{y^2}{2}\right]\sum_i e_i^2 f_i(x)\,. \tag{1.19}$$

Several important results can now be obtained for the quark-parton model:

- The comparison of (1.19) to (1.12) reveals

$$\frac{F_2}{x} = 2{\cdot}F_1 = \sum_i e_i^2 f_i(x). \tag{1.20}$$

  The QPM thus provides a straightforward relationship between the structure functions and the parton density functions $f_i(x)$.

- The structure functions do not depend on Q^2, but only on x, consistent with the predictions made by Bjorken and the measurements at SLAC.

- $F_2 = 2 \cdot x \cdot F_1$. This is known as the Callan-Gross relationship. It is valid as long as one considers the quarks to be the only constituents of the proton and is a direct consequence of the spin $\frac{1}{2}$ character of the quarks. Looking at (1.11) one gets $R = 0$ and $F_L = 0$, and the longitudinal absorption cross section for virtual photon scattering on quarks vanishes.

If quarks and anti-quarks are indeed the only constituents of the proton, the sum of the momenta they carry should be equal to the momentum of the proton (i.e. the sum of their momentum fractions should be equal to one). Measurements however have demonstrated that

$$\sum_q \int_0^1 x(q(x) + \bar{q}(x))dx \simeq 0.5 \tag{1.21}$$

which indicates that the quarks only carry about half of the momentum of the proton. In Quantum Chromodynamics this deficit in momentum is carried by the gluons.

1.4 Partons in Quantum Chromodynamics

The deviation from unity in (1.21) is a clear indication that quarks cannot be the only constituents of the proton. In addition, measurements covering a larger range of four-momentum transfers Q^2 soon indicated that the scaling behavior of the structure functions is violated. F_2 clearly depends on Q^2 at values of x smaller and larger than accessible in the original SLAC experiments (see Figure 1.3). The quark-parton model therefore cannot be the whole truth.

Quantum Chromodynamics

An explanation of these effects is given by Quantum Chromodynamics (QCD). The essential properties of this theory are [1]:

- Quarks carry the additional degree of freedom *color* as well as electric charge. There are three colors (Red, Green, Blue) which are the charge of the strong interaction.
- Color is exchanged by eight bi-colored gluons. The eight gluons are massless and have spin 1 (bosons). They do not carry electric charge.
- Color interactions are assumed to be a copy of electromagnetic interactions. Quark-gluon interactions can therefore be computed by the rules of QED with the substitution $\sqrt{\alpha} \rightarrow \sqrt{\alpha_s}$ at each vertex and the introduction of color factors. A necessary condition is, of course, that $\sqrt{\alpha_s}$ is small enough to make perturbation theory (as used in QED) applicable.

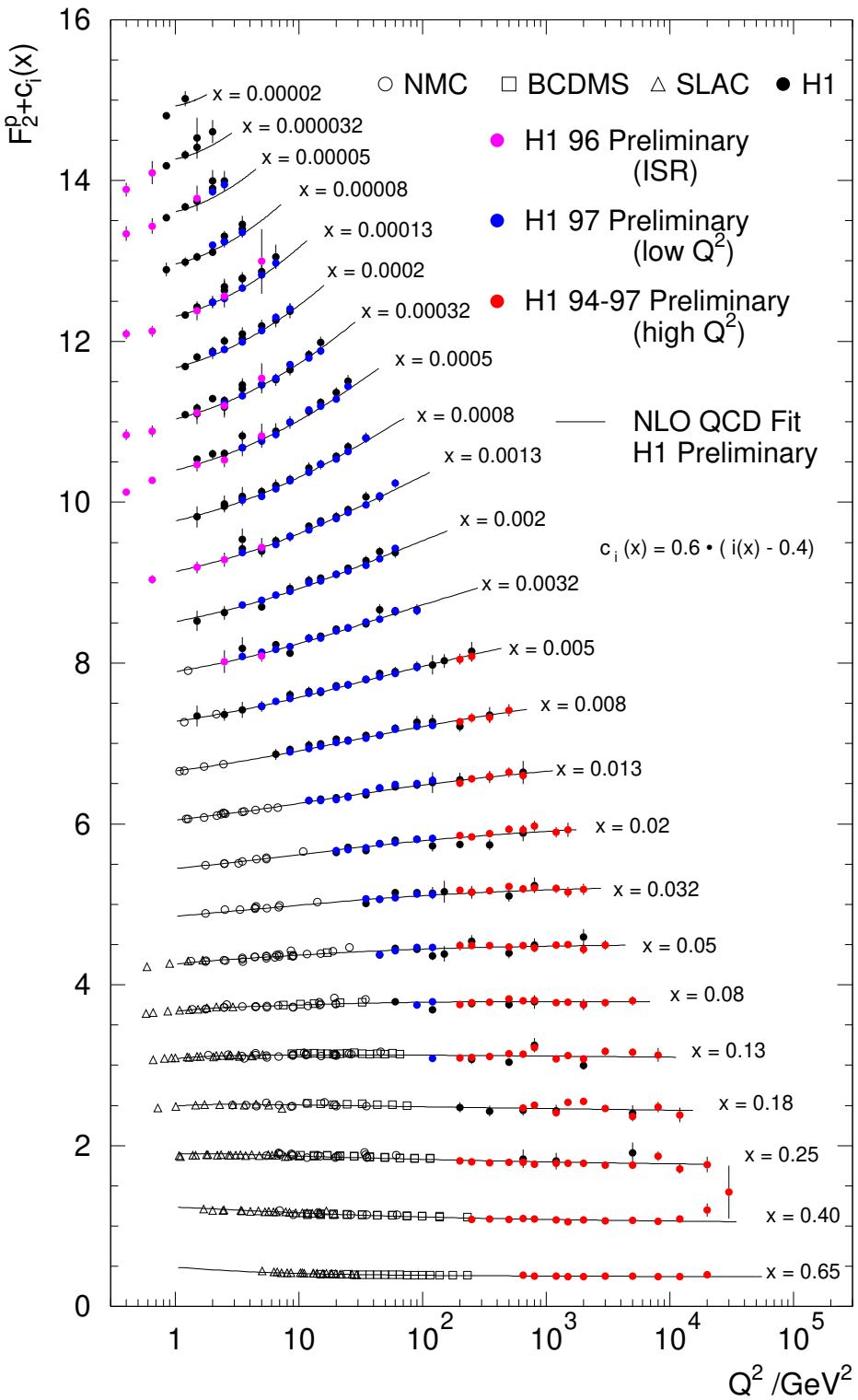

Figure 1.3: The proton structure function $F_2^p(x, Q^2)$ from H1 and from fixed target experiments [8]. The values are shifted for easier presentation by $c_i(x) = 0.6 \cdot i(x) - 0.4$ starting from $i = 1$ for $x = 0.65$.

- Gluons themselves carry color charge and can interact with other gluons.

The self-coupling of gluons manifests the non-Abelian nature of QCD. It leads, in contrast to the Abelian QED, to an *anti*-screening effect as a result of vacuum polarization around a color charge – the closer one probes this charge the less strong it appears.

To calculate cross sections in QCD one needs to integrate over the entire phase space of (real and virtual) quarks and gluons. These integrals, however, turn out to be divergent. A scheme is therefore defined to leave out the divergent parts of the integrals (regularization). The calculated cross sections become dependent on the energy scale μ_r^2 used in the regularization. This unphysical dependence of the cross sections on the scale μ_r^2 is compensated by defining an effective coupling constant and effective parton masses which absorb the divergent contributions (renormalization). The scale μ_r^2 is referred to as renormalization scale. The coupling constant is defined by the renormalization scheme used and depends on the scale μ_r^2. Requiring the cross sections to be independent of μ_r^2 leads to the renormalization group equation (RGE), which describes the dependence $\alpha_s(\mu_r^2)$. The RGE can be written as a perturbative expansion in α_s. The solution for the coupling constant when calculating to $\mathcal{O}(\alpha_s)$ is

$$\alpha_s(\mu_r^2) \;=\; \frac{4\pi}{\beta_0 \ln\left(\mu_r^2/\Lambda^2\right)} \;, \tag{1.22}$$

with $\beta_0 = 11 - 2n_f/3$ and n_f the number of quark flavors. Λ is a free parameter of QCD which has to be determined from experimental results. The value of α_s is usually given at the mass squared of the Z°. The current world average is $\alpha_s(M_Z^2) = 0.119 \pm 0.002$ [3]. The behavior of the coupling constant α_s has two immediate consequences:

- At high energies α_s is small and the quarks are 'asymptotically free'. In this kinematic region perturbation theory may be used to perform calculations within QCD.
- At large distances the coupling constant increases, leading to the confinement of quarks within hadrons. Here non-perturbative methods are needed.

It also means that in order to use perturbation theory at all, it must be possible to separate short-range from long-range processes. This is the idea of factorization, which will be important in the next section.

QCD corrections to the structure of the proton

In QCD the picture of the proton as used in the quark-parton model is modified by allowing gluon radiation. The QPM in this sense can be regarded as the lowest order process of QCD. Introducing the gluons provides ways to overcome the shortcomings of the QPM in describing experimental observations:

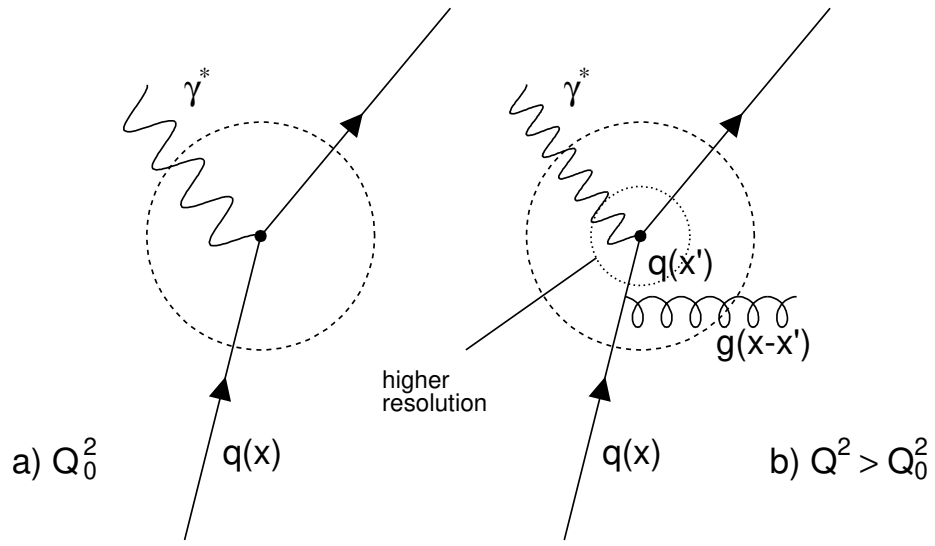

Figure 1.4: Gluon radiation and scaling violations: The higher resolution in (b) causes the virtual photon to 'see' more partons which on average carry a smaller fraction of the proton's momentum.

- The fractional momentum sum no longer deviates from unity. The missing momentum is carried by (electrically) uncharged gluons.
- The violation of Bjorken-scaling at large and small Bjorken-x can be explained by allowing the quarks to radiate gluons which in turn can split into $q\bar{q}$-pairs. The resolution increases with increasing energy (e.g. Q^2 in DIS). More and more gluon radiation processes and $q\bar{q}$-splittings can therefore be resolved, so that the apparent number of partons which share the proton's momentum increases (see Figure 1.4). Hence there is an increased chance of finding a quark at small x and a decreased chance of finding one at high x when moving towards larger Q^2. The result is a scale-violating Q^2 dependence of the structure functions.

Another consequence is, of course, that the simple relationship between the structure functions and the probability distribution of the quarks in momentum space no longer holds in its simple form (1.20). It was, after all, based on the assumption of an incoherent sum of γq scatterings. The separation of long range and short range processes according to the idea of factorization however allows a more general formulation for the structure functions

$$F_2(x,Q^2) = \sum_{i=q,g} \int_x^1 d\xi \; C_i^V \left(\frac{x}{\xi}, \frac{Q^2}{\mu_r^2}, \mu_f^2, \alpha_s \right) \cdot q_{i,h} \left(\xi, \mu_r^2, \mu_f^2, \alpha_s \right) \; , \tag{1.23}$$

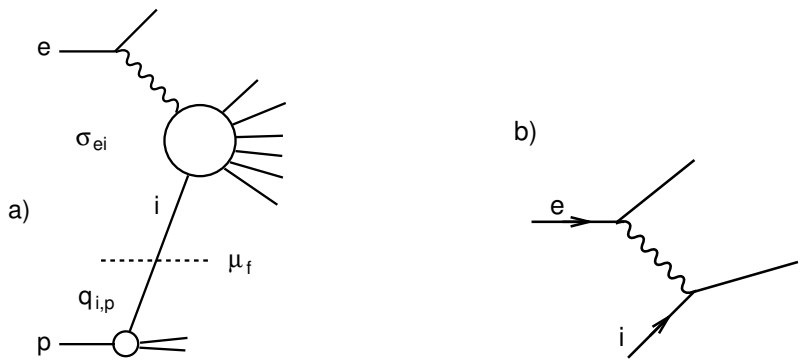

Figure 1.5: (a) The ep cross section is factorized into positron-parton cross sections σ_{ei} and parton densities $q_{i,p}$. (b) shows the lowest order diagram contributing to σ_{ei} in (a).

where the sum extends over all (anti-)quark and gluon densities. C_i^V are the coefficient functions for each type of parton i and exchanged boson V (here the virtual photon). μ_r^2 is the renormalization scale introduced above. The factorization scale μ_f^2 defines the point of separation between long range and short range phenomena (see Figure 1.5). If the relevant scale for a process is larger than μ_f^2, this process is considered calculable in perturbative QCD. In the example above Q^2 is taken to be the relevant scale. Everything below μ_f^2 is absorbed into the parton densities $q_{i,h}$. This definition determines the properties of the coefficient functions C_i^V and the parton densities $q_{i,h}$:

- C_i^V includes the 'hard' subprocess, which can be calculated using perturbation theory. The form of the coefficient functions depends on the parton-flavor i and the exchanged boson V. It does, however, not depend on the type of hadron entering the process. C_i^V in (1.23) can therefore be used to calculate the structure function of any hadron such as the proton, neutron or pions.

- The parton densities $q_{i,h}$ are specific to the hadron h. They are, however, independent of the 'hard' subprocess under consideration. Once they have been extracted from the comparison with experimental data, the parton densities can therefore be used to describe any hard interaction. In this sense they are refered to as *'universal parton densities'*.

One should note that while C_i^V and $q_{i,h}$ depend on the choice of renormalization and factorization scale, $F_2(x, Q^2)$ does not. Any dependence on μ_f^2 and μ_r^2 therefore has to cancel when the sum and the integral are carried out in (1.23). In practice the perturbative series for the coefficients C_i^V has been calculated completely only to next-to-leading order in α_s for the inclusive ep cross section. Some dependence

on μ_f^2 and μ_r^2 hence remains due to higher order effects which then also limit the notion of universality for the parton densities determined from experimental data.

Since these equations can not be solved completely so far, several approximations of QCD are commonly used which are valid in different regions of the phase space. In the perturbative expansion terms of the form $(\alpha_s \ln(Q^2/Q_0^2))$, $(\alpha_s \ln(1/x))$ and mixed terms $(\alpha_s \ln(Q^2/Q_0^2) \ln(1/x))$ appear. In the DGLAP scheme $(\alpha_s \ln(1/x))$ terms are neglected. The BFKL approach on the other hand takes the $(\alpha_s \ln(1/x))$ terms to be dominant over the $(\alpha_s \ln(Q^2/Q_0^2))$ terms used in the DGLAP approximation. As x decreases the mixed terms might be dominant if Q^2 is not too small. The CCFM equation finally promises a smooth transition between the domains of small and large x. These approximations will be treated in more detail in the following sections.

1.5 The DGLAP Evolution Equations

It has not been possible so far to calculate the parton densities $q_{i,h}$ from first principles in QCD. However, towards large Q^2 (the coupling constant α_s decreases) one can employ perturbative calculations to predict the evolution of the parton densities. The evolution of the quark and the gluon densities in this region is given by the DGLAP (Dokshitzer, Gribov, Lipatov, Altarelli, Parisi) equations [9]:

$$\frac{dq_i(x,Q^2)}{d\ln Q^2} = \frac{\alpha_s}{2\pi}\int_x^1 \frac{d\xi}{\xi}\left[q_i(\xi,Q^2)P_{qq}\left(\frac{x}{\xi}\right) + g(\xi,Q^2)P_{qg}\left(\frac{x}{\xi}\right)\right], \quad (1.24)$$

$$\frac{dg(x,Q^2)}{d\ln Q^2} = \frac{\alpha_s}{2\pi}\int_x^1 \frac{d\xi}{\xi}\left[\sum_i q_i(\xi,Q^2)P_{gq}\left(\frac{x}{\xi}\right) + g(\xi,Q^2)P_{gg}\left(\frac{x}{\xi}\right)\right]. \quad (1.25)$$

The index i denotes the quarks and anti-quarks of all flavors. The splitting functions $P_{i,j}(z)$ give the probability for parton branchings $q \to qg$, $g \to gg$ and $g \to q\bar{q}$, where the daughter parton i carries a fraction $(1-z)$ of its mother's (j) momentum (see Figure 1.6). The splitting functions are calculable by perturbative expansion

$$P_{ij}(z,\alpha_s) = \frac{\alpha_s}{2\pi}P_{ij}^0 + \left(\frac{\alpha_s}{2\pi}\right)^2 P_{ij}^1 + \cdots \quad (1.26)$$

In leading order the splitting functions are:

$$\begin{aligned} P_{qq}^0(z) &= P_{gq}^0(1-z) = \frac{4}{3}\left[\frac{1+z^2}{(1-z)_+}\right] + 2\cdot\delta(1-z) \\ P_{qg}^0(z) &= \frac{1}{2}(z^2+(1-z)^2) \\ P_{gg}^0(z) &= 6\left[\frac{z}{(1-z)_+} + \frac{1-z}{z} + z(1-z)\right] + (11-\frac{n_f}{3})\cdot\delta(1-z)\,. \end{aligned} \quad (1.27)$$

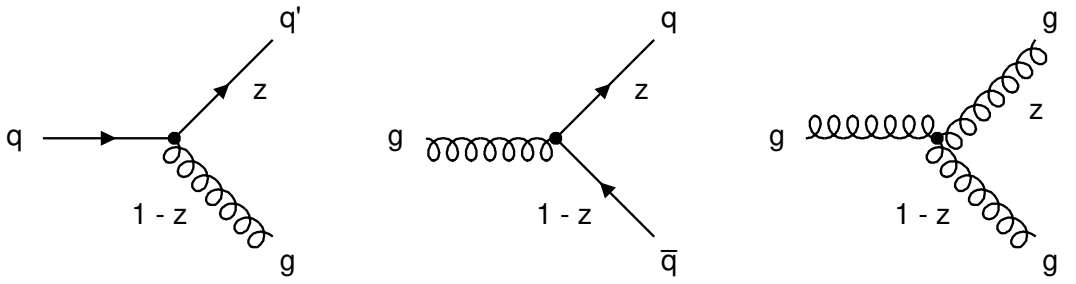

Figure 1.6: Feynman graphs for splitting functions. The following processes are shown (from left to right): $q \to q'g$ (P_{qq}, P_{gq}), $g \to q\bar{q}$ (P_{qg}) and $g \to gg$ (P_{gg}).

The subscript '+' indicates that the singularities at $z = 1$ (corresponding to the collinear emission of partons) are regularized by using the prescription

$$\int_0^1 dz \frac{f(z)}{(1-z)_+} := \int_0^1 dz \frac{f(z) - f(1)}{1-z} \tag{1.28}$$

for any function $f(z)$. The DGLAP equations can be obtained using the Leading-Log Approximation (LLA). In leading order α_s the dominant contributions are here given by $(\alpha_s \ln(Q^2/Q_0^2))^n$ terms which can be summed for all orders n. The leading role of the Q^2 terms is inherent in the perturbative ansatz. Dokshitzer [9] showed that in an axial gauge (where the gluon only has the two physical polarization states) the LL(Q^2) is equivalent to the sum of ladder graphs as shown in Figure 1.7. The LL(Q^2) contribution comes from the region of phase space given by the following two conditions:

- The transverse momenta $k_{T,i}^2$ of the emitted partons are strongly ordered such that $k_{T,i}^2 \ll k_{T,i+1}^2 \ll \cdots \ll Q^2$.
- The longitudinal momenta x_i of the emitted partons satisfy the constraint $x_i > x_{i+1} > \cdots > x$.

The region where the LLA is applicable at all is given by the use of perturbation theory and by neglecting $\ln(1/x)$ terms in the LLA sum:

$$\begin{aligned} \alpha_s(Q^2) \ln(Q^2/Q_0^2) &\sim 1 \\ \alpha_s(Q^2) \ln(1/x) &\ll 1 \\ \alpha_s(Q^2) &\ll 1 \end{aligned} \tag{1.29}$$

Hence, if the terms including $\ln(1/x)$ become larger, the DGLAP equations as described above are no longer applicable. At HERA values of $x < 10^{-4}$ have been reached, where the influence of these logarithms might well be visible. It should be noted that in the DGLAP scheme no statement is made about the x dependence

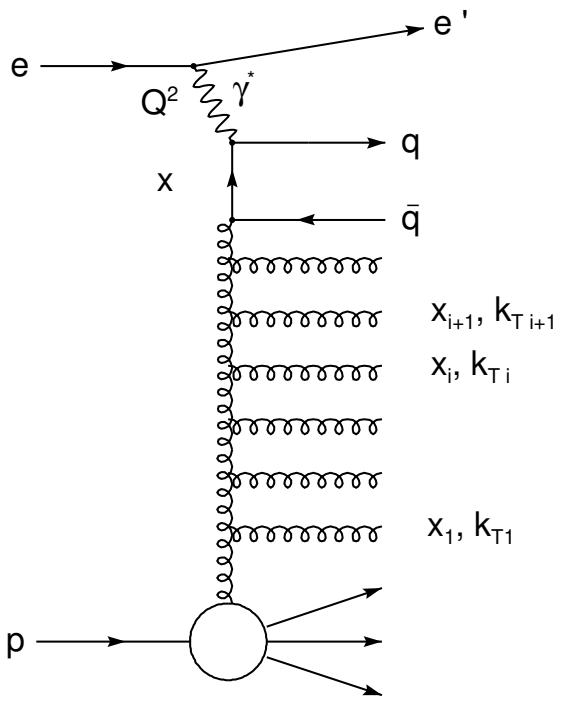

Figure 1.7: Ladder diagram to visualize the parton evolutions in QCD. The gluon longitudinal and transverse momenta are labeled x_i and $k_{T,i}$.

of the parton distributions. One can therefore use input parton distributions which rise at small x to describe the data measured at HERA to the lowest available values of $Q^2 \simeq 0.5$ GeV^2 [10]. When moving towards smaller x, contributions $\alpha_s \ln(1/x)$ and $\alpha_s \ln(1/x) \ln(Q^2/Q_0^2)$ become important. If the latter are dominant the double-leading-log approximation (DLLA) can be used, which in addition to the strong ordering in $k_{T,i}^2$ of the emitted partons also requires the longitudinal momenta to be strongly ordered: $x_i \gg x_{i+1} \gg \cdots \gg x$.

1.6 The BFKL Equation

When x becomes small but Q^2 is not large enough for the DLL scheme to be applicable, the DGLAP approximations cease to be valid. In this region one needs to sum diagrams which are leading in $\ln(1/x)$ independent of $\ln Q^2$. This is carried out by the BFKL (Balitsky, Fadin, Kuraev, Lipatov) equation [11]. Here the gluon ladder need not be ordered in k_T. The gluon distribution therefore is not integrated over k_T. This unintegrated gluon density $f(x, k_T^2)$ relates to the more familiar gluon

density as follows

$$xg(x,Q^2) = \int_0^{Q^2} \frac{dk_T^2}{k_T^2} f(x,k_T^2). \tag{1.30}$$

The BFKL equation can then be written as

$$\frac{df(x,k_T^2)}{d\ln(1/x)} = \int dk_T'^2 \, K(k_T^2,k_T'^2) \, f(x,k_T'^2) = K \otimes f = \lambda f \, , \tag{1.31}$$

which describes the evolution in $\ln(1/x)$ of the unintegrated gluon density. The solution of this equation is controlled by the largest eigenvalue λ of the kernel K [12]. In leading order in $\ln(1/x)$ and for fixed α_s one obtains a very steep power law

$$xg(x,Q^2) \sim f(Q^2)x^{-\lambda} \, , \quad \text{with} \quad \lambda = \alpha_s \frac{12 \cdot \ln 2}{\pi} \simeq 0.5 \, . \tag{1.32}$$

Recent developments however indicate that the inclusion of the running coupling and the next-to-leading order contributions have a large effect on λ [13]. The different scope of the BFKL evolution leads to an ordering scheme for the parton emissions in LL$(1/x)$ which is very different from the DGLAP-type ordering:

- The transverse momenta $k_{T,i}^2$ of the emitted partons are unordered. The parton emissions perform a *random walk* in k_T^2 space.
- The longitudinal momenta x_i of the emitted partons are strongly ordered: $x_i \gg x_{i+1} \gg \cdots > x$.

The fact that the BFKL evolution is not ordered in transverse momentum leads to a diffusion of k_T^2, which can extend into the infra-red region. This is usually avoided by introducing a cut-off parameter k_0^2, below which gluon emissions are not allowed. An unwanted side effect of this procedure is, however, that the results thus obtained show a dependence on this parameter k_0^2.

1.7 The CCFM Equation and the Linked Dipole Chain Model

As stated above, the BFKL and DGLAP equations are valid in quite separate regions of phase space, depending on which set of logarithms is dominant. Catani, Ciafaloni, Fiorani and Marchesini (CCFM) [14] have developed a theoretical framework which treats both the small and the large x region in a unified way. The CCFM equation is based on the coherent radiation of gluons, which leads to an angular ordering of the gluons along a chain of multiple emissions. The CCFM equation is defined in

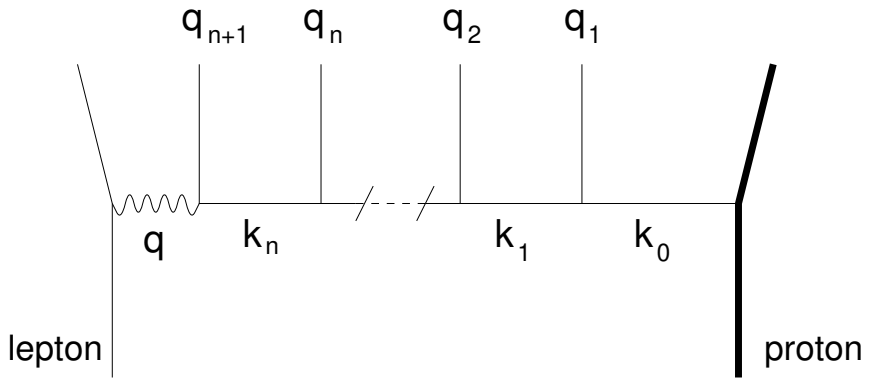

Figure 1.8: The LDC model: fan diagram for a DIS event with n initial emissions. q_i denote the emitted ISB partons, k_i denote the propagators.

terms of a scale dependent unintegrated gluon density $F(x, k_T^2, Q^2)$ quite analog to the BFKL equation above. The integrated gluon density can be recovered by

$$xg(x, Q^2) = \int^{Q^2} \frac{dk_T^2}{k_T^2} f(x, k_T^2, Q^2) \,. \tag{1.33}$$

The angular ordering introduces the additional scale which is needed to specify the maximum angle for a gluon emission. At very small x the angular ordering does not constrain the transverse momenta along the chain and F becomes the Q^2-independent gluon of the BFKL equation. Moving towards larger x the angular ordering becomes equivalent to an ordering in the gluon transverse momenta and one recovers the behavior of the DGLAP evolution [15].

Recently the CCFM approach has been reformulated to obtain the Linked Dipole Chain Model (LDC). The possible parton emissions are separated into Initial State (ISB) and Final State Bremsstrahlung (FSB). The ISB set in the CCFM model is defined by requiring that the emissions are ordered in rapidity and energy. In the LDC model an additional constraint on the transverse momenta in each emission is introduced [16] (see Figure 1.8 for the definition of the variables)

$$q_{T,i} > \min[(k_{T,i}), (k_{T,i-1})] \,. \tag{1.34}$$

Emissions which violate this condition are moved into the FSB set. The FSB kinematical region in the LDC thus formulated is consistent with the Color Dipole Model [17] for parton cascades. The initial ISB partons are assumed to form a chain of linked color dipoles which can radiate partons independently.

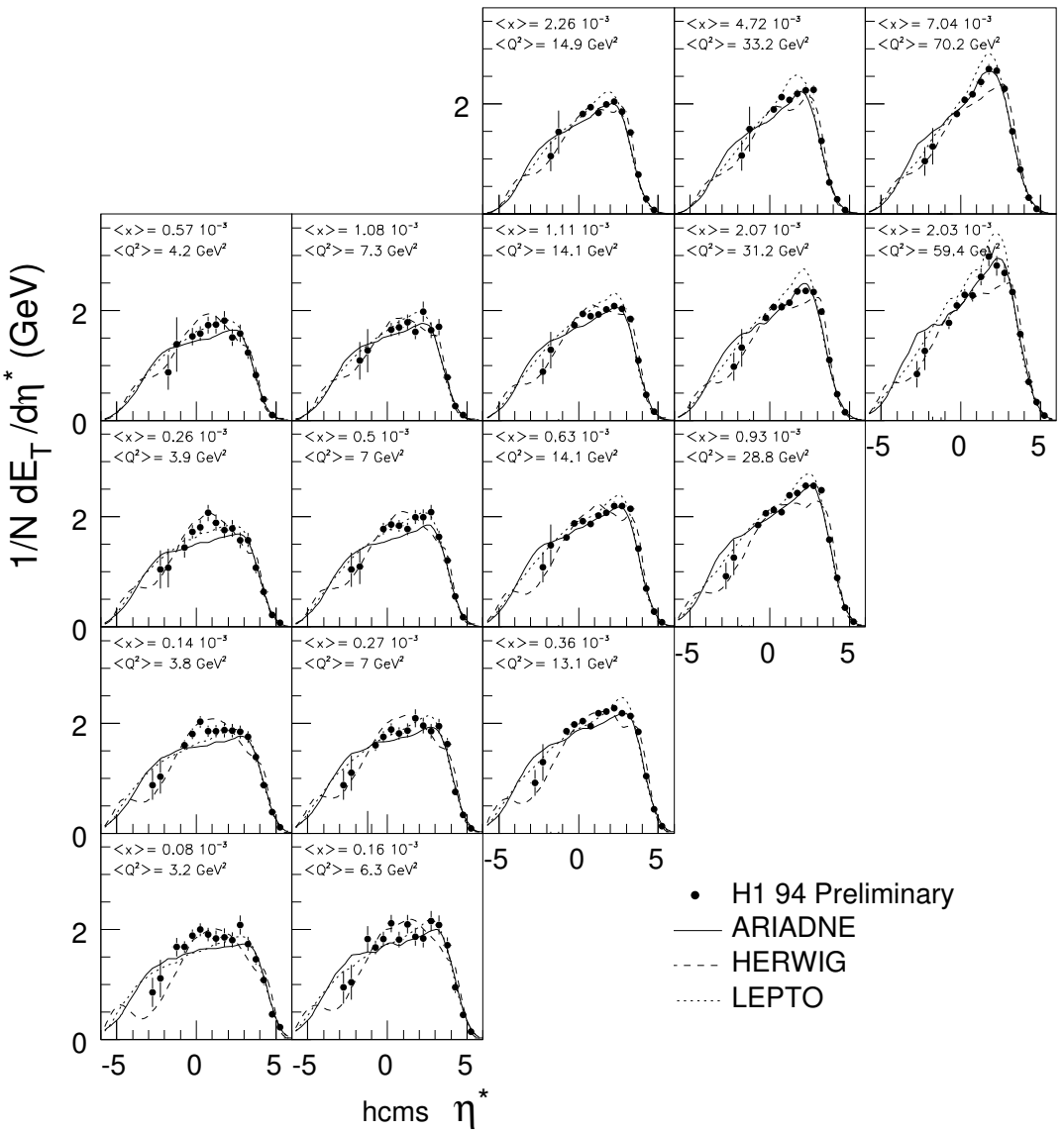

Figure 1.9: The transverse energy flow as a function of pseudorapidity in the hadronic cms [18]. The proton direction is to the left. The errors represent the statistical error only. Three QCD models are overlaid for comparison.

1.8 The Merits of High p_T Particle Observables

If there is one thing to be learned from the previous sections, it is that observables are needed to provide cornerstones on the road to further theoretical development. The most insight into the mechanisms at work will be provided by the approach which predicts the widest range of observations with the least number of starting assumptions. One of the most important measurements driving the understanding

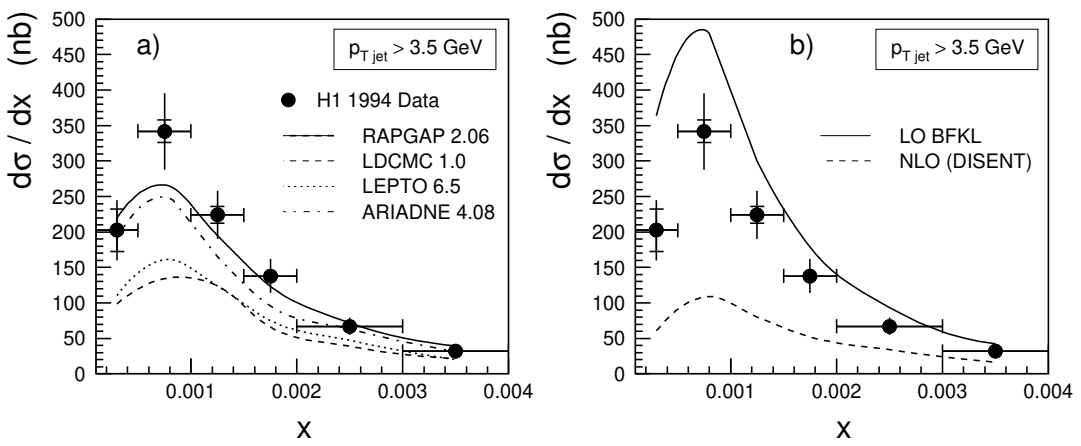

Figure 1.10: The forward jet cross sections as a function of Bjorken-x as measured by H1 [19]. The jets fulfill the condition $0.5 < p_{T,j}^2/Q^2 < 2.0$. The errors shown are the statistical (inner) and the systematic error added in quadrature. The overlaid lines represent QCD model predictions (see [19] for a discussion of the models).

of the structure of hadrons and of processes involving multi-parton radiation has been the determination of the hadron structure functions such as $F_2^P(x, Q^2)$. Data is available down to $x \sim 10^{-5}$ and up to $Q^2 \sim 10^4$ GeV^2. The following situation has now emerged:

- QCD analyses based on the DGLAP evolution (see Section 1.5) in next-to-leading order α_s give a good description of the data down to very low values of Q^2 and x (see Figure 1.3), where in fact $\ln(1/x)$ contributions should become important.
- The problem in identifying the underlying small x dynamics is not due to the insufficient kinematical reach of the experiments, but rather due to the parametric freedom in specifying the initial conditions of the theory [10].
- The measurement of F_2 is too inclusive. One should explore properties of the hadronic final state in deep-inelastic scattering.

When trying to identify the dynamics leading to the *partonic* final state by measuring observables of the *hadronic* final state, another problem presents itself: hadronization. The process of converting the partonic properties of an event (as predicted by a theoretical model) into observable hadrons may wash out differences between the various models. A striking example of such an effect is the measurement of the transverse energy flow by H1. Although different models predict very different E_T-flows for the partonic final state [20], they are compatible with the data and with each other for the hadronic final state (see Figure 1.9). One therefore needs observables which retain the characteristics of the underlying parton level even after

hadronization. The classical way of measuring the properties of an outgoing hard parton is based on the idea that whatever the final observable particles are, they will be close to the original parton in the appropriate space (e.g. transverse momentum relative to the original direction). Various algorithms are then used to collect all these particles into a 'jet'. An elegant way to probe the small x behavior of QCD was proposed by Mueller [21]. He suggested the study of deep-inelastic events (x, Q^2) which contain an identified energetic jet (x_j, k_{Tj}^2) close to the proton remnant:

- The jet should satisfy $k_{Tj}^2 \simeq Q^2$, which leaves only little phase space for the DGLAP evolution (see Section 1.5).
- At the same time k_{Tj}^2 has to be sufficiently large to avoid diffusion into the infra-red region as described in Section 1.6.
- The parton densities for this process are to be evaluated at (x_j, k_{Tj}^2), where they are well known from the global analyses, thereby reducing the ambiguities from the choice of the non-perturbative parton input.

This kind of measurement has been carried out by ZEUS [22] and H1 [19]. Part of the H1 results are shown in Figure 1.10. A detailed discussion of the results can be found in [19]. The differences between the various QCD models are clearly visible for this observable (defined for the hadronic final state).

From the above one can conclude that the interesting phase space is to be found close to the proton remnant and at high transverse momenta. It is mostly experimental arguments which lead the way from here to the measurement of high p_T π°-mesons. The first requirement, however, is that the π°-mesons are strongly correlated to the underlying parton dynamics. This is demonstrated in Figure 1.11. The Monte Carlo event generator LEPTO [23] is used to generate DIS events. These events are subjected to hadronization as implemented in the package JETSET [24] to convert the partons into observable hadrons. Events with a π°-meson of $p_{T,\pi} > 2$ GeV are selected if the meson has a polar angle of $5^\circ < \theta_\pi < 25^\circ$ with respect to the incident proton direction. A parton is not necessarily a well defined object in an event generator. The π°-mesons are therefore compared to jets of partons found in the same event. A k_T-type jet-algorithm [25] was used to define the jets. In nearly all ($> 99\,\%$) selected π° events a jet was found. Figure 1.11 (a) shows the correlation in pseudorapidity ($\eta = -\ln(\tan(\theta/2))$) between the π°-meson and the parton jet. The correlation is indeed very strong, indicating that the direction of the initial hard parton(-jet) is in most cases not altered significantly by hadronization effects. Figure 1.11 (b) demonstrates how much of the transverse momentum of the parton jet is carried by the π°-meson. Since the mean value is about 0.4, the initial parton jet on average carries 2.5 times the transverse momentum of the π°-meson measured.

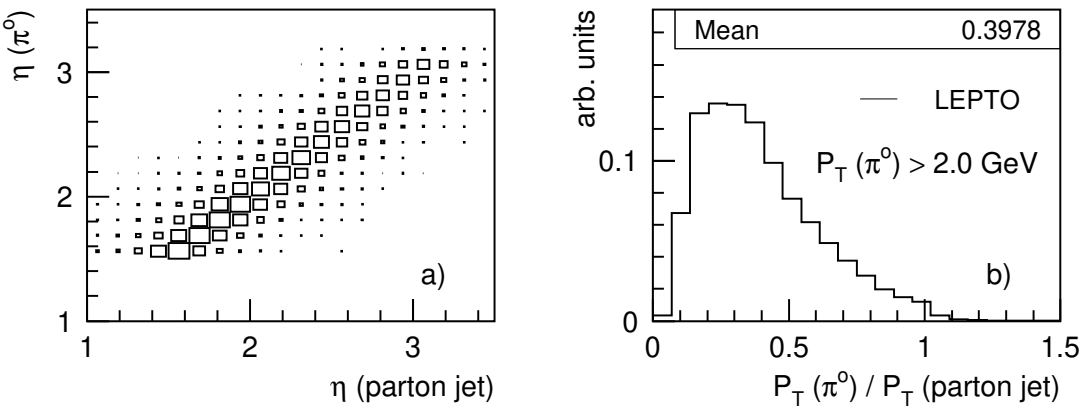

Figure 1.11: The angular correlation (a) and p_T-ratio (b) between π°-mesons and parton-jets in simulated deep-inelastic scattering events. Events are selected to contain a π°-meson with $p_{T,\pi} > 2$ GeV and a polar angle of $5^\circ < \theta_\pi < 25^\circ$ with respect to the incident proton direction. Parton jets are defined using a k_T-type jet algorithm [25].

It now remains to be argued why the π°-mesons are the most suitable particles to be used in such a measurement and what their advantages over the commonly used jet observables are:

- Due to their integrating nature, jet algorithms will pick up an increasing amount of unwanted energy from the proton remnant when moving towards smaller polar angles. The π°-meson as a single particle does not have this problem.
- A jet is defined by the jet algorithm. The properties of the jet algorithm will therefore influence the result. The notion of a particle is much more independent.

Experimentally the π°-meson is the most suitable particle to be measured at high transverse momenta because:

- π-mesons are the lightest hadrons and therefore the most numerous in the hadronic final state.
- The measurement of charged particles in tracking chambers at high momenta is difficult since the tracks are essentially straight.
- The π°-mesons decay into two photons, which cause a purely electromagnetic shower in the calorimeter. Electromagnetic showers are much more compact than showers of hadronic origin. It will be shown in the course of this analysis

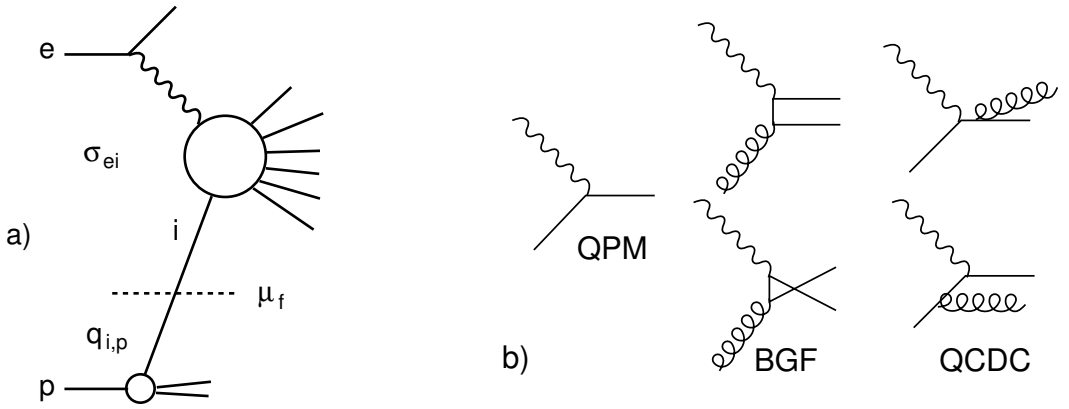

Figure 1.12: Tree level diagrams for γP scattering (b) contributing to σ_{ei} in (a).

that a π°-signal can be selected based on the different nature of electromagnetic and hadronic showers in the calorimeter.

This method can be used up to very high π° energies and down to small angles with respect to the proton remnant – this is the phase space of interest defined above!

To summarize the discussion above: The measurement of π°-meson production provides observables which are strongly correlated to the underlying parton dynamics. Experimentally they allow the exploration of the interesting phase space region close to the proton remnant where differences in the partonic activity of various models are expected to be pronounced. The measurement is not limited as far as high transverse momenta of the π°-meson are concerned. The available reach in $p_{T,\pi}$ is given by the available amount of data only.

1.9 QCD Models

Predictions made by QCD inspired models involve two different aspects: the short range processes which can be calculated perturbatively, and the long range non-perturbative effects of hadronization. The perturbative part of QCD is treated either with fixed order (α_s) calculations of the matrix elements, or with parton showers, or a combination of both. Perturbative QCD makes predictions for the *partonic* final state. Hadronization is the link to the observable world. The string fragmentation model and the cluster fragmentation model are used by the QCD models which will later be compared to the experimental results. A short description of both fragmentation models is given.

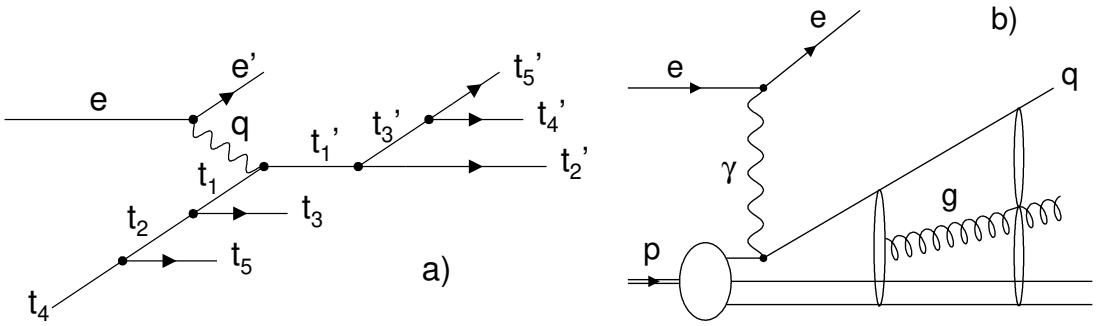

Figure 1.13: Parton cascades in deep-inelastic scattering: (a) Leading Log parton shower: initial and final state parton showers are initiated by successive parton branching. (b) The color dipole model: Partons are radiated from color dipoles stretched between outgoing quark and remnant, and between the resulting partons.

Matrix Elements

In fixed order $(\alpha_s)^n$ perturbation theory, all graphs to order n (including the virtual corrections from loop diagrams) are calculated and summed to obtain a prediction for the process under investigation. In Figure 1.12 (b) tree-level diagrams for γP scattering are shown. The calculations are usually done numerically employing Monte Carlo techniques. Up to now order $n = 2$ calculations are available which, for instance, predict dijet production to NLO(α_s).

Leading Log parton cascade

Complete fixed order $(\alpha_s)^n$ calculations are not available for $n > 2$. Higher order effects can be approximated using the parton cascade ansatz [26]. It has the advantage that arbitrarily high orders in α_s can be simulated, but only in the Leading Log approximation. The quark struck by the electroweak boson in deep-inelastic scattering may emit partons both before and after the boson vertex, corresponding to initial and final state parton showers respectively (see Figure 1.13 (a)). A parton (close to mass shell) in the incoming nucleon can initiate an initial state parton cascade. In each branching one parton becomes increasingly space-like ($m^2 < 0$) and the other is on-shell or has a time-like virtuality ($m^2 > 0$). The result of this initial state (space-like) cascade is a space-like quark which interacts with the electroweak boson. The outgoing quark is either time-like or on-shell. If the outgoing quark is time-like, the result is a final state (time-like) cascade. The off-shell mass is reduced by branching into daughter partons until all partons are essentially on-shell. Any time-like parton from the initial state cascade will undergo a similar development. Both the initial and the final state cascade are based on the branching processes

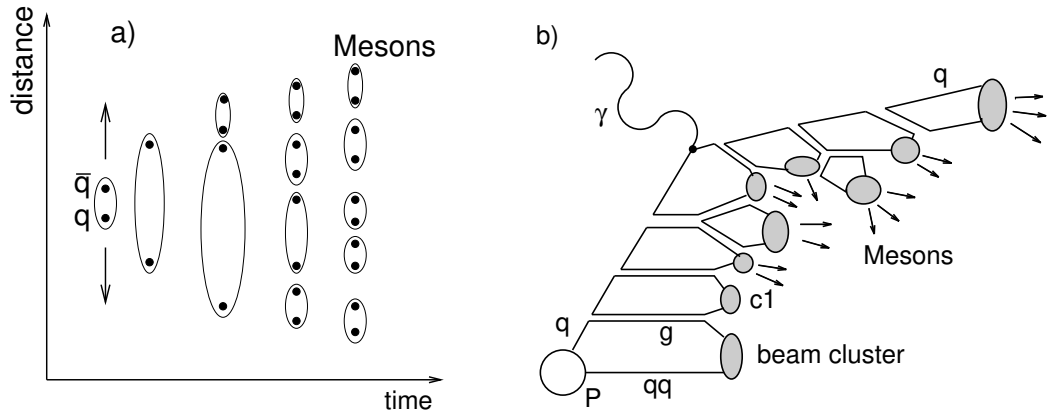

Figure 1.14: (a) The string fragmentation model: New $q\bar{q}$-pairs are created when the string between the two separating partons of a $q\bar{q}$-pair breaks up. Mesons are formed when the string energy is too small to create further $q\bar{q}$-pairs. (b) The cluster fragmentation model: gluons (double lines) are split non-perturbatively into $q\bar{q}$-pairs. Color neutral clusters are formed which decay into mesons.

$q \to qg$, $g \to gg$ and $g \to q\bar{q}$ as described by the DGLAP splitting functions in the LL(Q^2) approximation of QCD (see Section 1.5).

Color Dipole parton cascade

An alternative description of parton showers is provided by the Color Dipole Model (CDM) [17]. Unlike the leading-log parton model the CDM does not divide the QCD cascade into an initial and a final state. Instead all parton radiation is described starting from a color dipole formed between the struck quark and the hadron remnant. Subsequent gluon radiation emanates from color dipoles spanned between the newly created color charges and the original color charges. The process is iterated until all the available energy has been used up. In DIS one of the color charges, the proton remnant, is not point-like. The emission of small wavelengths from an extended antenna is suppressed. The CDM takes this effect into account by introducing an appropriate suppression factor. The boson-gluon fusion (BGF, see Figure 1.12) process is not described by this approach, but has to be inserted by hand. The k_T phase space for gluon emission is bounded by the k_T of the previous emission. The emissions are uniform in rapidity. If one arranges the gluon emissions according to increasing rapidity, the final gluon configuration will therefore be unordered in k_T.

String fragmentation

The string model for fragmentation [24] starts by stretching a color field between the two separating partons of a $q\bar{q}$-pair. The color field is thought to be string-like with a constant energy density per unit length. In DIS strings will also be stretched between the (anti-)quark and the proton remnant. When the energy stored in the string is large enough, the string breaks up by creating a new $q\bar{q}$-pair, forming new string pieces. The process is iterated until all the available energy has been used up. The resulting string fragments are combined into mesons and baryons (see Figure 1.14 (a)). Gluons are realized as kinks in the string, which receive the four-momentum of the gluon.

Cluster fragmentation [27]

In the cluster fragmentation approach color singlets are formed from the partons present after the perturbative evolution. First all gluons are forced to split into $q\bar{q}$-pairs. Neighboring (color connected) $q\bar{q}$-pairs are then combined into low mass color neutral clusters. These clusters are then taken to be superpositions of meson resonances, and they decay into mesons (and baryons) depending on the available phase space (see Figure 1.14 (b)).

Chapter 2

The ep Collider HERA

The **H***adron*-**E***lectron*-**R***ing*-**A***ccelerator* is the first ever storage ring facility to provide colliding beams of electrons and protons. The two main accelerators reside in a tunnel of 6.3 km circumference. They produce counter-rotating beams of 27.5 GeV (electrons) and 820 GeV (protons) resulting in a center of mass energy of 300.3 GeV. The electron ring uses conventional magnet technology, whereas superconducting magnets are needed for the bending fields in the proton ring. Four interaction regions are available to the experimentalists. H1 (north hall) and Zeus (south hall) study electron-positron scattering events. Both experiments have been taking data from ep collisions since 1992. HERA-B (west hall) only utilizes the proton beam in fixed target mode by inserting tungsten wire targets into the beam halo. The HERA-B detector components are expected to be fully operational in 1999. The main focus will be the search for decay modes in the $B^\circ/\bar{B}^\circ$ system indicating a violation of the combined symmetry of charge conjugation and parity (CP). Collisions of the electron beam in polarized mode with a polarized gas target (H_2, D, ^3He,^4He) have been used by the HERMES (east hall) collaboration since 1995 to study phenomena related to the spin of the colliding particles.

A schematic layout of the accelerator complex is shown in Figure 2.1. A chain of accelerators originally built for previous experiments now serves to produce the electron and proton beams at the energy required to inject them into the two main accelerators. Protons are produced by sending negatively charged hydrogen ions through a stripper foil. These protons are then collected into bunches and accelerated to 7.5 GeV in DESY III before they are transfered to PETRA. After the maximum of 70 bunches in PETRA has been reached, the protons are accelerated to 40 GeV and injected into HERA. With a capacity of 210 bunches in HERA 3 iterations of this process are necessary for a complete proton fill.

Electrons are provided by a 500 MeV linear accelerator. The electrons are first accumulated into a single bunch before they are accelerated to 7 GeV in DESY II and transfered to PETRA. Again 70 bunches are collected here before they are

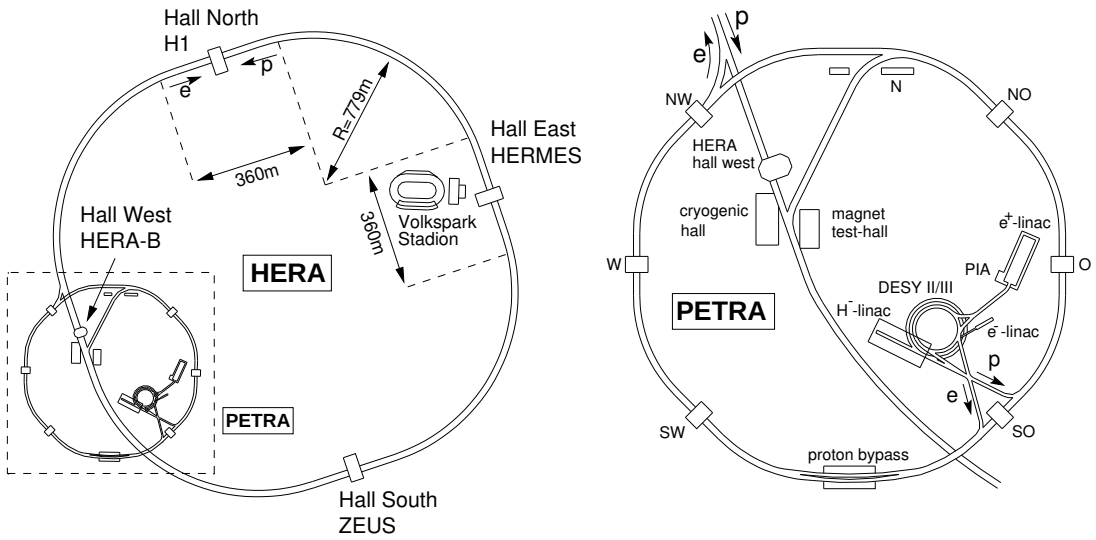

Figure 2.1: Schematic overview of the HERA accelerator complex.

accelerated to 11 GeV and injected into the HERA electron ring. Also here three iterations are needed for a complete fill. Normally the proton beam is produced first and accelerated to its final energy of 820 GeV. Afterwards the electron beam is inserted and brought to 27.5 GeV before both beams are optimized for luminosity production.

During 1994 the electrons were replaced by a positron beam. Positively charged ion-clusters produced by getter pumps which maintain the high vacuum in the electron ring had been found to reduce the lifetime of the beam. These ions are repelled by the positron beam, which therefore has a longer lifetime.

Chapter 3

The H1 Detector

Many aspects of the physics to be studied and the variety of the signatures they produce were not known at the design stage of the detector. To exploit the potential provided by the high energy ep collisions as much as possible, the H1 apparatus was not constructed for a number of specialized measurements but rather as a general purpose detector for ep collisions. This concept is based on a full coverage of the solid angle around the interaction point with the exception of the beam holes where the colliding beams enter the apparatus. Figure 3.1 shows an isometric view of the H1 detector. The asymmetric design of the detector is motivated by the asymmetric beam energies. The center of mass frame of the colliding particles is boosted with respect to the laboratory frame in the direction of the much more energetic proton beam ($\gamma_{\rm cm} = 2.86$). The highest particle and energy densities are expected in this region and the detector is considerably more massive and highly segmented here.

The laboratory frame is described by a right-handed coordinate system such that the proton beam moves along the $+z$ direction. The origin is defined to be the nominal interaction point. The x-axis and y-axis point to the center of the ring and upwards respectively. For many physics parameters, a spherical coordinate system is more appropriate. The azimuthal angle (ϕ) is defined such that $\phi = 0$ points along the x-direction. The polar angle (θ) is measured relative to the z-axis ($\theta = 0$ corresponds to the $+z$-direction). For ultra-relativistic particles the pseudorapidity η is commonly used in place of θ:

$$\eta = -\ln\left[\tan\frac{\theta}{2}\right] = \tanh^{-1}(\cos\theta)\,. \tag{3.1}$$

For massless particles η is the same as the rapidity y, defined by

$$y = \frac{1}{2}\ln\left[\frac{E + p_Z}{E - p_Z}\right]\,. \tag{3.2}$$

The dimensions of the H1 detector are approximately 12 m $\times$ 10 m $\times$ 15 m, with a total weight of about 2800 tons. No single device can perform all particle

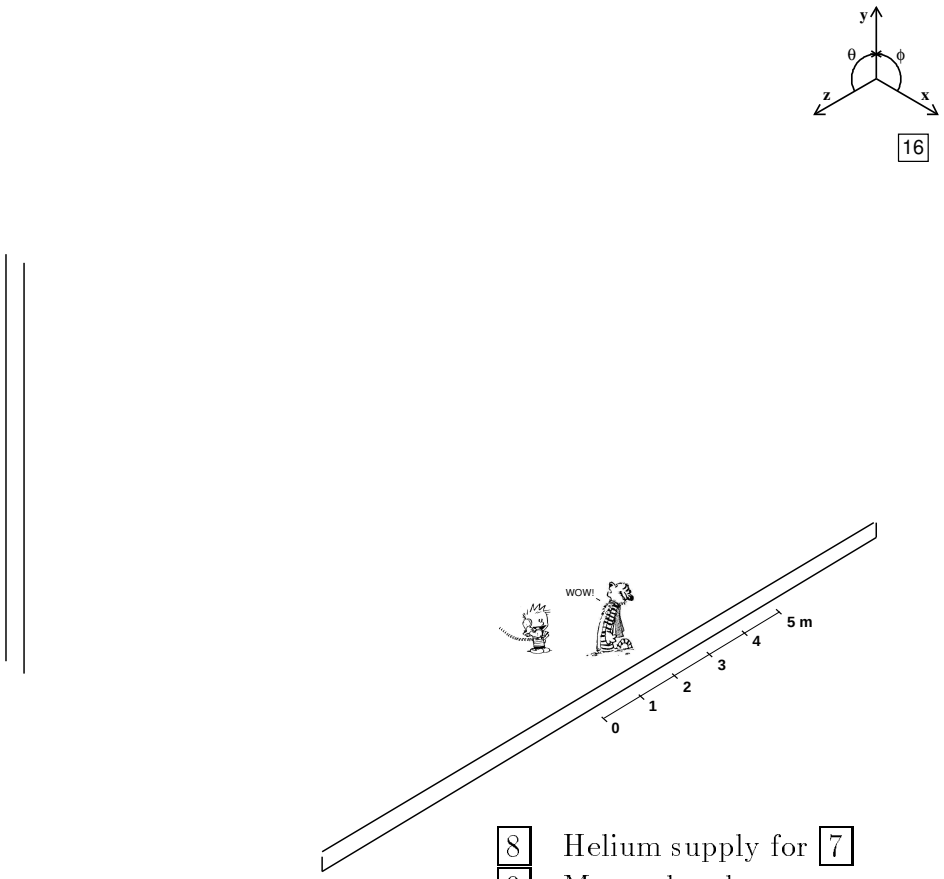

1	Beam pipe and beam magnets	8	Helium supply for 7
2	Central track detectors	9	Muon chambers
3	Forward track detectors	10	Instrumented iron yoke
4	Electromagnetic LAr calorimeter	11	Forward muon toroid
5	Hadronic LAr calorimeter	12	SPACAL and Backward DC
6	Superconducting coil (1.15 T)	13	PLUG calorimeter
7	Compensating magnet	14	Concrete shielding
		15	Liquid argon cryostat
		16	H1 coordinate system

Figure 3.1: An isometric view of the H1 collider detector at HERA.

measurements to the desired precision. The detector is therefore really a group of devices providing complementary information on the reaction products. In the following sections, components of the detector relevant to this analysis are described in more detail.

3.1 Tracking

The H1 tracking system covers the polar angular range from $5° < \theta < 178°$ with full azimuthal coverage. The tracking devices are subdivided into three major components. The Central Tracker covers the region of $15° < \theta < 165°$ and, in addition to drift chambers used for the precise measurement of tracks, also features multi-wire proportional chambers. The spatial resolution of the latter is worse than that of the drift chambers, but their fast response time make them useful for triggering purposes. The Forward Tracker comprises a similar combination of detectors and extends over the range $5° < \theta < 25°$. The Backward Drift Chamber was installed in 1995 as part of a major upgrade of the backward region of the detector. The main goal of this upgrade was a significant improvement in detecting and measuring the scattered positron if it enters the detector at polar angles $155° < \theta < 178°$. Figure 3.2 shows a side view of all tracking devices except the muon detectors. All three major components contribute to the present analysis and will therefore be described in more detail in the following sections.

In 1995 and 1996 Central and Backward Silicon Trackers were installed to provide tracking information very close to the interaction region and for large polar angles respectively. Since no data from these devices are used here they will not be discussed further.

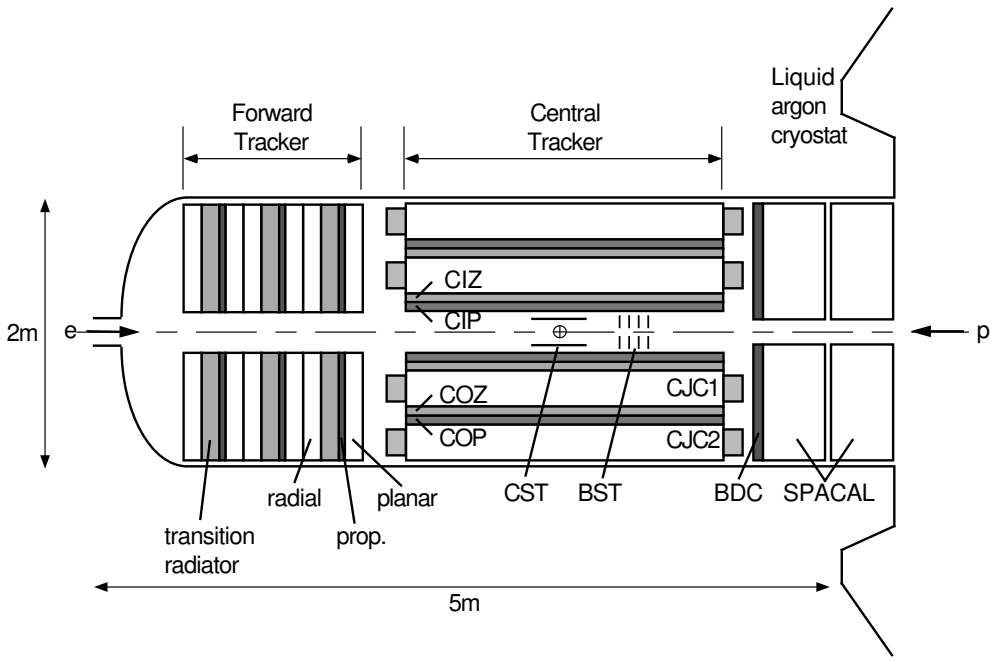

Figure 3.2: Side view of the H1 tracking system.

3.1.1 Central and Forward Track Detectors

Two large concentric drift chambers (CJC1 and CJC2) are the basis for track reconstruction in the central region of H1. Wires 2.2 m long are strung parallel to the beam (z-direction) with the drift cells inclined by about 30° with respect to the radial direction. A magnetic field of 1.15 T is provided by a superconducting cylindrical coil with a diameter of 6 m and a length of 5.75 m enclosing the main calorimeter. By choosing this location the amount of dead material in front of the calorimeter and its total weight are minimized. The CJC1 features 30 cells with 24 sense wires each, whereas the CJC2 has 60 cells with 32 wires each. Signals recorded in these chambers are used to determine the transverse track momentum and in addition provide information on the specific energy loss $\mathrm{d}E/\mathrm{d}x$ used to improve particle identification ($\sigma_{dE/dx}\approx 10\%$). The space point resolution in the $r\phi$-plane is 170 μm. The z-coordinate can be determined with a resolution of one percent of the wire length by comparing signals read out at both wire ends. High momentum tracks cross the sense wire plane at least once in CJC1 and CJC2. The passing time of a particle can be determined from the fine match at the crossing to an accuracy of $\sigma\sim 0.5$ ns, thereby allowing the tracks coming from different bunch crossings to be easily separated.

Two thin drift chambers with wires perpendicular to the beam axis measure the z coordinate with better accuracy than possible with charge division and complement the measurement of track momenta. The Central Inner (CIZ) and Central Outer (COZ) z-chambers are located just inside and outside CJC1 respectively. The CIZ is divided into 15 drift cells, the COZ into 24 drift cells with four sense wires per cell in both cases. These two chambers achieve a resolution of typically 300 μm in z and about five degrees in ϕ.

Using signals from all four chambers yields a resolution on the momentum of charged tracks of $\sigma_p/p^2 < 0.01$ GeV^{-1}. The polar angle can be measured to $\sigma(\theta) \approx 1$ mrad.

Two Multi-Wire Proportional Chambers (MWPC) inside the CIZ (Central Inner Proportional Chamber – CIP) and filling the gap between COZ and CJC2 (Central Outer Proportional Chamber – COP) complete the Central Tracker. They deliver a fast timing signal with a time resolution better than the separation of two succeeding HERA bunch crossings. In addition they provide moderately accurate space points for charged particle track reconstruction at the first level trigger (see section 3.4). Both CIP and COP are constructed as a double layer of cells with wires strung parallel to the beam axis. The available segmentation for the CIP is eightfold in ϕ with the double layers rotated by $\pi/16$ with respect to each other and 60 pads in z in each ϕ sector. The segmentation of the COP is 18-fold in z and 16-fold in ϕ.

Three identical supermodules aligned along the z direction form the Forward Track Detector (FTD). Each contains a planar drift chamber, a proportional chamber, a transition radiator, and a radial drift chamber (see Figure 3.2). In this

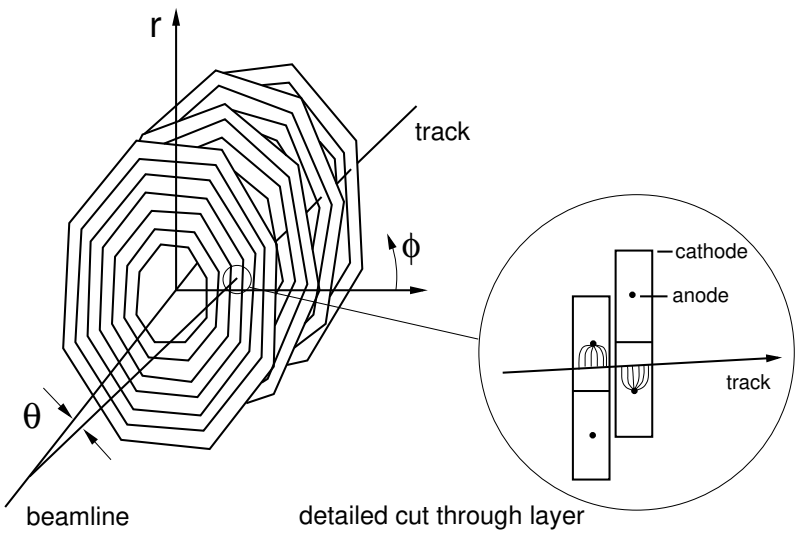

Figure 3.3: Schematic outlay of the four BDC double layers.

analysis only the Forward Multi-Wire Proportional Chambers (FWPC) are used to identify the correct bunch crossing and provide a fast trigger on tracks pointing to the primary interaction vertex (together with CIP and COP). The Forward Multi-Wire Proportional Chambers (FWPC) are mounted directly behind the planar drift chambers in order to share the same gas mixture and maximize the trigger's geometrical acceptance. Each features two wire planes with wires oriented along the vertical (y) direction interleaved with three planes of ring shaped cathode readout pads. A timing resolution of 20 ns was measured using ep data.

3.1.2 The Backward Drift Chamber

The main purpose of the Backward Drift Chamber (BDC) is to measure the direction of the scattered positron in the range $155° < \theta < 178°$ with full azimuthal coverage. This information is then used for the selection of deep inelastic scattering events and to determine their kinematical quantities. Precision therefore has to be achieved first of all in measuring the polar angle (Section 4.2).

The sense wires are strung perpendicular to the beam axis, forming octagons of increasing size resembling a spider's web (Figure 3.3). This causes a radial drift direction in the cells resulting in an optimal resolution in this coordinate. A positron from the primary vertex passes four double layers of drift cells for a maximum of eight space points for the track reconstruction. Each double layer is rotated with respect to the previous one by 11.25 degrees to increase the sensitivity of the ϕ measurement and to avoid the overlap of insensitive regions like the cell boundaries. The drift cells in every second layer are shifted by half a cell width in radial direction

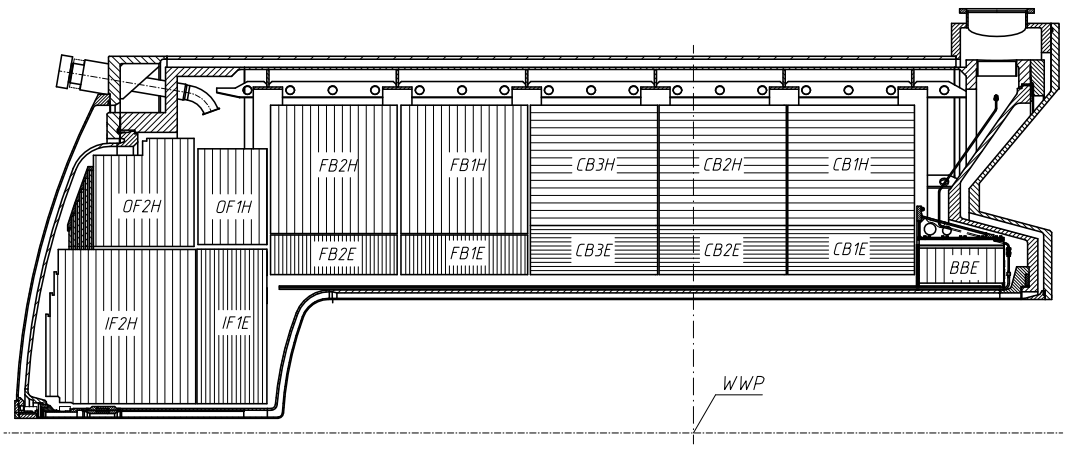

Figure 3.4: Side view of the liquid argon calorimeter.

to resolve the left-right ambiguity. Towards small radial distances from the beam axis one has to cope with an increasing rate of background particles from interactions of the beams with the beam pipe and with residual gas atoms. The BDC therefore features cells of two different geometries. At small radii the maximal drift distance is about 0.5 cm. It increases by a factor of three for cells more than ≈ 25 cm away from the beam axis. Each octant is equipped with 16 small and 16 large drift cells giving a total of 2048 signal channels for eight octants times eight layers.

The resolution on the polar angle of the scattered positron measured in the BDC and including information from the position of the primary vertex has been shown to exceed 0.7 mrad [28].

3.2 Calorimetry

The calorimetry of the H1 detector includes four subdetectors: The Liquid Argon (LAr) calorimeter, The SPAghetti CALorimeter (SPACAL), the tail catcher and the plug calorimeters. The LAr calorimeter is the main calorimeter of H1. It covers the central and forward part of the detector. Energy measurement in the backward region is provided by the SPACAL. Tail catcher (leakage of energy from the LAr) and plug calorimeters (energy measurement close to the beamhole) are not used in this analysis. Only LAr and SPACAL are therefore discussed below.

3.2.1 Central and Forward Calorimetry

The measurement of energies in the central and forward part of the detector is provided by the Liquid Argon (LAr) sampling calorimeter. The LAr covers the

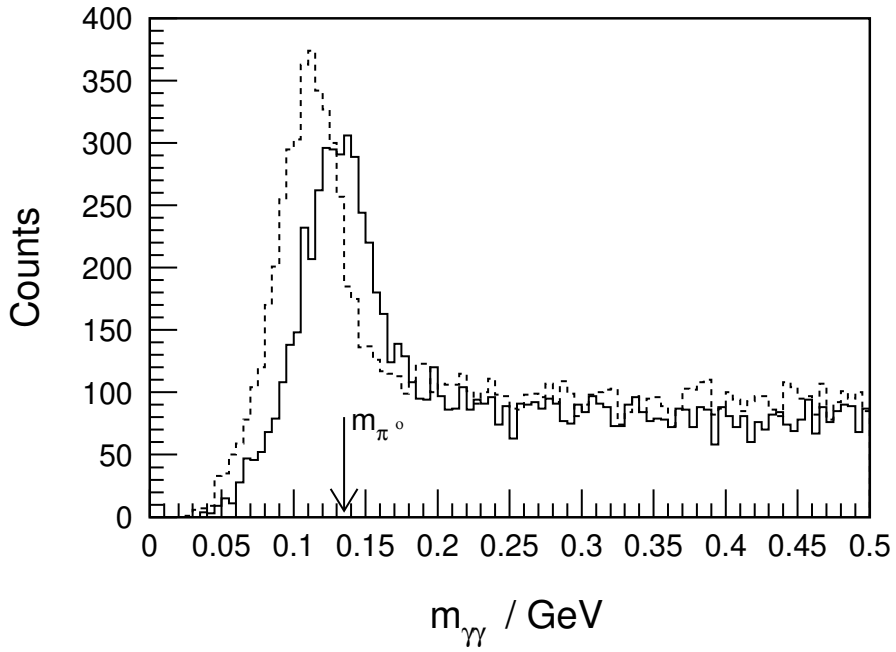

Figure 3.5: Position of the di-photon invariant mass peak before (dashed line) and after (solid line) the correction for uninstrumented material.

polar angular range between $4° < \theta < 154°$. The main reasons for employing the liquid argon technique are good stability, ease of calibration, the homogeneity of the response and the fine granularity which can be achieved with such a calorimeter. The calorimeter is housed in a cryostat inside the main solenoid coil to minimize both the amount of dead material in front of the calorimeter and the overall size and weight of the calorimeter. Figure 3.4 shows a side view of the LAr calorimeter. The segmentation along the beam axis is done in eight self supporting wheels, each of them segmented in ϕ into eight identical stacks or octants. The two forward wheels (on the far left in Figure 3.4) are assembled as two half rings in an effort to minimize dead regions due to cracks. Every wheel of the LAr is divided into an inner electromagnetic and an outer hadronic section. The only exception is the BBE, which only has an electromagnetic section.

The electromagnetic part of the calorimeter consists of 2.4 mm thick lead absorber plates with 2.35 mm liquid argon as active material. The total thickness varies between 20 and 30 radiation length. The energy resolution of the electromagnetic section has been determined in test beam measurements to be $\sigma_E/E \simeq 0.12/\sqrt{E} \oplus 0.01$ where E is given in GeV. The hadronic sampling cells consist of 19 mm stainless steel absorber plates with a double gap of 2.4 mm liquid argon. The hadronic section represents between 5 and 8 interaction length in total. The energy resolution in the hadronic section is $\sigma_E/E \approx 0.50/\sqrt{E} \oplus 0.02$, with E given in GeV.

The calorimeter is highly segmented in both sections, with three-fold or four-fold longitudinal segmentation in the electromagnetic part and four-fold to six-fold longitudinal segmentation in the hadronic section. Cells sizes are between 10 and $100\,\mathrm{cm}^2$ in the electromagnetic section and between 50 and $2000\,\mathrm{cm}^2$ in the hadronic part of the calorimeter. The total number of readout cells is about 45000. Especially interesting for this analysis is the very fine granularity in the forward part of the electromagnetic calorimeter (IF1E and FB2E in Figure 3.4), which is four-fold in the longitudinal direction with typical cell sizes of $3.5 \times 3.5\,\mathrm{cm}^2$. It allows a detailed analysis of the shower forms developing in the calorimeter.

The energy measured has to be corrected for the losses absorbed in dead material in front of the calorimeter and in cracks between the calorimeter stacks. These losses can be up to 10 % of the energy deposited in the calorimeter in low Q^2 DIS events [29]. An example for the effect of the dead material correction for experimental data is shown in Figure 3.5 for the π°-meson peak in the distribution of the invariant mass of two photons. LAr measured energies entering this analysis are taken on this electromagnetic scale after dead material corrections have been applied, since the interest is in electromagnetic objects only. The response of the calorimeter to hadrons is about 30 % smaller than for electrons of the same energy. A weighting technique is used offline to correct for this effect for analyses which require the measurement of hadronic energies.

The most precise information on the absolute scale of the measurement of electromagnetic energies comes from the analysis of the scattered positron. Here general event properties, like the balance of transverse momentum between scattered positron and hadronic final state, and different methods of determining the event kinematics are used to reduce the scale uncertainty to 3 % (see Figure 3.6). The hadronic energy scale is known to 4 %.

3.2.2 Backward Calorimetry

Calorimetric information in the backward region is mainly provided by a scintillating fiber Spaghetti Calorimeter (SPACAL) with lead absorbers. Incident particles develop into a shower of secondary particles in the lead, which in turn cause the fibers to scintillate. The light is then collected by photo-multipliers. The device is split into two separate parts, the inner electromagnetic and the outer hadronic section (see Figure 3.7). The setup is completed by the backward plug calorimeter located in the iron yoke of the H1 magnet.

The active volume of the electromagnetic part features a lead to fiber ratio of 2.3:1 and is 28 radiation length (250 mm) deep. The remaining energy leakage is negligible for 30 GeV electrons [30]. The small cell cross section of $40.5 \times 40.5\ \mathrm{mm}^2$ is well matched to the Molière radius of 25.5 mm and ensures good electron-pion separation as well as a good position resolution. Corresponding to the larger lateral

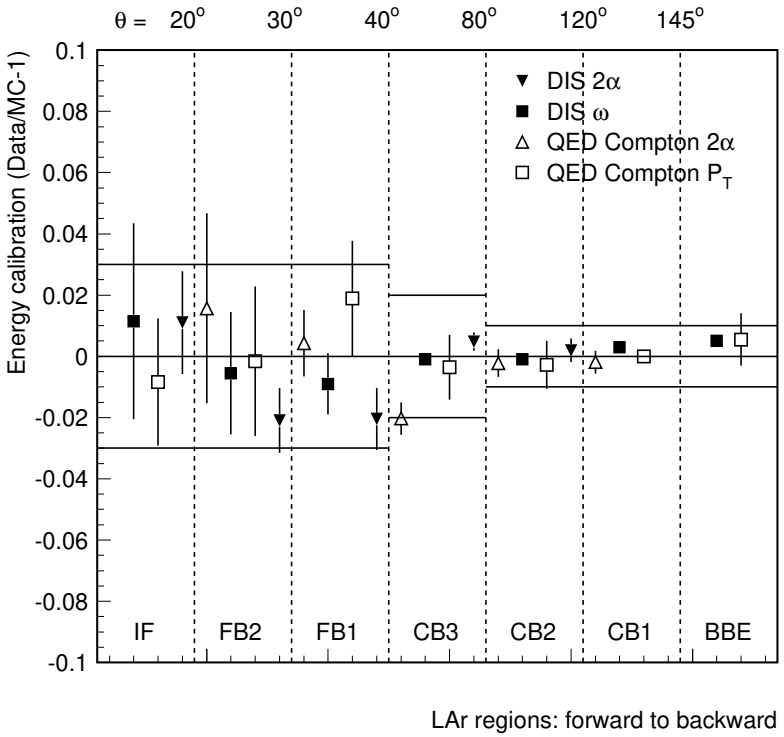

Figure 3.6: Calibration of electromagnetic energies for the scattered positron. Monte Carlo simulations serve as a reference for the calibration. Different processes and methods of reconstructing the event kinematics are used [37].

size of hadronic showers a cell size of 119.3 × 119.0 mm^2 was chosen for the hadronic section. With a lead to fiber ratio of 3.4:1 and a similar depth it adds about one interaction length to the electromagnetic section.

A total of 1328 channels (1192 from the electromagnetic and 136 from the hadronic section) are read out by mesh-type photomultipliers to achieve a time resolution of 1 ns while operating within the strong magnetic field of the H1 main solenoid. The signals are split into three branches: energy, timing and trigger. The excellent time resolution is used to provide time of flight information on energy depositions in the SPACAL for both the electromagnetic and hadronic sections. ToF/AToF energy sums are calculated from the global energies in the SPACAL. An AToF veto rejects background arriving outside a preset time window. Together with the inclusive electron trigger decisions (see section 3.4) the ToF/AToF information is already available for the first level trigger.

The absolute energy scale was originally determined from test beam measurements and has since been extensively checked by various methods, including the study of QED Compton processes, invariant mass reconstruction of π°-mesons, and the comparison of the measured energy of the scattered positron to the prediction

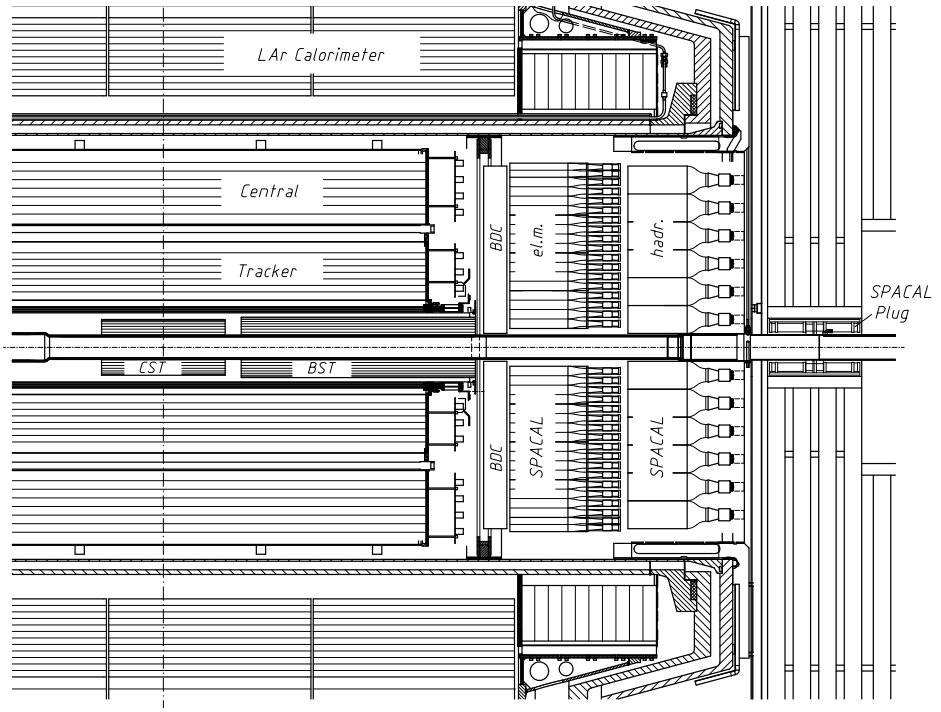

Figure 3.7: Side view of the backward region of the H1 detector. The location of the SPACAL sections and the BDC in the experiment are shown.

obtained from the polar scattering angles of the positron and the hadronic final state. The uncertainty of the absolute energy scale has thereby been demonstrated to be less than 1 %. Energies in the electromagnetic section can be measured with a resolution of [30]

$$\frac{\sigma_E}{E} = \frac{(7.1\pm0.2)\%}{\sqrt{E/GeV}} \oplus (1.0\pm0.1)\%.$$

3.3 Luminosity System and Time of Flight Counters

One of the vital ingredients of any cross section measurement is the precise determination of the integrated luminosity represented by the data. Any uncertainty here will very directly influence the quality of the measurement. A common strategy to determine the luminosity is to measure the rate of the events of a reaction with a well known cross section. In H1 the Bethe-Heitler process $ep \to e\gamma p$ is used for this purpose.

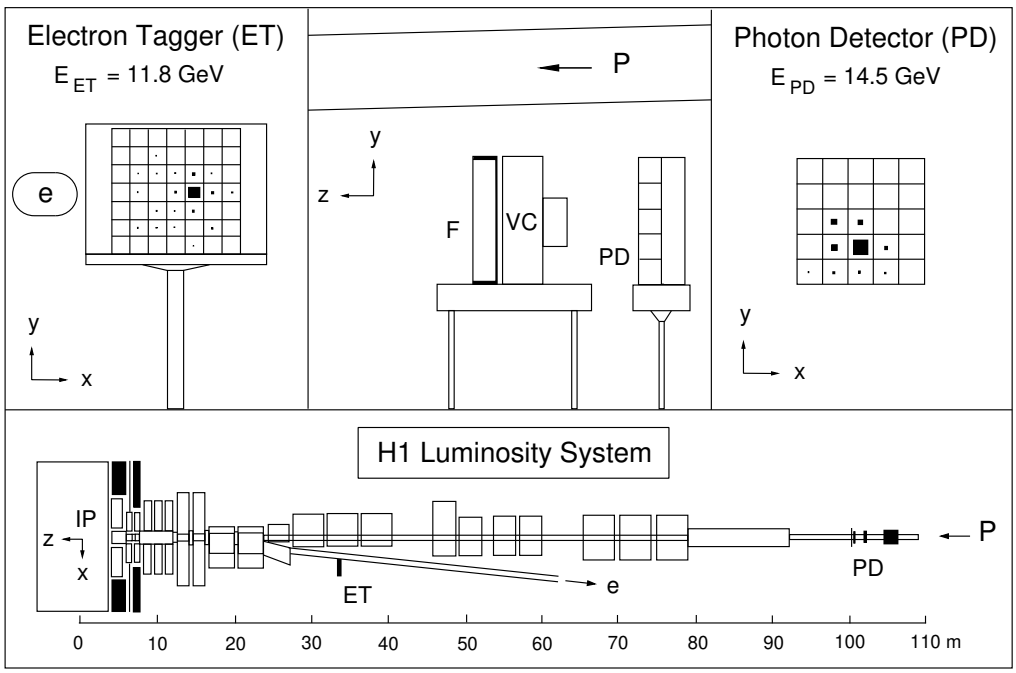

Figure 3.8: The H1 luminosity system.

The layout of the luminosity system is shown in Figure 3.8. Two principal components are available for the measurement of the positron and photon respectively. The Electron Tagger (ET) is installed close to the positron beampipe at $z = -33.4$ m, and the Photon Detector (PD) at $z = -102.9$ m next to the proton beam pipe. Both devices are hodoscopes of total absorption KRS-15 crystal Cerenkov counters chosen for their high radiation resistance, good energy, coordinate and time resolution. Scattered positrons are deflected by a set of low-beta quadrupoles and a bending magnet before they pass an exit window at $z = -27.3$ m and hit the ET. The photons leave the proton beam pipe where it bends upwards at $z = -92.3$ m before reaching the PD. A Pb filter (2.2 X_0) followed by a water Cerenkov veto counter (VC, 0.8 X_0) shields the PD from the high synchrotron radiation flux. To minimize radiation damage the detectors are mounted on movable platforms which are retracted during beam injection.

Two different methods are used to determine the luminosity. The coincidence mode requires the simultaneous detection of positron and photon. Information thus obtained is used as feedback in the steering phase of the colliding beams and to determine the relative luminosity during data taking. Later on in the analysis the single photon method measures the integrated luminosity $\mathcal{L}$ by counting the number of Bethe-Heitler events (N_{BH}) with the photon energy above a certain threshold. The simple relation $\mathcal{L} = N_{BH}/\sigma_{BH}$ has to be extended to account for the photon

energy threshold, the available detector acceptance and background effects:

$$\mathcal{L} = \frac{N_{BH}^{ep}(E_\gamma > E_{min})}{\sigma_{BH}(E\gamma > E_{min})} = \frac{\frac{\sum_i (W_i^{tot}(E_{min}) - W_i^{bgr}(E_{min}))}{\epsilon_{trig}(E_{min})}(1 - \delta_{n\gamma}(L, E_{min}))}{\sigma_{BH}(E_{min}) \cdot A_\gamma(\Theta_x, \Theta_y)}, \qquad (3.3)$$

where $W_i = P_i N_i$ denotes the total and the background number of events in part i of the data. The principal source of background events is bremsstrahlung from the residual gas in the beam pipe. Their frequency can be determined using data from positron pilot bunches (e-bunches without colliding p-bunches) and is about 10% of the $ep \to e\gamma p$ rate at design luminosity. E_{min} is the lower threshold of the photon energy in the PD used in the analysis. It is chosen such that the final systematic error is minimized, usually at about 10 GeV. A_γ represents the correction applied for the limited acceptance of the PD. It depends on the tilt (Θ_x, Θ_y) of the lepton beam. The probability of detecting more than just one photon in the same bunch crossing (pile-up effect) is taken into account by the luminosity and E_{min} dependent $\delta_{n\gamma}$. After applying all corrections the final uncertainty of the luminosity measurement is ~ 3 %.

In addition to the above tasks the ET of the luminosity system is used to detect and trigger on scattered positrons at very low values of the four momentum transfer $Q^2 < 0.01$ GeV^2.

The time-of-flight counters are a set of rather simple but very important devices to counteract the influence of background arising from unwanted reactions of the beam particles with, for example, residual gas particles. The concept of these detectors is based on the precise timing knowledge of the bunch crossings in the detector provided by the HERA machine (HERA clock). A time window is set depending on the respective position of the counters. Their position determines the time of flight particles from nominal ep interactions will take to reach the counters. Background particles give themselves away by arriving outside the designated time interval. Such devices are installed in the backward $(-z)$ direction between the endcap of the iron return yoke and the beampipe (Backward ToF, BToF), and in the forward direction around the beampipe at $z = 5.2$ m (Forward ToF, FToF). In addition, several unused gaps in the PLUG absorber have been instrumented similar to FToF and BToF. They form the PLUG ToF (PToF). Finally a double wall of counters known as the Veto Wall is positioned at $z = -6.5$ m and $z = -8.1$ m. Scintillators are chosen for these detectors for their good time resolution of ≈ 2 ns. Time of flight information is also provided by the SPACAL calorimeter close to the beampipe in the backward direction (see section 3.2.2).

3.4 Triggering and Data Acquisition

The task of the trigger system is to select ep interactions of physics interest in the data flow from the detector and to reject background. H1 is equipped with a multi-level (L1 – L5) trigger system for this purpose. The first level trigger L1 is a dead time free system which provides a trigger decision after 2.5 μs. Since bunch crossings in HERA occur every 96 ns the full event information is stored in pipelines until the L1 decision is reached. The event is kept if one of the 128 L1 subtriggers is fired. Subtriggers are simple logical combinations of the trigger signals from the detector components (trigger elements).

The most important L1 trigger elements for this analysis are provided by the backward calorimeter SPACAL (Section 3.2.2): the inclusive electron trigger (IET). These trigger elements are intended to recognize the positron from a deep-inelastic event if it is scattered under small polar angles and consequently hits the backward calorimeter. In total 320 arrays of 4×4 neighboring cells (IET-windows) are defined for the electromagnetic section of the SPACAL. The IET-windows overlap to avoid efficiency gaps at the borders. In each window the sum of the energy registered inside the time-of-flight window is computed and compared to three different thresholds: IET$>$ 0 ($\gtrsim$ 2 GeV), IET$>$ 1 ($\gtrsim$ 5 GeV) and IET$>$ 2 ($\gtrsim$ 15 GeV). If the signal inside any IET-window exceeds one of the discriminatory thresholds, a corresponding trigger bit is set. These trigger bits are then used by various subtriggers to reach an L1 trigger decision. In 1996 the IET was affected by the 'hot spot', a small region of beam related activity in the backward calorimeter close to the beampipe. The hot spot caused a high (background) trigger rate in the central part of the IET, which was then separated logically from the outer region to allow necessary adjustments of the trigger system. The information about which trigger element and subtrigger was fired is fed into the data stream for every accepted event and can be used for further analysis.

The second level trigger L2 provides the opportunity to verify the L1 decision by employing more sophisticated algorithms which are, for example, sensitive to certain event topologies. The L2 decision is available after 20 μs. No additional L2 condition was used in this analysis. Once the positive trigger decision is reached, the complete event information is read out and transfered to the fourth-level trigger (L3 is currently not used). The rate of accepted events is typically a few 10 Hz. L4 is a software filter farm with 30 parallel processors. With the full event information available the remaining number of background events is further suppressed before the events are written to tape. About 1 % of the rejected events are written to a separate file (L4 reject tapes) for monitoring purposes. At the last level L5 the events are fully reconstructed and classified according to criteria provided by the analysis working groups. These events are usually the starting point for any physics analysis. Non-classified events are rejected and again 1 % is kept in a separate file (L5 reject tapes).

The data is taken in separate 'runs' of events. The idea is to have stable conditions for any given run. A new run is started whenever the setup of the experiment changes. This concerns changes in the trigger setup, the availability of the subsystems, and so on. A typical run contains a few 10 k events.

3.5 Detector Simulation

The reconstructed experimental data constitute a convolution of the positron-proton scattering event with the intrinsic resolution of the detector. The effects of the detector have to be unfolded from the measured data. The basic strategy employed is as follows:

(I) The physics process under study is simulated according to a theoretical model.

(II) The four-momenta and particle identities are fed into the full H1 detector simulation H1SIM. H1SIM is based on the detector simulation package GEANT [31]. In H1SIM the details of geometrical acceptance and intrinsic resolution of every detector component and the distribution of instrumented and uninstrumented material are implemented and used to compute the detector response to the simulated event.

(III) After the simulated events are processed by H1SIM they are subjected to the same reconstruction process as the actual data delivered by the detector read out chain.

(IV) By comparing the events generated in (I) to the reconstructed output of H1SIM one can estimate the influence of the detector on the event signature under study.

In this analysis the event generator LEPTO [23] is used to generate deep-inelastic scattering events. LEPTO uses an implementation of the Leading Log $\ln(Q^2)$ parton shower model (Section 1.9) together with order α_s matrix elements (ME+PS). The generator is run in the framework of DJANGO [32] to account for effects of electroweak radiation.

The procedure should obviously be independent of the theoretical model used in (I). To estimate the influence of the model used, a second set of simulated events is used as well. Here an implementation of the Color Dipole Model (CDM) as implemented in ARIADNE [33] replaces the Leading Log $\ln(Q^2)$ parton shower. Both sets use the string fragmentation scheme provided by JETSET [24] for hadronization. The two sets are labeled MEPS and CDM in the course of this analysis. To estimate background arising from photoproduction processes the event generator PHOJET [34] is used. PHOJET simulates all components of the total photoproduction cross section.

Chapter 4

The Selection of Deep-Inelastic Scattering Events

In this chapter the selection of deep-inelastic scattering (DIS) events from the available data volume is described. Basic quality criteria are applied. The main components and subsystems of the detector must be operational. The conditions under which the data are taken have to be stable, especially concerning the trigger system. DIS events are identified by measuring the scattered positron. The data volume is reduced to a subsample of events with a promising positron candidate at an early stage, which minimizes the handling of events irrelevant to this analysis. The final selection is based on a detailed analysis of the positron candidate.

4.1 Basic Selection of the ep Data Sample

The data on which this analysis is based were taken by H1 during the 1996 running period. The first days and weeks of each running year are used to optimize the overall performance of the detector, and particularly of the trigger system, to the conditions of the running period. The major effect in 1996 relevant for this analysis was a spot of beam related activity in the backward calorimeter close to the beampipe ('hot spot'). Although not associated with the scattering process at the primary vertex, these energy depositions in the multi GeV range fired the triggers composed of backward calorimetric information with a high frequency. The triggers therefore had to be modified in order to ensure a reasonable trigger rate and retain predominantly events which are of interest for physics analyses (see Section 3.4). Only data taken after the triggers became stable are included in this analysis.

Starting from run 157341 (Aug 31st 1996) to the last run 171156 (Nov 29th 1996) the data is first filtered to obtain a subset of runs fulfilling basic quality criteria. Essentially, the major detector components (both the backward and the central

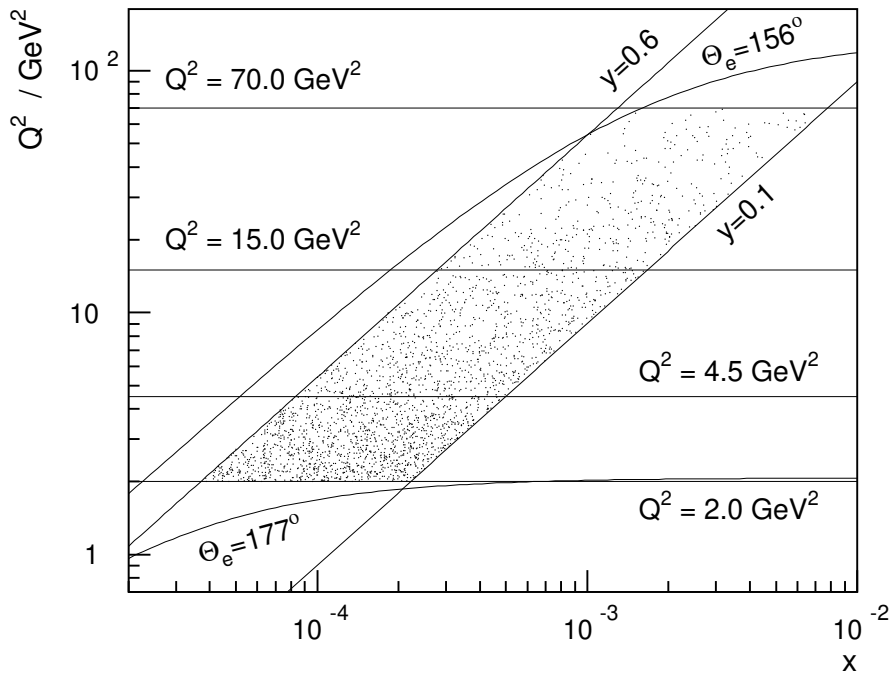

Figure 4.1: The kinematic plane in terms of the invariant quantities Q^2 and x. The scatter points indicate the distribution of deep-inelastic scattering events.

calorimeter, central and backward tracking, the luminosity system and the time of flight counters) are required to be operational during the run. The data available for further analysis then corresponds to an integrated luminosity of 5.8 pb^{-1}. Events must fulfill the conditions of subtrigger s002 (see Section 3.4) to enter the analysis. s002 requires an energy deposition of several GeV in the backward calorimeter and a well defined primary event vertex. The selection of DIS events described below is based on the identification of the scattered positron. Only events with a promising positron candidate are therefore considered. For this analysis a cluster of more than 8 GeV in the backward calorimeter is defined to be such a candidate. After this selection 2.54 M events are left for further analysis.

4.2 The available DIS Phase Space at low Q^2

Deep-inelastic scattering events are identified and event kinematical properties (see Section 1.1) are calculated by using the polar angle and the energy of the scattered positron. The negative square of the four momentum transfer, Q^2, and the

dimensionless y are related to these quantities (neglecting the positron mass) by:

$$Q^2 = 4\,E_e\,E_l\cos^2\frac{\theta_e}{2} \qquad \text{and} \qquad y = 1 - \frac{E_e}{E_l}\sin^2\frac{\theta_e}{2}\,, \tag{4.1}$$

where E_l and E_e are the energies of the incoming and the scattered positron respectively and θ_e is the polar angle of the scattered positron as defined in the H1 coordinate system (see Fig. 3.1). Bjorken-x is then given by $x = Q^2 / (y \cdot s)$, where s is the square of the center of mass energy.

Values of $Q^2 \lesssim 100$ GeV^2 as studied in this analysis are not sufficient to cause large scattering angles for the positron. The available phase space in this case is therefore determined by the backward calorimeter's acceptance for the given parameters of the incident beams. The phase space is defined in terms of invariant quantities only. Requirements concerning the energy and the polar angle of the scattered positron are used during preselection but are later made redundant by restricting the analysis to the range $0.1 < y < 0.6$ and $2.0 < Q^2 < 70.0$ GeV^2. The only exception is a tiny area at the high Q^2 /high y edge of the phase space which causes a very small acceptance correction as shown in Figure 4.1. The isolines for the polar angles $\theta_e = 156°$ and $\theta_e = 177°$ mark the acceptance limits of the backward calorimeter.

4.3 Identification of the Scattered Positron

The positron candidate is always defined to be the most energetic reconstructed cluster of energy depositions in the backward calorimeter. A minimum energy of 10 GeV is required during the searching phase (later made redundant by $y < 0.6$). The positron candidates then have to fulfill a series of quality requirements to keep the contamination by background small. The main source of background are hadrons (especially $\pi°$) which are misidentified as the scattered positron. This can either lead to the wrong event kinematics in a deep-inelastic scattering event or cause events from photoproduction processes to enter the event sample.

The transverse radius of the positron candidate $R_{cl,e}$ has to be smaller than 3.5 cm to reject hadronic clusters, which on average are broader (Figure 4.2 (a)). The prediction produced by the simulation yields values of $R_{cl,e}$ which are systematically too small. The simulated events are therefore shifted by 5 % towards larger values of $R_{cl,e}$ before the cut is applied. This shift is already included in Figure 4.2 (a). The resulting description of the data is sufficient considering that only very few positron candidates in the chosen phase space are rejected by this cut.

With a depth of 28 radiation lengths the SPACAL should fully contain electromagnetic showers caused by the incident scattered positron in the given energy range of less than 30 GeV. Energy depositions in the hadronic part of the SPACAL directly behind the positron candidate cluster are therefore a sign of background.

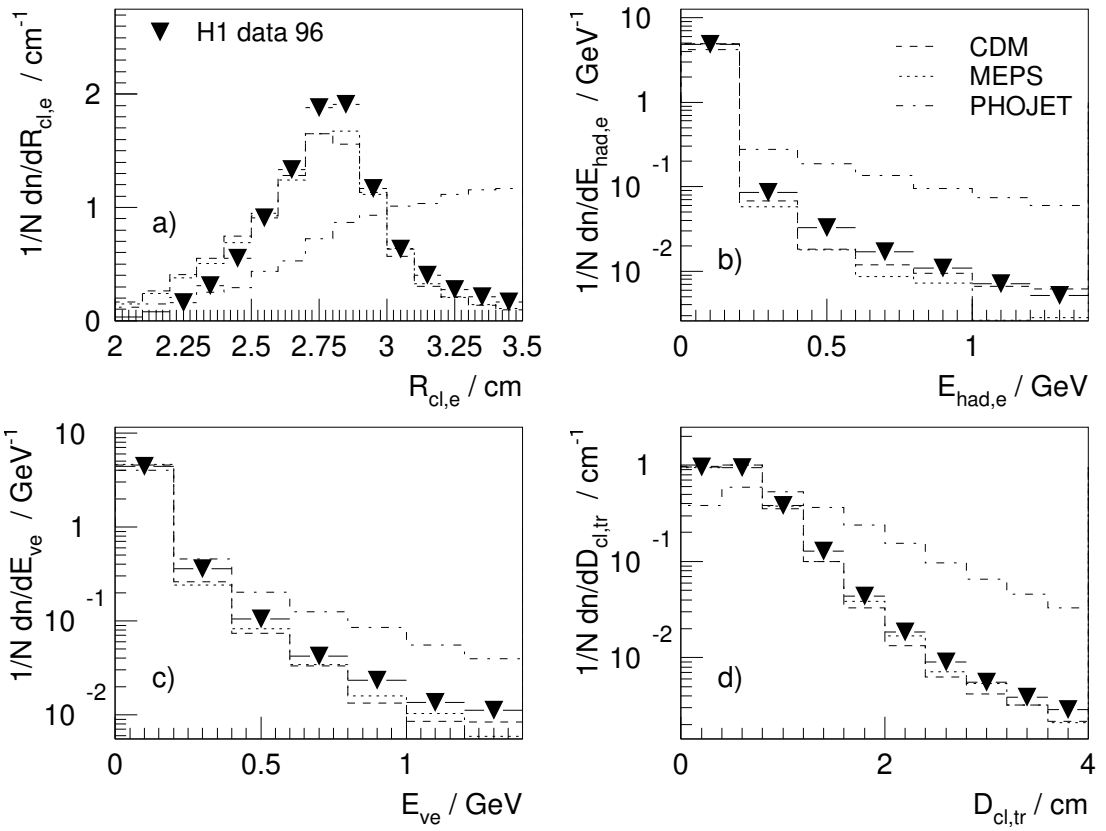

Figure 4.2: Distributions of variables used in the selection of the scattered positron: cluster radius (a), hadronic energy behind the candidate cluster (b), energy in the SPACAL veto layer (c) and the distance of the closest BDC track to the center of gravity of the candidate cluster (d). N denotes the number of events entering the distribution. The overlaid PHOJET [34] Monte Carlo indicates the expected shape of background from photoproduction. The relative contribution from this type of background at this point is already reduced to a few percent by requiring an energetic positron candidate in the SPACAL.

To quantify this, the energy in the hadronic SPACAL inside a cone of a four degree opening angle around the direction of the candidate is summed and the resulting $E_{had,e}$ is required to be less than 1 GeV (Figure 4.2 (b)).

Because the intention is to measure positron candidates down to very small scattering angles of a few degrees, care must be taken to avoid leakage into the beampipe, which would distort the energy measurement. An energy sum (displayed in Figure 4.2 (c)) is formed for this purpose from the depositions in the veto layer. The veto layer consists of four cells directly adjacent to the beampipe. The energy deposit in this layer E_{ve} must not exceed 1 GeV for the candidate to be accepted.

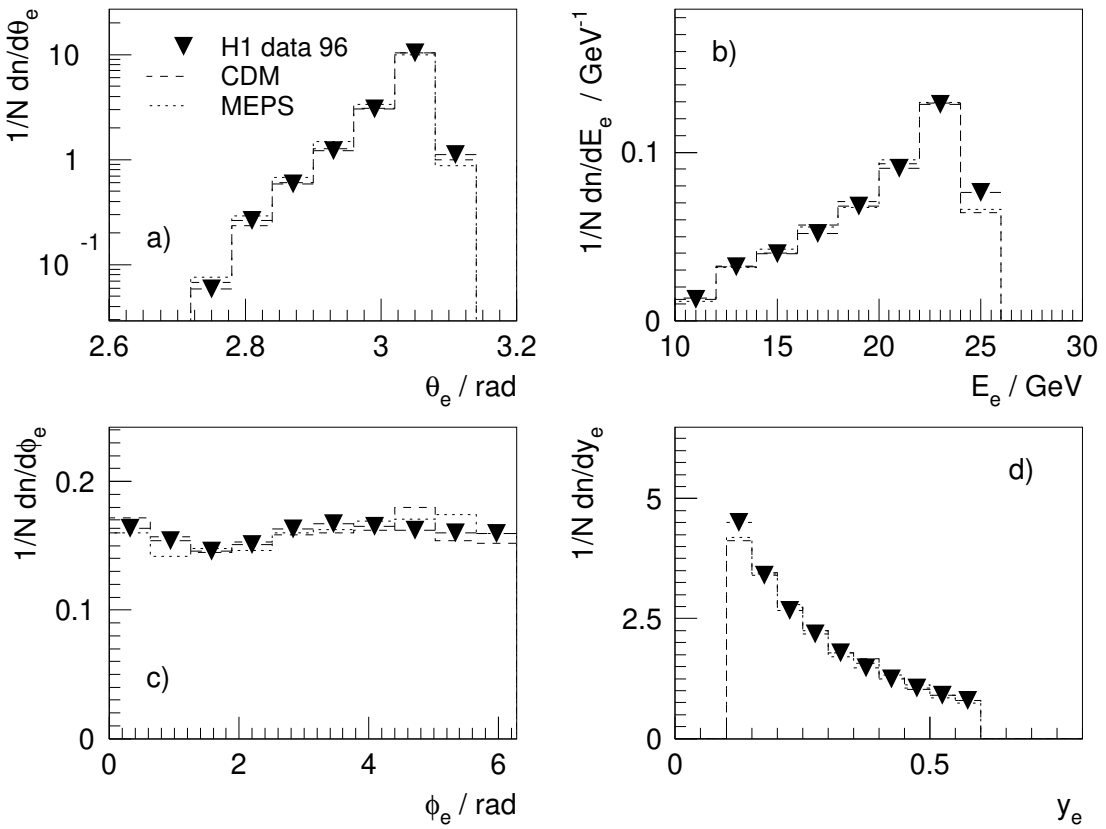

Figure 4.3: Polar angle (a), energy (b) and azimuthal angle (c) of the scattered positron and y as calculated from (θ_e, E_e). N denotes the number of events entering the distribution. To obtain a well defined sample the data and the simulated samples MEPS and CDM only include events triggered by s002 *(see Section 6.2).*

The energy measurement is complemented by directional information taken from the backward drift chamber. The higher resolution (see Section 3.1.2) of the drift chamber (together with the position of the primary vertex) allows a more precise determination of the scattering angle than is possible using the position of the cluster candidate in the SPACAL alone. To ensure that track and cluster candidate correspond, the distance between the closest track and the cluster (center of gravity) $D_{tr,cl}$ (Figure 4.2 (d)) is required to be smaller than 3.5 cm.

In Figures 4.2 (a)-(d) the expected distribution of background events is indicated using the photoproduction Monte Carlo PHOJET [34]. The relative contribution from this type of background at this point is already reduced to a few percent by requiring an energetic positron candidate in the SPACAL. The difference in shape is clearly visible and via the applied cuts leads to a further suppression of this background.

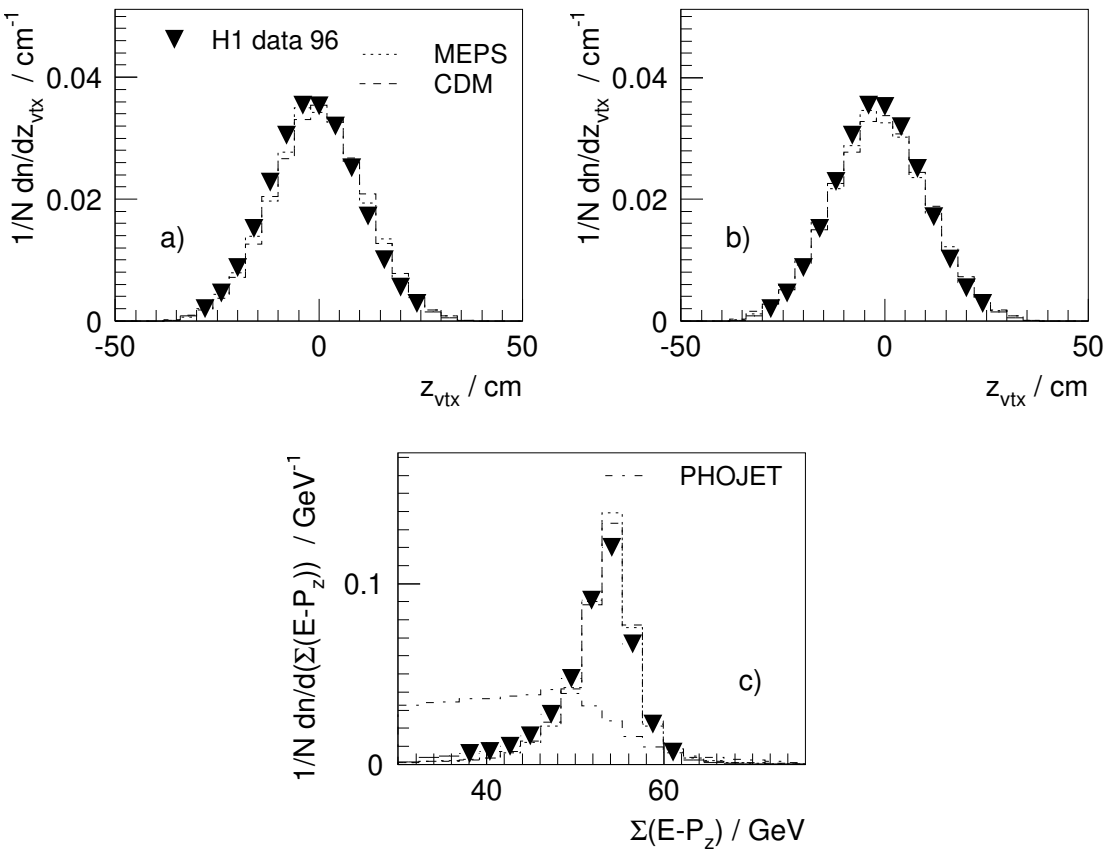

Figure 4.4: The distribution of the z coordinate of the primary event vertex and its description by the detector simulation (a). In (b) the simulated samples CDM and MEPS are reweighted to account for the slight shift visible in (a). Figure (c) shows the distribution of the sum $\sum_j (E_j - p_{z,j})$ over all particles detected in the event. N denotes the number of events entering the distribution. The expected shape of photoproduction background in (c) is again shown using PHOJET.

The polar angle and the energy distribution of the positrons thus selected are shown in Figure 4.3 (a) and (b) respectively. Figure 4.3 (c) and (d) show the positron azimuthal angle and y as obtained by (4.1). Subtrigger s002 is required for all events (data and simulated events) in Figure 4.3 to obtain well defined samples. The slight asymmetry visible in the ϕ_e distribution is due to the setup of s002 in two separate areas with separate trigger thresholds. This effect is corrected for later in the analysis (see Section 6.2).

To reduce the contamination of the event sample by reactions involving residual gas molecules in the beampipe and by events from photoproduction processes, and to suppress events in which a high energy photon is radiated off the incoming positron, additional quality requirements are applied to the event itself.

E hottest cluster ($\Rightarrow$ positron candidate)	E_e	$>$	10 GeV
radius of candidate cluster	$R_{cl,e}$	$<$	3.5 cm
E hadronic behind the candidate cluster	$E_{had,e}$	$<$	1.0 GeV
energy in the SPACAL veto layer	E_{ve}	$<$	1.0 GeV
track cluster distance	$D_{tr,cl}$	$<$	3.5 cm
position of primary event vertex	$\mid z_{vtx} \mid$	$<$	35.0 cm
$\sum_j (E_j - p_{z,j})$ of all detected particles j	$\sum E - p_z$	$\in$	$[35, 70]$ GeV

Table 4.1: Summary of quality criteria applied to the positron candidate and the event itself for the selection of deep-inelastic scattering events.

The reconstruction of the primary event vertex must yield a z coordinate z_{vtx} not more than 35 cm away from the nominal interaction point. The z_{vtx} distribution as implemented in the detector simulation shows a shift with respect to the data (Figure 4.4 (a)). Since z_{vtx} enters the analysis in order to determine the polar angle of both the scattered positron and the final state particles, a good description of the measured distribution is important. The simulated Monte Carlo samples are therefore reweighted to account for the observed shift by using the ratio of Gaussian fits to data and Monte Carlo. Applying the weight to the Monte Carlo samples requires a variable which is well defined for every event. Since the primary vertex will in general not be reconstructed for all events, the value of z_{vtx} as given by the simulation before the reconstruction step (see Section 3.5) is used for this purpose. The data are not altered by this procedure. The result can be seen in Figure 4.4 (b) and shows an improved agreement of the simulated events with the data.

For every event one can calculate the quantity $\sum_j (E_j - p_{z,j})$ with the sum extending over all detected particles in the event. If all particles were detected and perfectly measured, the conservation of energy and longitudinal momentum (considering the opposite signs of p_z for incident positron and proton) would yield twice the energy of the incident positron beam for an ep scattering event. If the scattered positron escapes down the beampipe and a hadron is misidentified as the scattered positron (photoproduction background) the sum will in general yield smaller values. Requiring $35 < \sum_j (E_j - p_{z,j}) < 70$ GeV therefore suppresses this type of background. Photons radiated off the incoming positron and leaving the detector through the beamhole will also distort this quantity.

After all selection criteria have been applied, about 600 k events are left for further analysis.

Chapter 5

Identification of Neutral Pions

The following chapter is devoted to the identification of π°-mesons in the deep-inelastic scattering events selected in Chapter 4. The analysis is concerned with π°-mesons at large energies and transverse momenta. The opening angle of the two photons from the decay of a π°-meson is therefore in general small and the two photons cannot be resolved as single objects in the detector. The method of identifying π°-mesons by reconstructing the invariant mass from their decay products is hence not applicable. Instead a detailed analysis of the showers caused by the photons when absorbed in the calorimeter is used to separate them from the hadronic background. The shower form analysis is based on the description of such showers by the detector simulation. Emphasis is therefore placed on the accurate modeling of the detector response. The quality of the π° selection achieved by this method is demonstrated by determining the angular and transverse momentum resolutions for the π° candidates.

5.1 The π° Phase Space

This analysis is concerned with the production of energetic π°-mesons in the forward direction, i.e. close to the proton remnant (see Section 1.8). The term 'forward' in this case is defined to start from polar angles $\theta_\pi < 25^\circ$. The boundary condition for the lowest possible θ_π is given by the detector acceptance and taken to be $\theta_\pi > 5^\circ$. The θ_π range is thus partly motivated by the conditions present in the laboratory system of reference. For this reason the cut on θ_π is also applied in that frame. Similarly, the minimal energy requirement for each candidate expressed by the condition $x_\pi = E_\pi \,/\, E_{proton} > 0.01$ must be fulfilled within the laboratory system for the analysis strategy explained in the next section. The minimum transverse momentum required of the π° is however motivated only by the physics processes that are to be studied, the dynamics of which can more easily be separated from the event kinematics in the center of mass system of the virtual photon and the proton

(hadronic cms). The condition $p_{T,\pi} > 2.5$ GeV is therefore to be understood in the hadronic cms. Table 5.1 summarizes the definition of the phase space in which the measurement is carried out.

DIS selection	π° selection	frame of ref.
$0.1 < y < 0.6$	$5^\circ < \theta_\pi < 25^\circ$	lab.
$2.0 < Q^2 < 70.0$ GeV^2	$x_\pi = E_\pi \,/\, E_{proton} > 0.01$	lab.
	$p_{T,\pi} > 2.5$ GeV	hcms

Table 5.1: Summary of the conditions defining the phase space in which the measurement of forward π° cross sections is carried out.

5.2 Selection Strategy

The π°-mesons are measured via the dominant decay channel $\pi^\circ \rightarrow 2\gamma$ with the branching ratio $\Gamma_i(2\gamma)/\Gamma \sim 99$ %. With a $c\tau = 25.1$ nm [3] the lifetime of the π° can be neglected here for all practical purposes. For the phase space defined in the previous section the two decay photons from a π° produced at the primary vertex will traverse part of the central tracker and the forward track detector before being absorbed by the LAr calorimeter (see Chapter 3). Unless converting to an e^+e^- pair in some material in between, they will not leave a trace in the track detectors, which are only sensitive to particles carrying an electric charge. The amount of uninstrumented material in the detector has been studied for the analysis of charged particle spectra [19] and was found to be well described by the detector simulation.

The π°-mesons are therefore measured using calorimetric information only. Since the analysis is concerned solely with the high energy part of the π° spectrum, the opening angle of the two photons from a π° decay will be small. Figure 5.1 (a) shows the mean and the minimal opening angle as a function of the π° energy. Larger opening angles can still occur for high π° energies if the decay is asymmetric. Figure 5.1 (a) however demonstrates that the mean value of the opening angle for π° energies above 8 GeV is close to the minimal value allowed by four-momentum conservation. Asymmetric decays with large $\gamma\gamma$ opening angles hence constitute only a small portion of all π° decays. If the decay vertex is assumed to coincide with the nominal interaction vertex, the opening angle can be used to calculate the distance between the two photons on the surface of the forward LAr calorimeter (IF, see Figure 3.4) as shown in Figure 5.1 (b) for the case of Φ_{min}. An example of such a two photon configuration in the calorimeter can be seen in Figure 5.2 for a π° decay taken from a simulated event. The energy depositions in the calorimeter cells are

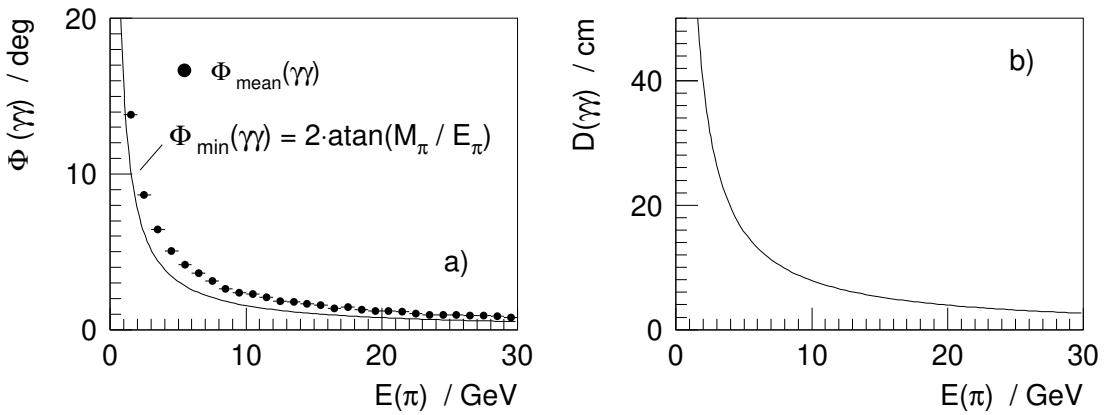

Figure 5.1: Mean and minimal opening angle of two photons from the reaction $\pi^\circ \rightarrow 2\gamma$ as a function of the π° energy (a). Figure (b) shows the distance between the two photons on the surface of the forward LAr calorimeter (IF, see Figure 3.4) for Φ_{min} if the decay vertex is assumed to coincide with the nominal interaction point.

displayed as a function of azimuthal angle (a) and pseudorapidity (b) relative to the center of gravity of the configuration. The energy of the π° is $\approx$ 14 GeV. Although two distinct peaks caused by the two photons can be seen close to zero, the existing overlap causes the reconstruction program to combine them into one cluster. It can therefore be concluded that at the high π° energies considered here the calorimetric response will yield just one cluster. The standard method of reconstructing the invariant mass from the separate measurement of the two decay photons to identify the π°-meson is hence not applicable.

Instead, a detailed analysis of the longitudinal and transverse shape of the energy depositions is performed. This approach is based on the compact nature of electromagnetic showers as opposed to showers of hadronic origin, which are broader. The analysis of shower forms is made possible by the fine granularity of the H1 LAr calorimeter in the forward direction with a cell size of 3.5×3.5 cm^2 and four-fold longitudinal segmentation for the electromagnetic section (see Section 3.2.1). The showers are returned by the LAr reconstruction program as clusters of energy depositions. The reconstruction is tuned to contain the complete electromagnetic shower in one cluster which therefore can be used to identify the parent (electromagnetic) particle(s). Showers of hadronic origin will predominantly be split into several clusters by the reconstruction. A set of shape estimators serves to statistically select clusters caused by electromagnetic particles. Since the only significant source of such particles in the phase space considered are photons from the decay of π°-mesons, they can be used to statistically identify these π°-mesons.

In order to select a class of candidate clusters predominantly initiated by the two decay photons of a π°-meson, the distribution of the shower shape estimators

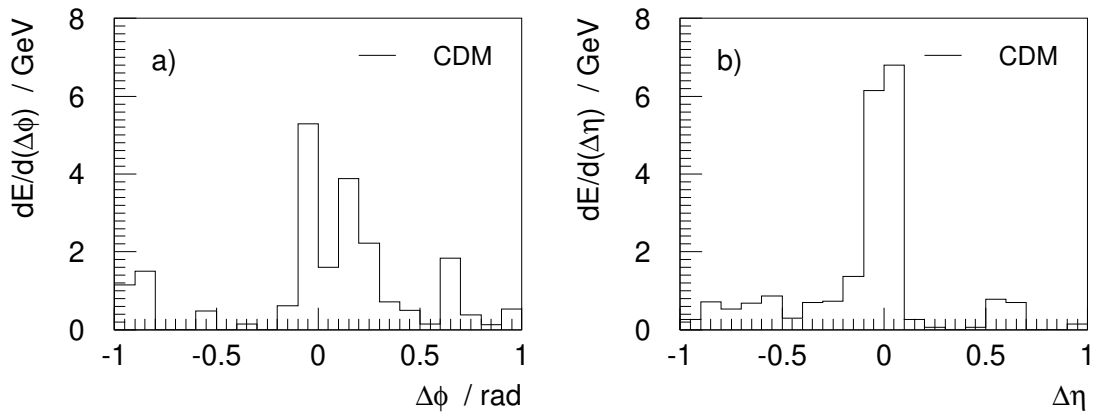

Figure 5.2: Energy depositions in the forward LAr of a two photon configuration from a π° decay taken from a simulated event: (a) as a function of azimuthal angle, (b) as a function of pseudorapidity relative to the center of gravity of the configuration. The energy of the π° is $\approx$ 14 GeV.

are studied separately for the π° signal and the background. For the estimators to be useful, there must be a very distinct difference in their behavior for signal and background.

A set of simulated events is used for this purpose. For these events the direct relationship between the generated particles, the simulated detector response, and the objects returned by the reconstruction program is available. Using this information, the particles associated with a specific cluster and the fraction of the energy they contribute can be determined. Three classes of events are defined accordingly (the contribution of each class in a sample of clusters located predominantly in the electromagnetic LAr is given in brackets):

- **π° signal class** (34 %): clusters with more than 90 % of their energy from a π°-meson (e.g. a well isolated π°)

- **background class** (27 %): clusters with less than 10 % of their energy from a π°-meson (e.g. background particles with no π° nearby)

- **hybrid class** (39 %): clusters with between 10 and 90 % of their energy from a π°-meson (e.g. background particles and π° are close enough together to contribute to the same cluster)

The candidates used for this study are required to fulfill the conditions listed in Table 5.1. The large hybrid class is a striking feature of this analysis. It will be discussed in more detail in the next section.

5.3 Shower Shape Estimators

The shape of the electromagnetic shower, which is taken to be equivalent to the cluster returned from the LAr reconstruction, is quantified by using the information on measured energy and position for every calorimeter cell contributing to the cluster. This method is of course only applicable if the cluster consists of a sufficient number of cells, as is the case here due to the fine segmentation of the calorimeter and the large energies ($E > 8$ GeV) of the cluster candidates considered.

The fraction of electromagnetic energy Ω_{em}

The electromagnetic part of the LAr calorimeter provides more than 20 radiation length for the absorption of electromagnetic showers, which therefore should be well contained in this part of the calorimeter. Hence only clusters located predominantly in the electromagnetic LAr are considered. This is ensured by calculating the quantity

$$\Omega_{\mathrm{em}} = \frac{E_{\mathrm{em}}}{E} = \frac{\sum_j E_j}{\sum_i E_i}, \tag{5.1}$$

where i runs over all cells of the cluster and j only includes those cells of the cluster located in the electromagnetic section of the LAr. Only clusters fulfilling $\Omega_{\mathrm{em}} > 0.8$ are included in the analysis. Figure 5.3 (a-c) shows Ω_{em} for the three classes defined above for simulated CDM events. A clear difference can be observed. The tail towards smaller values of Ω_{em}, representing leakage into the hadronic part of the calorimeter, falls off much more steeply for the signal class than for background and hybrid clusters. The requirement on Ω_{em} is raised to be larger than 0.9 for the final selection.

The fraction of energy in the shower core Ω_{hc}

To exploit the overall compactness of the desired signal clusters, a 'hot core' consisting of the most energetic group of continuous calorimeter cells, which must include the hottest cell, is defined for each candidate:

$$\Omega_{\mathrm{hc}} = \frac{E_{\mathrm{hc}}}{E} = \frac{\sum_k E_k}{\sum_i E_i}\,. \tag{5.2}$$

The number of cells k included varies with the position in the LAr and has been optimized to include about 80 % of the energy of an electromagnetic shower in the core [35]. Again i runs over all cells of the cluster. A very clear difference can be observed for Ω_{hc} in Figure 5.3 (d-f), which peaks close to one for the signal class, but is almost flat for the background. For the hybrid class the estimator is pulled towards lower fractions of the cluster energy contained in the core by additions of

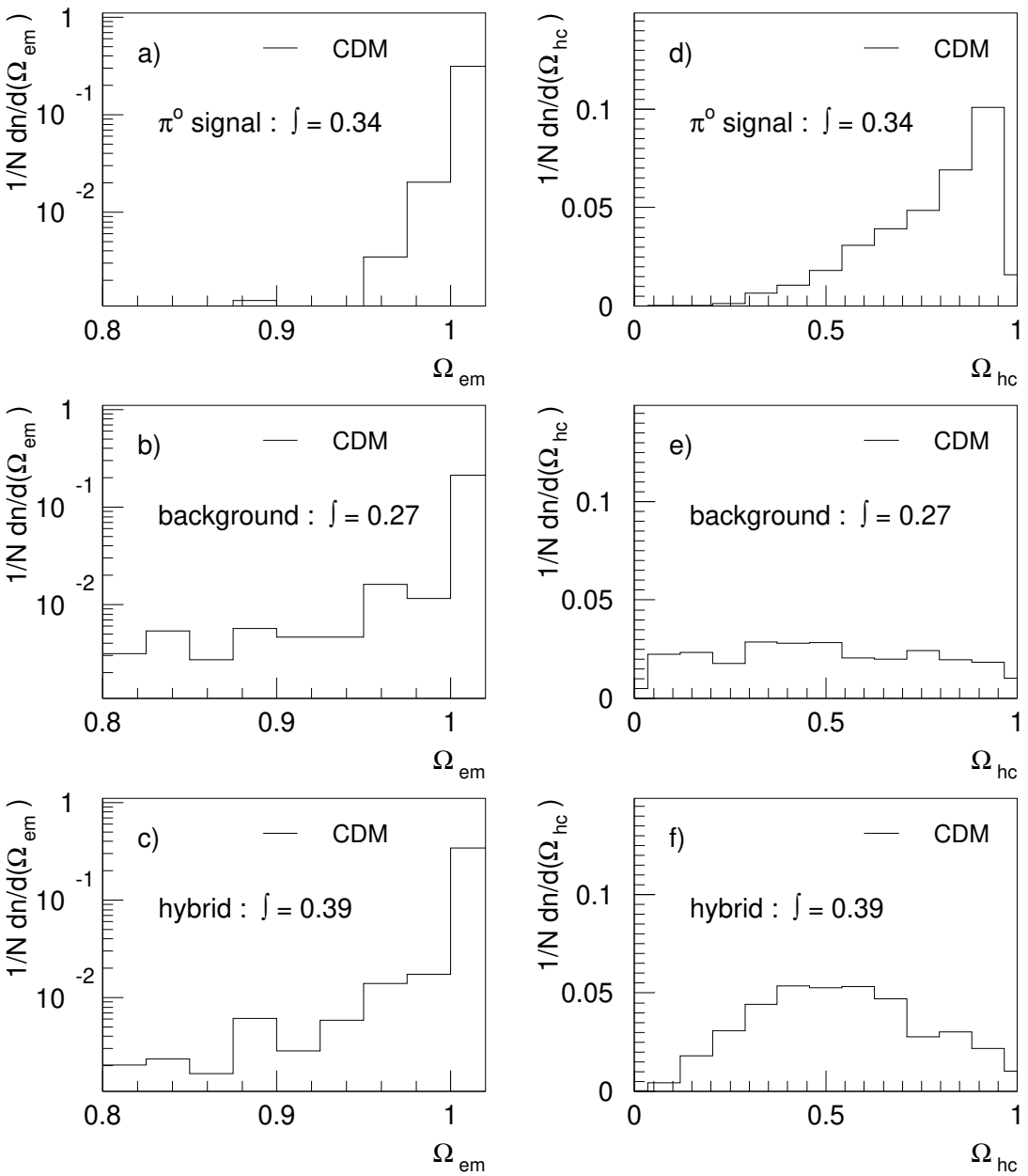

Figure 5.3: The shower shape estimators $\Omega_{\rm em}$ (a-c) and $\Omega_{\rm hc}$ (d-e) for the signal, background, and hybrid class of clusters in simulated events. The distributions are normalized to the number N of clusters studied (all three classes combined). The integral denotes the relative proportions of the three classes.

background energies at the edge of the candidate cluster and by the broader nature of background clusters in general. A cut keeping only clusters with $\Omega_{\rm hc} > 0.5$ suggests itself to reject large parts of the background while retaining most of the signal. For the hybrid class, clusters with small additions of background energies are preferred over those with large additions, which are mostly rejected.

The transverse dispersion of the shower $\Omega_{\rm td}$

The lateral spread of the shower is quantified in terms of lateral shower moments calculated relative to the shower principal axis. The shower axis is obtained as a linear extrapolation from the primary vertex through the energy weighted center of gravity of the cluster. The first and second moments of the cluster are then calculated as

$$\langle r \rangle = \frac{1}{A} \sum_i \frac{E_i \cdot r_i}{V_i}, \quad \langle r^2 \rangle = \frac{1}{A} \sum_i \frac{E_i \cdot r_i^2}{V_i}, \quad \text{with} \quad A = \sum_i \frac{E_i}{V_i}, \tag{5.3}$$

where E_i and V_i are the energy and the volume of a cell and r_i denotes its radial distance from the shower axis. The sum runs over all cells belonging to the cluster excluding cells with negative energies which might occur occasionally due to fluctuations in the noise behavior. One can now define the transverse dispersion $\Omega_{\rm td}$ of a cluster to be

$$\Omega_{\rm td} = \sqrt{\langle r^2 \rangle - \langle r \rangle^2} \ . \tag{5.4}$$

The $\Omega_{\rm td}$ estimator as shown in Figure 5.4 (a-c) demonstrates the larger lateral spread of hadronic showers (i.e. background for this analysis) as compared to the signal class clusters, which are of electromagnetic nature. Clusters belonging to the hybrid class are broadened by the energy additions. The selection criterion based on this estimator keeps clusters with $\Omega_{\rm td} < 4$ cm.

The longitudinal spread of the shower $\Omega_{\rm le}$

The longitudinal shower shape is used as a selection criterion via the fraction of energy deposited in each layer of cells in the electromagnetic part of the LAr calorimeter. The longitudinal segmentation in the area considered (IF and FB2, see Figure 3.4) is fourfold (layer 0...3, 0 is closest to the interaction point). For each cluster the energy deposited in the single layers is summed and used to construct the following longitudinal estimator $\Omega_{\rm le}$:

$$\Omega_{\rm le} = \frac{E_{L1} - E_{L3}}{\sum_{i=0}^{3} E_i} \tag{5.5}$$

Electromagnetic showers are expected to have fully developed shortly after hitting the calorimeter with only small energy deposits in the last layer of the electromagnetic LAr. The longitudinal estimator $\Omega_{\rm le}$ defined above will therefore yield larger

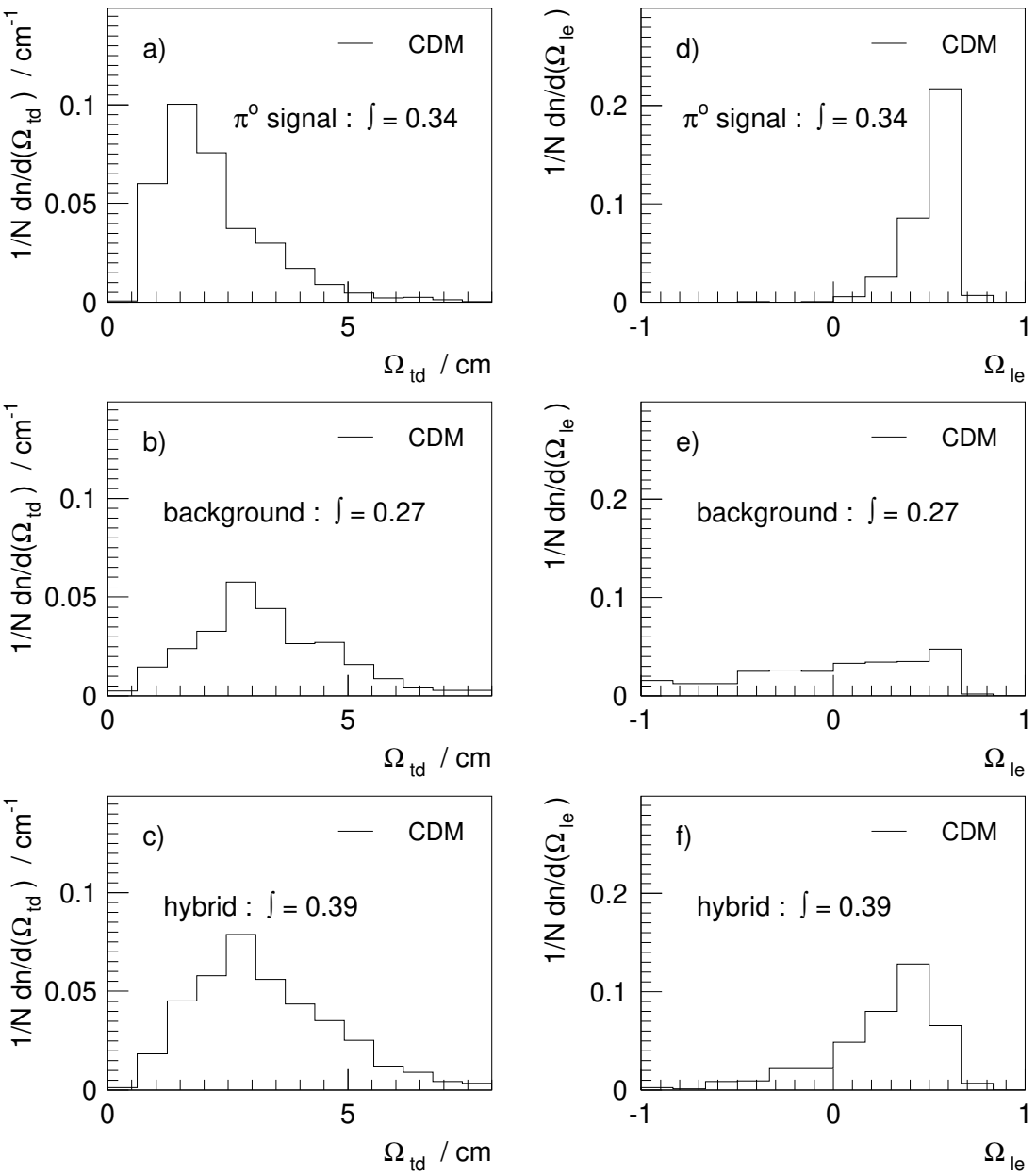

Figure 5.4: The shower shape estimators Ω_{td} (a-c) and Ω_{le} (d-e) for the signal, background, and hybrid class of clusters in simulated events. The distributions are normalized to the number N of clusters studied (all three classes combined).The integral denotes the relative proportions of the three classes.

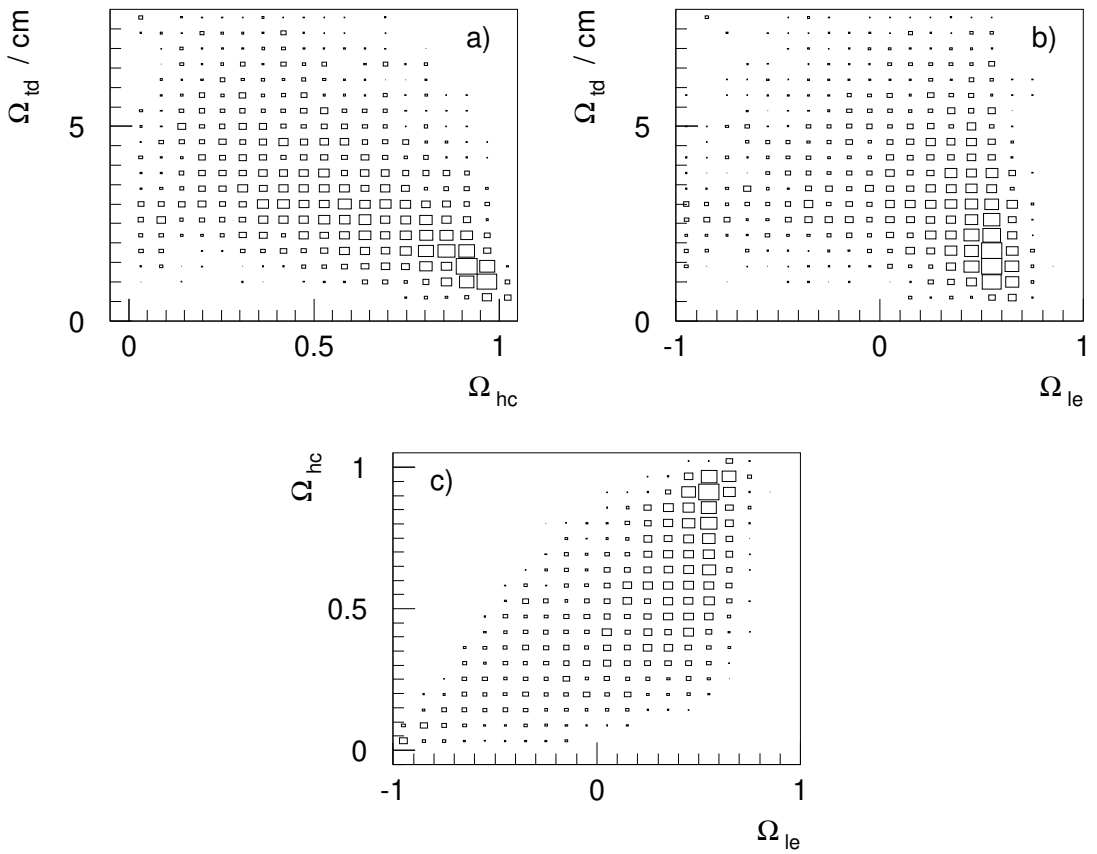

Figure 5.5: Correlations of the shower shape estimators for simulated events (CDM): (Ω_{td}, Ω_{hc}) (a), (Ω_{td}, Ω_{le}) (b), and (Ω_{hc}, Ω_{le}) (c). Signal, background and hybrid type clusters are included.

numerical values for electromagnetic showers than for those of hadronic origin, which start later and develop well into the hadronic part of the calorimeter. The rejection power of the longitudinal estimator Ω_{le} is visible in Figure 5.4 (d-f). The clusters belonging to the signal class indicate that the showers they contain start close to the calorimeter surface and are well contained in the electromagnetic part of the LAr calorimeter. The distribution for the background class suggests showers spreading much further into the hadronic part of the calorimeter. Again the hybrid class of clusters shows the competing influence of electromagnetic and hadronic showers. A requirement of $\Omega_{le} > 0.4$ is chosen for the selection of the signal class.

The distributions in Figures 5.3 and 5.4 are normalized to the number N of clusters studied (all three classes combined). The integral of entries displayed in each figure therefore indicates the fraction of clusters in each class. It becomes immediately evident that the main challenge in this analysis is not the rejection of pure background but the very sizeable hybrid class. It is caused by the high

energy faction in em LAr	$\Omega_{\rm em}$	$>$	0.9
energy fraction in cluster core	$\Omega_{\rm hc}$	$>$	0.5
transverse dispersion	$\Omega_{\rm td}$	$<$	4.0 cm
longitudinal extension	$\Omega_{\rm le}$	$>$	0.4

Table 5.2: Summary of shower shape conditions applied to select π° candidates.

activity in this region of phase space, with hadronic showers 'masking' the clear electromagnetic signature provided by the two photons of a π° decay. This overlap is mainly responsible for losses of π° detection efficiency, since the distortion of the shape estimators it causes will in many cases lead to the rejection of the cluster candidate.

Table 5.2 summarizes the restrictions on the shower shape estimators applied to candidate clusters in selecting π° candidates. Figure 5.5 shows the correlations of $\Omega_{\rm hc}$, $\Omega_{\rm td}$ and $\Omega_{\rm le}$. Although a correlation is visible, it is evident that the application of all three shape estimators does not constitute a redundant procedure.

When the selection criteria in Tables 4.1, 5.1 and 5.2 are applied to the data set described in Section 4.3 about 1700 π° candidates are found.

5.4 Modeling of the Detector Response

The identification of π°-mesons is based on the relationship between generated π°-mesons and reconstructed objects in simulated events. It is evident that in order for this method to be reliable, the behavior of the detector must be well reproduced by the simulation. The modeling of the scattered positron has been tested in many previous analyses as, for example, the determination of the structure function F_2. For the present analysis it is solely the description of the π° candidate and of its immediate vicinity in the detector which is of importance. The main influence here is the particle or energy density surrounding the π° candidate. For the selection method employed the behavior of the cluster candidates is parameterized in form of the shower shape estimators introduced in the previous section. In this section:

- the distributions of the shower shape estimators in the data are compared to two sets of simulated events CDM and MEPS,
- the description is found to be imperfect and the simulated events are reweighted as a function of the particle density (available as the number of secondary interactions, see below),

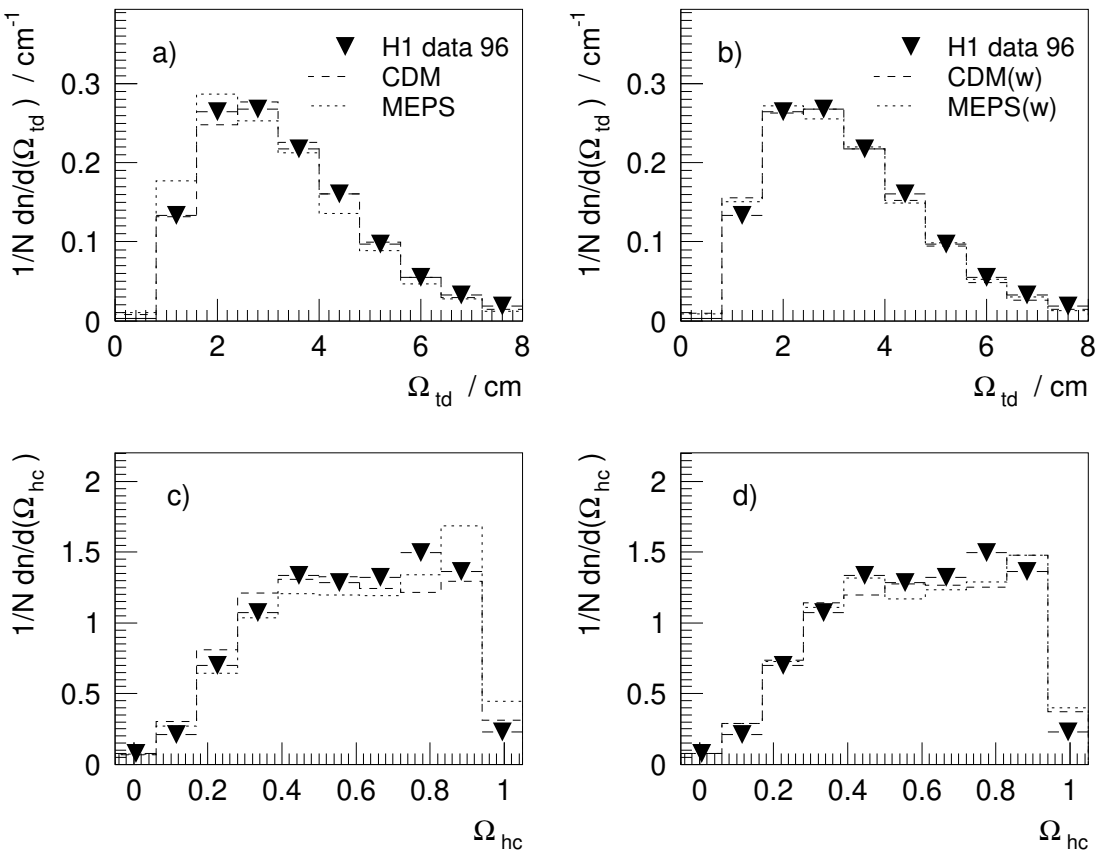

Figure 5.6: The shower shape estimators $\Omega_{\rm hc}$ and $\Omega_{\rm td}$ in the data with two different sets of simulated events overlaid for comparison: (a,c) without, and (b,d) with reweighting of the simulated events. The distributions are normalized to the number N of clusters entering the distribution. Signal, background and hybrid type clusters are included.

- the reweighting is done such that a good description of the transverse shower shapes is achieved,
- the resulting distributions of the shower shapes and the transverse energy flow around a cluster candidate for the simulated events are compared to the data.

Figures 5.6 (a,c) and 5.7 (a,c) compare the two sets of simulated events CDM and MEPS (see Section 3.5) to the data for the four shower shape estimators. It becomes evident especially for the estimators $\Omega_{\rm hc}$ and $\Omega_{\rm td}$ that the description of the data is imperfect. The following should however be noted:

- MEPS predicts on average slightly more compact clusters than seen in the data, while the average cluster in CDM is somewhat broader than clusters in data events.

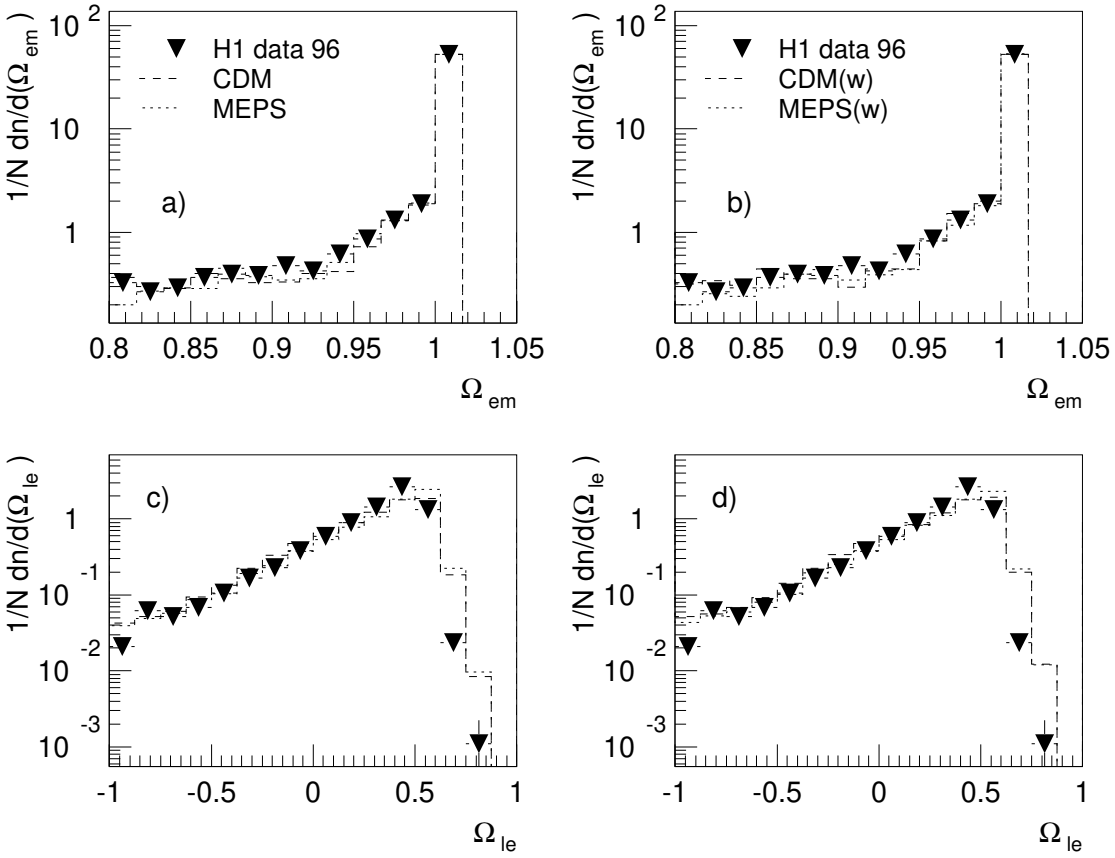

Figure 5.7: The shower shape estimators $\Omega_{\rm em}$ and $\Omega_{\rm le}$ in the data with two different sets of simulated events overlaid for comparison: (a,c) without, and (b,d) with reweighting of the simulated events. The distributions are normalized to the number N of clusters entering the distribution. Signal, background and hybrid type clusters are included.

This behavior is visible, for example, in the distributions of $\Omega_{\rm hc}$ in Figure 5.6 (c). MEPS shows larger values of $\Omega_{\rm hc}$ (more energy in the cluster core), while CDM has on average less energy in the cluster core.

- The data therefore is somewhere in between these two sets of simulated events.
- Differences in the results arising form the choice of either CDM or MEPS can hence be used to estimate the systematic uncertainty associated with the model dependence of the final results.

To reduce this systematic uncertainty the simulated events are reweighted to make their behavior more compatible with the data. The development of electromagnetic showers in detectors like the LAr calorimeter is well known and carefully

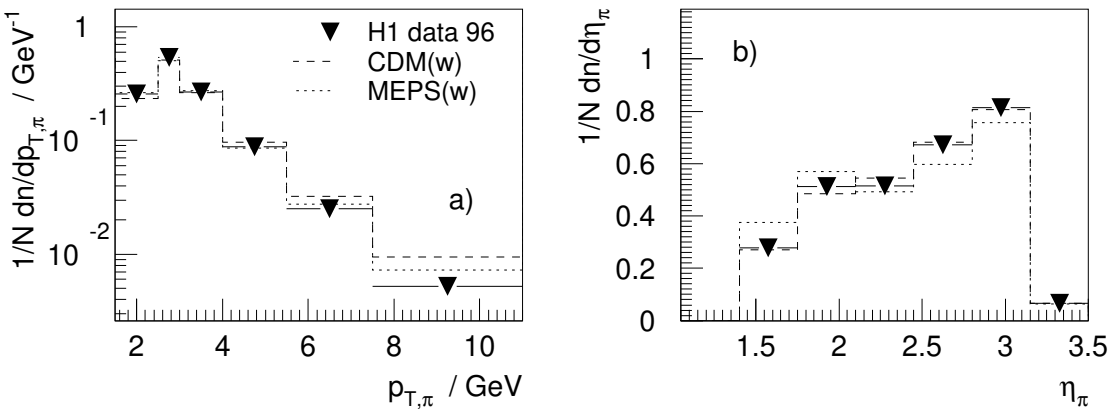

Figure 5.8: Transverse momentum (a) and pseudorapidity (b) of candidate clusters (all classes) and two different sets of simulated events (reweighted) overlaid for comparison. The distributions are normalized to the number N of clusters entering the distribution.

included in the simulation software. The differing shapes of data and simulated events are caused by the environment in which a cluster candidate is found, i.e. the density of particles near a produced π°-meson. Such (background) particles potentially contribute to the energy of the cluster candidate and distort the shower shape estimators. There also is a certain probability that they will undergo interactions with the material they traverse before being absorbed by the calorimeter. The number of vertices of these secondary interactions (known from the simulation) is of

successive cuts $\Rightarrow$		$\Omega_{\rm em} > 0.9$	$\Omega_{\rm td} < 4.0\,{\rm cm}$	$\Omega_{\rm hc} > 0.5$	$\Omega_{\rm le} > 0.4$
			CDM(w)		
π° signal	6162(34%)	6135(35%)	5715(41%)	5380(51%)	4726(63%)
background	4811(27%)	4504(26%)	3262(23%)	1925(18%)	1061(14%)
hybrid	7126(39%)	6905(39%)	4980(36%)	3159(30%)	1719(23%)
			MEPS(w)		
π° signal	9250(37%)	9213(39%)	8672(45%)	8146(55%)	7031(64%)
background	5732(23%)	5268(22%)	4004(21%)	2605(18%)	1402(13%)
hybrid	9824(40%)	9360(39%)	6396(34%)	3973(27%)	2504 (23%)

Table 5.3: The number of clusters left in the three cluster classes defined in Section 5.2 when successively applying the shower shape cuts. The percentages given in brackets denote the fraction of the remaining total number of clusters in each class. The start sample contains clusters with $\Omega_{\rm em} > 0.8$.

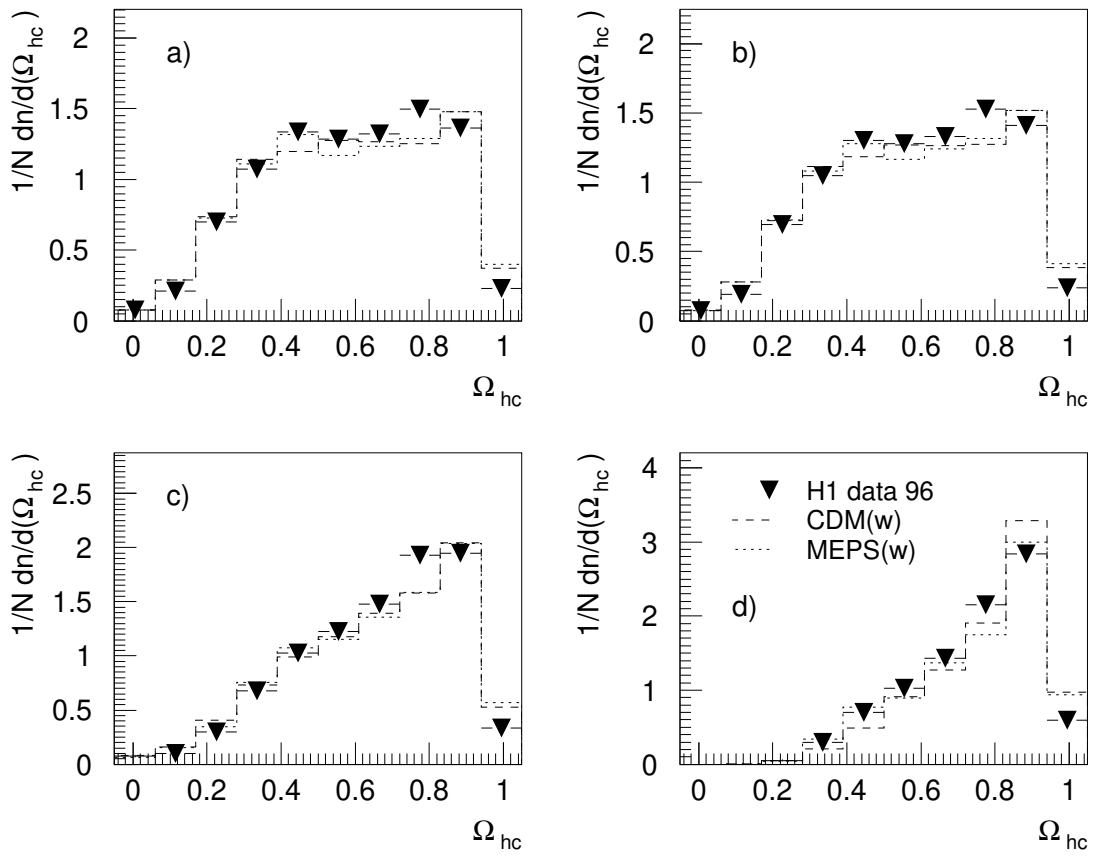

Figure 5.9: Behavior of the estimator $\Omega_{\rm hc}$ with the successive application of the $\Omega_{\rm em}$ (b), $\Omega_{\rm td}$ (c) and $\Omega_{\rm le}$ (d). All cluster candidates fulfill the conditions in Table 5.1. The distributions are normalized to the number N of clusters entering the distribution. Signal, background and hybrid type clusters are included.

course correlated to the particle density. Events with more than about 8 such vertices are weighted up (MEPS) or down (CDM) as necessary to obtain a satisfactory description of the shape estimators as seen in the data. The weights are limited to be less than 3 (MEPS) or larger than 0.3 (CDM) respectively. The data themselves are not altered in the procedure.

Figures 5.6 (b,d) and 5.7 (b,d) show the improved description achieved by the reweighted simulated events. The effect is much more pronounced for the estimators which are sensitive to the transverse shape of the shower, since it is the transverse shower form which is most strongly influenced by the particle density around a cluster candidate. Since the original behavior of the simulated events has been altered, (w) is added to the label of the new curves. In Figure 5.8 the comparison of the simulated events to the data is shown for the transverse momentum and pseudorapidity of candidate clusters. In Figure 5.9 the estimator $\Omega_{\rm hc}$ is used as

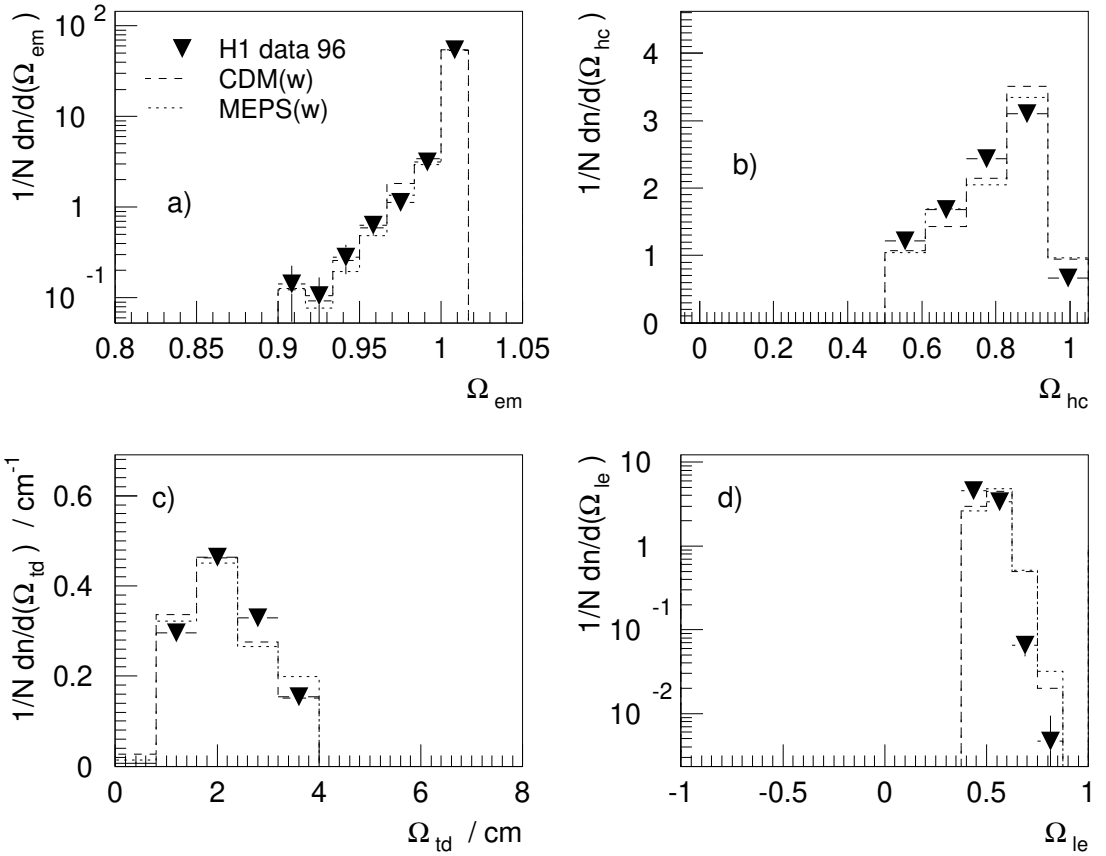

Figure 5.10: The estimators $\Omega_{\rm em}$ (a), $\Omega_{\rm hc}$ (b), $\Omega_{\rm td}$ (c) and $\Omega_{\rm le}$ (d) with all cuts applied. Two sets of simulated events CDM(w) and MEPS(w) are overlaid for comparison. The distributions are normalized to the number N of cluster candidates studied. Signal, background and hybrid type clusters are included.

an example to demonstrate the effect of successively applying the other cluster shape conditions. Every step applied to the data is reproduced by the simulated events. Table 5.3 compares the behavior of CDM(w) and MEPS(w) separately for the three types of clusters (π° signal, background, hybrid) defined in Section 5.2. The number of clusters left in each class when successively applying the shower shape cuts is given. The percentages given in brackets denote the fraction of the remaining total number of clusters in each class. The two simulated samples give compatible predictions concerning the distribution of clusters in the three classes after each cut. The distribution of the four shape estimators after all selection cuts have been applied is shown in Figure 5.10 (a-d).

For a more detailed investigation of the quality of the modeling of π° candidates, the transverse momentum flow around the direction of cluster candidates is studied. Figure 5.11 (a) shows the E_T flow as a function of the distance $R = ((\Delta\phi)^2 +$

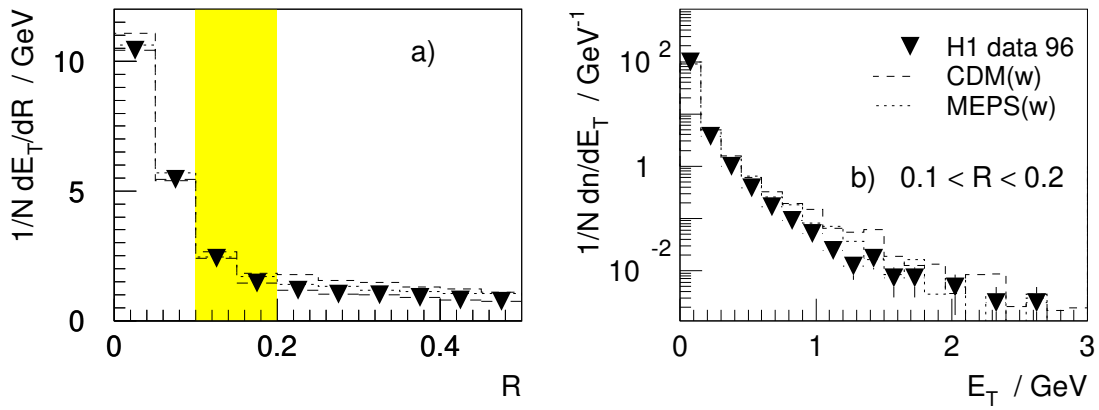

Figure 5.11: Transverse energy flow at distance $R = \sqrt{(\Delta\phi)^2 + (\Delta\eta)^2}$ relative to the direction of the cluster candidate (a). In (b) the E_T spectrum is shown for the shaded area ($0.1 < R < 0.2$) in (a). Two sets of simulated events CDM(w) and MEPS(w) are overlaid for comparison. The distributions are normalized to the number N of cluster candidates studied. Signal, background and hybrid type clusters are included.

$(\Delta\eta)^2)^{1/2}$ relative to the direction of the cluster candidate. In Figure 5.11 (b) the transverse energy spectrum at a distance $0.1 < R < 0.2$ from the direction of the candidate is plotted. Both CDM(w) and MEPS(w) are able to describe the E_T flow. There is, however, a tendency to overshoot the data as one goes further away from the direction of the candidate.

It can be concluded from the above that the behavior of the data is sufficiently well reproduced by the simulation (including the reweighting scheme described above) to serve as a basis for the unfolding of detector effects (see Section 6.3).

5.5 Efficiency, Purity and Resolution of the selected π° Sample

To obtain a measure of the quality of the π° selection described in the previous section one can define an efficiency ϵ_{π° and a purity κ_{π° for finding single π°. Their values are determined using sets of simulated events for which both the number of generated π°-mesons and the detector response are known. To correlate both levels a spatial condition is introduced requiring the reconstructed and the generated object to be closer than 0.2 in the η-ϕ-plane before the two are assumed to be related to each other. This condition is defined wide enough to not impose geometrical acceptance effects on the calculation of ϵ_{π° and κ_{π°. The conditions as described in Table 5.1 are applied. π° candidates are selected from the reconstructed clusters as

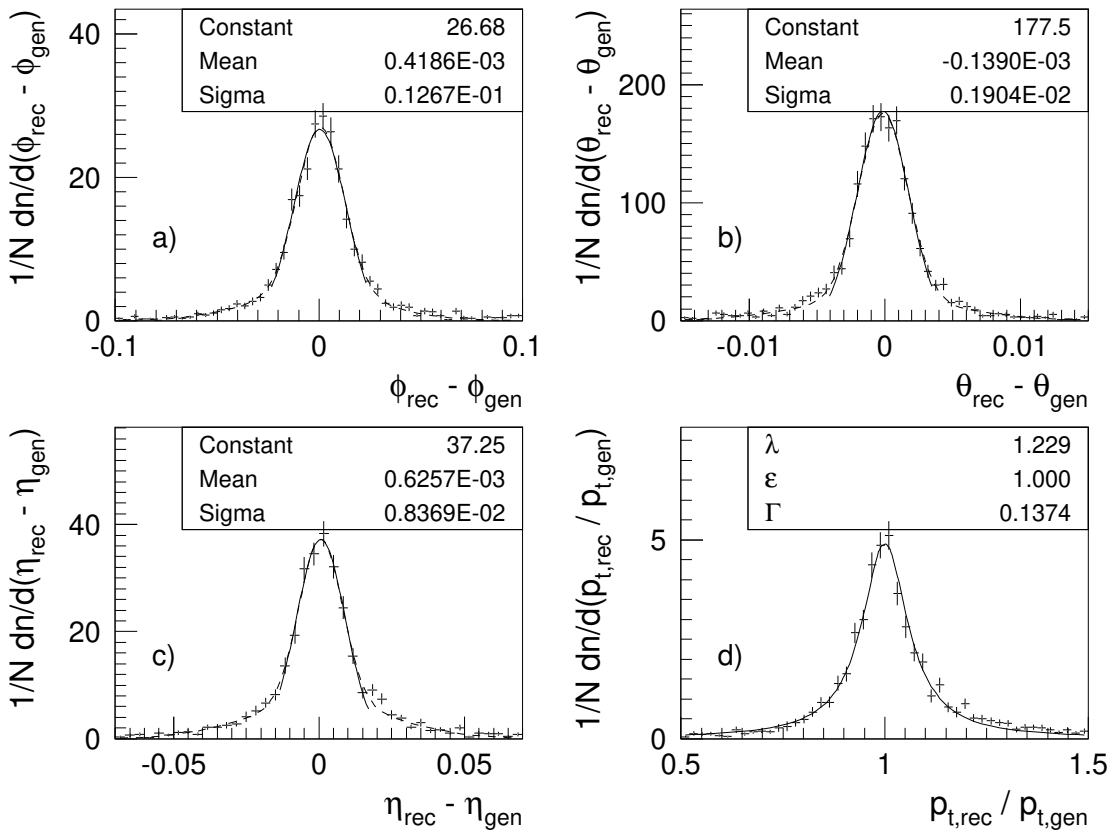

Figure 5.12: Angular and transverse momentum resolution for π° after all selection cuts. Angular resolutions (a),(b) and (c) are best described by a double Gaussian form (dashed lines), where the central part is dominated by a single Gaussian (solid lines) which is also used to define the resolutions. The transverse momentum resolution (d) is best fitted by a Breit-Wigner shape $P(x) = \lambda \cdot \Gamma \,/\, ((\epsilon - x)^2 + (\Gamma/2)^2)$. The resolution is here defined to be $\Gamma/2$ of the distribution.

described in Section 5.3. One can then define ϵ_{π° and κ_{π° as

$$\epsilon_{\pi^\circ} = \frac{N_{\pi^\circ}(gen \wedge rec_{md})}{N_{\pi^\circ}(gen)}\,, \qquad \kappa_{\pi^\circ} = \frac{N_{\pi^\circ}(rec \wedge gen_{md})}{N_{\pi^\circ}(rec)}\,, \tag{5.6}$$

where *gen* and *rec* denote generated and reconstructed objects respectively, and the subscript *md* expresses the condition of spatial correlation described above. The values obtained in this way are very similar for both CDM(w) and MEPS(w) at $\epsilon_{\pi^\circ} > 45$ % and $\kappa_{\pi^\circ} > 68$ %.

As described in Section 5.3, these numbers are mainly affected by the density of particles surrounding a particular π° candidate. The loss in efficiency is connected to the rather large hybrid class of clusters, which are rejected in the selection procedure because their cluster shapes have been distorted by the addition of background

energy. The deviation of κ_{π^0} from 100 % is caused by reconstructed objects which are accepted as π^0 candidates but are not connected to a π^0-meson originating from the primary event vertex. Some of these are the remaining hadronic clusters which pass the selection. Others are π^0-mesons with a somewhat smaller energy or transverse momentum than required in the selection, which might be boosted into the accepted phase space region by small additions of hadronic energy which do not distort the shape estimators enough for them to be rejected. The following should however be noted about the background:

- The main hadronic background is composed of charged pions. Charged pions should show the same characteristics as their uncharged sibling. Background of this type therefore does not affect the main features of the signal events.
- Background from secondary interactions in the material of the detector is predicted by the simulation to be not larger than a few percent and therefore has no significant influence.

It should also be noted that the numbers quoted in this section serve as an indicator for the quality of the selection procedure only and are not used to determine the actual detector corrections (see Section 6.3).

The cluster candidates for which a relationship can be established with a generated π^0-meson as described above can be used to determine the angular and transverse momentum resolution of the given selection. Figure 5.12 shows the resolution plots. The angular resolutions are fitted well by a double Gaussian form, where the second Gaussian serves to describe the tails of the distribution (e.g. caused by showering in passive material worsening the angular information). Numerical values for the resolutions are defined to be the Sigma of a Gaussian describing the central part of the distributions. One obtains ≈ 13 mrad for the azimuthal and ≈ 2 mrad for the polar angle. The $p_{T,\pi}$ resolution is best fitted by a Breit-Wigner shape and the resolution for this variable is defined to be half the width of the distribution $\Gamma/2 \approx 7$ %.

Chapter 6

Measurement of Neutral Pion Production Cross Sections

The cross section σ_t relates the number of events N_t of a certain type t to the available integrated luminosity $\mathcal{L}$

$$N_t = \sigma_t \cdot \mathcal{L}\,. \tag{6.1}$$

The amount of integrated luminosity $\mathcal{L}$ represents the data volume taken by the experiment which is available for analysis (see Section 3.3). The physics responsible for the value of N_t is described by σ_t in the formula above. The experimentalist therefore measures σ_t by counting the number of events of type t

$$\sigma_t = \frac{N_t}{\mathcal{L}}\,. \tag{6.2}$$

In reality the situation is somewhat more complicated. Several corrections have to be applied to the number of events N_t measured

$$\sigma_t = \frac{N_t}{\mathcal{L}} \cdot \epsilon_{tr} \cdot C_{pur/eff} \cdot C_{rad}. \tag{6.3}$$

- ϵ_{tr} compensates for inefficiencies of the trigger system.
- $C_{pur/eff}$ considers inefficiencies and impurities when selecting events of type t.
- C_{rad} compensates for the influence of QED radiation.

The motivation of the last correction C_{rad} is different from the others. The measurement is perfectly valid without applying C_{rad} if one states that the results include effects of QED radiation. However, C_{rad} is applied to be able to compare the measurement to theoretical predictions which usually do not include QED radiative effects. Apart from the value of σ_t, a lot can be learned from the dependence of σ_t

on various quantities $a, b, ...$ relevant to the process under study. If experimentally feasible one therefore measures differential cross sections such as $d\sigma_T/da$, $d\sigma_T/db$, $d\sigma_T/(da\,db)$,...instead of just the total cross section in the considered phase space.

The following chapter describes the measurement of differential π°-meson production cross sections. The measurement is based on the selection of π°-mesons (described in Chapter 5) in deep-inelastic scattering events (selected in Chapter 4). First the observables are defined. Events entering the analysis are triggered by the subtrigger s002. For each observable the efficiency of trigger s002 is determined and the resulting correction is applied to the data. The data is then corrected for detector effects and the influence of QED radiation using a bin-by-bin unfolding procedure. Finally possible sources of systematic uncertainties are studied to estimate their effect on the observables. The chapter concludes with the presentation of the final experimental results of this analysis: The differential π°-meson production cross sections including the statistical and systematic errors for each observable.

6.1 The Observables

The π° cross sections are measured as a function of Q^2 and as a function of x, $p_{T,\pi}$ and η_π in three regions of Q^2 ($2.0 < Q_1^2 < 4.5 < Q_2^2 < 15.0 < Q_3^2 < 70.0$ GeV^2) each. The restraints $5^\circ < \theta_\pi < 25^\circ$, $x_\pi = E_\pi / E_{proton} > 0.01$ and $p_{T,\pi} > 2.5$ GeV as listed in Table 5.1 are applied. Perturbative calculations become more reliable for higher values of the scale relevant to the process under study. For high p_T π°-meson production at low Q^2 the transverse momentum of the π°-mesons can be considered the suitable scale for calculations. Cross sections as a function of x and Q^2 are therefore also measured for the higher threshold of $p_{T,\pi} > 3.5$ GeV. Table 6.1 shows an overview of all distributions measured. The ~1700 (~600 for $p_{T,\pi} > 3.5$ GeV) π°

Observable	DIS phase space		π° phase space
$d\sigma_\pi/dx$	$0.1 < y < 0.6$	$2.0 < Q^2 < 4.5$ GeV^2	$5^\circ < \theta_\pi < 25^\circ$ (lab)
$d\sigma_\pi/dp_{T,\pi}$	and three bins	$4.5 < Q^2 < 15.0$ GeV^2	$x_\pi > 0.01$ (lab)
$d\sigma_\pi/d\eta_\pi$	of Q^2 each:	$15.0 < Q^2 < 70.0$ GeV^2	$p_{T,\pi} > 2.5$ GeV
$d\sigma_\pi/dQ^2$			(hcms)
$d\sigma_\pi/dQ^2$	$0.1 < y < 0.6$	$2.0 < Q^2 < 70.0$ GeV^2	higher $p_{T,\pi}$ threshold
$d\sigma_\pi/dx$			$p_{T,\pi} > 3.5$ GeV

Table 6.1: Summary of quantities measured including the phase space in which they are defined.

candidates available after the selection are distributed such that every bin contains roughly the same number of entries. The additional requirement of no less than about 100 entries per bin then determines the maximum number of bins for each distribution.

6.2 Trigger Efficiency for Events containing a π° Candidate

The measurement of cross sections requires well defined and stable conditions for the trigger which decides whether an event as seen by the detector is kept for further analysis. Corrections must be determined for events rejected by the trigger which would otherwise contribute to the cross sections. In this section the trigger efficiencies are determined for all observables. The data is then corrected bin-by-bin for any inefficiency. It is important to note that this correction is applied before the unfolding procedure described in the next section. Trigger inefficiencies are consequently not considered in the unfolding.

The Level 1 (L1, see Section 3.4) trigger employed in this analysis is s002. Essentially it is sensitive to energy depositions in the backward calorimeter SPACAL, validated by a sufficiently well reconstructed primary event vertex and the requirement of some activity in the central region of the detector in the form of tracks.

The s002 subtrigger was chosen because it covers the entire backward calorimeter, including the central trigger card around the beampipe. The latter corresponds to the region most affected by the 'hot spot' (see Section 4.1). The SPACAL IET trigger is described in Section 3.4. For s002 the second highest trigger threshold is used for both the central and the outer part of the SPACAL (SPCLe_IET >1 .or. SPCLe_IET_Cen_2), which starts to become effective at energy depositions of about 5 GeV. The phase space considered in the analysis requires positron energies of above 10 GeV. This part of the trigger should therefore yield an efficiency very close to 100 %. Originally intended to be based on the SPACAL alone, the high rate of background events caused by the 'hot spot' requires additional conditions to complement the SPACAL information.

The existence of a well defined primary event vertex is ascertained by the trigger element zVtx_sig. It is formed by filling the z coordinate resulting from combinations of hits in the central and forward proportional chambers (see Section 3.1.1) into a histogram. If the hits are caused by tracks emerging from a common vertex, a significant peak should be visible at the z position of the vertex, and zVtx_sig is fired.

Information from the central jet chambers described in Section 3.1.1 is used to tag every event according to the activity present in the central part of the detector. Since a complete track finding algorithm would take more time than available for

the L1 trigger decision, hit masks are defined according to track positions in drift space and track curvature in the magnetic field. Tracks with low or high momentum can be distinguished as well as the charge of tracks with a momentum lower than about 1 GeV. One of the masks needs to be fired for the trigger element DCRPh_Ta to be switched on. During the run period this condition in s002 was replaced by DCRPh_THig, which requires the fired mask to be for tracks with a transverse momentum of more than 800 MeV.

A set of veto conditions (see Section 3.3) complements the trigger requirements listed above to further reduce the contamination by background events. Except for SPCLh_AToF_E_1, which was added from run 166213, these conditions did not change over the run period. The main trigger elements of s002 and their logical connection are listed in Table 6.2. Also indicated is the run range during which the respective condition was enabled.

An important feature needed for a reliable measurement of cross sections is the stability of the trigger. The ratio of the number of events kept by the trigger to the corresponding luminosity, from which the cross section is obtained, should be constant over the entire data taking period. Figure 6.1 shows the ratio of number of events to corresponding luminosity as a function of the luminosity acquired (a) and the sum of events as a function of the luminosity acquired (b). The trigger shows stable behavior, which is not influenced by the change in the track based conditions indicated by the dashed line. Furthermore the introduction of the anti-time-of-flight veto from the hadronic part of the SPACAL (SPCLh_AToF_E_1, marked by the dotted line), causes no significant effect. The selection includes the conditions listed in Table 6.1, but instead of applying the shower shape selection described in

SPACAL based trigger elements	
SPCLe_IET>1 .OR. SPCLe_IET_Cen_2	
.AND.	
.NOT. SPCLh_AToF_E_1	added from run 166213

.AND.

track based trigger elements	
DCRPh_Ta .AND. zVtx_sig	before run 163255
DCRPh_THig .AND. zVtx_sig	from run 163255

Table 6.2: Setup of trigger s002 *for the run period in 1996 relevant to this analysis. The trigger setup was modified twice during the data taking. These changes, however, had no significant effect on the stability of the trigger.*

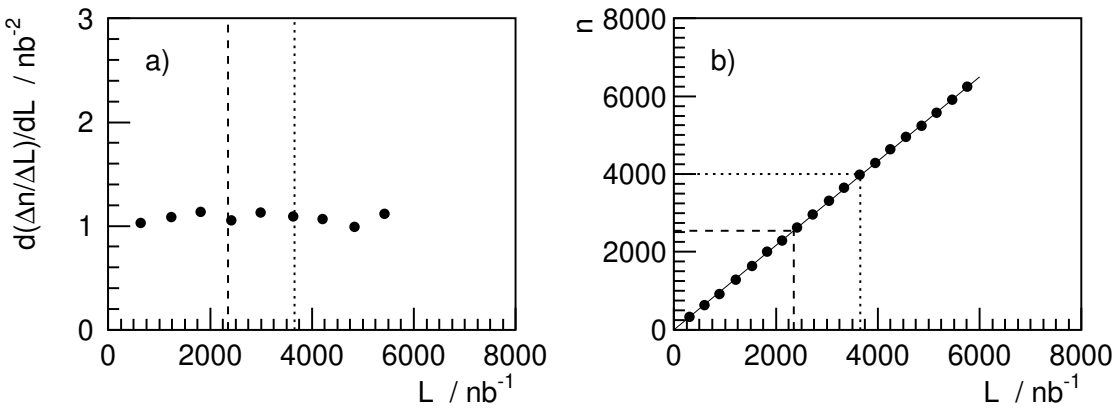

Figure 6.1: Stability of trigger s002. *L is the luminosity and n the corresponding number of events. The dashed line indicates the change in the track based trigger elements of* s002. *The dotted line represents the introduction of the* SPACAL *hadronic anti-time-of-flight veto (see Table 6.2).*

Section 5.3, the candidate is only required to have $\Omega_{\rm em} > 0.8$. This reduced selection ensures that only events with relevant topologies enter while still providing sufficient statistics.

Because conditions based on the primary event vertex and on tracks in the central detector are included in the trigger, the efficiency of triggering events in the analysis phase space depends not only on the scattered positron, but is also influenced by the configuration of the hadronic final state. In particular the trigger is not fully efficient, since the focus on the forward region of the detector allows events into the analysis without sufficient activity in the central region to fire the track trigger elements. The trigger efficiency ϵ_{s2} for every measured distribution must therefore be determined. ϵ_{s2} is calculated from data only to avoid additional uncertainties from the trigger simulation. A monitor trigger is used to define a data sample independent of the requirements applied in s002. Events in this subsample of the data which survive all the selection requirements of the analysis chain but did not fire s002 constitute the inefficiency of this trigger for this analysis.

Unfortunately there is no single monitor trigger with a sufficiently high rate independent of all the conditions in s002. The efficiencies therefore have to be determined in two separate steps. First the performance of the trigger elements relying on information from the backward calorimeter is studied using events kept by SPMON, a condition formed by requiring one or more of the following four subtriggers: s060, s067, s075, and/or s077. These subtriggers are mainly based on energy depositions in the LAr calorimeter. The conditions in s002 concerning the primary vertex and central tracks are closely related. Their influence is therefore determined in a single step, with s000 used as monitor trigger. s000 is based solely

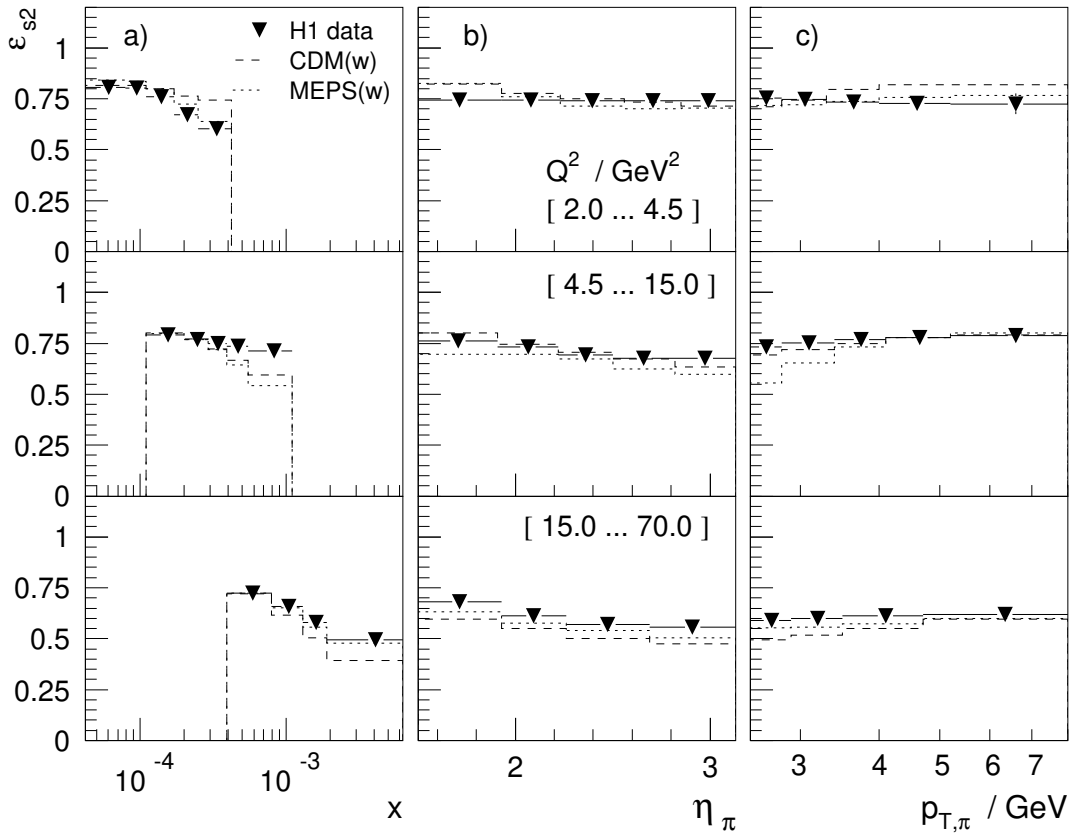

Figure 6.2: Efficiency of trigger s002 *for $d\sigma_\pi/dx$ (a), $d\sigma_\pi/d\eta_\pi$ (b), and $d\sigma_\pi/dp_{T,\pi}$ (c) for the three regions in Q^2 listed in Table 6.1 ($p_{T,\pi} > 2.5$ GeV). The efficiencies are determined from data only. The behavior of the simulated event samples is shown for comparison.*

on SPACAL information. The efficiency of s002 in bin i for any of the distributions observed can now be determined as

$$\epsilon_{s2,i} = \left(\frac{N_{Sp,i}}{N_i}\right) \cdot \left(\frac{M_{Tr,i}}{M_i}\right). \tag{6.4}$$

N_i denotes the number of events provided by s000 which pass the selection for bin i. The same selection as for the stability study above is used. It should be noted again that the main sources of background (i.e. charged pions) behave according to the same underlying mechanism and therefore do not distort ϵ_{s2} as seen for events containing a π°-meson. $N_{Sp,i}$ is the subsample of N_i for which the SPACAL based trigger elements in s002 are fired. M_i is defined analog to N_i, but with the events provided by SPMON instead of s000. $M_{Tr,i}$ denotes the subsample of M_i for which the track based trigger elements in s002 are fired (see Table 6.2).

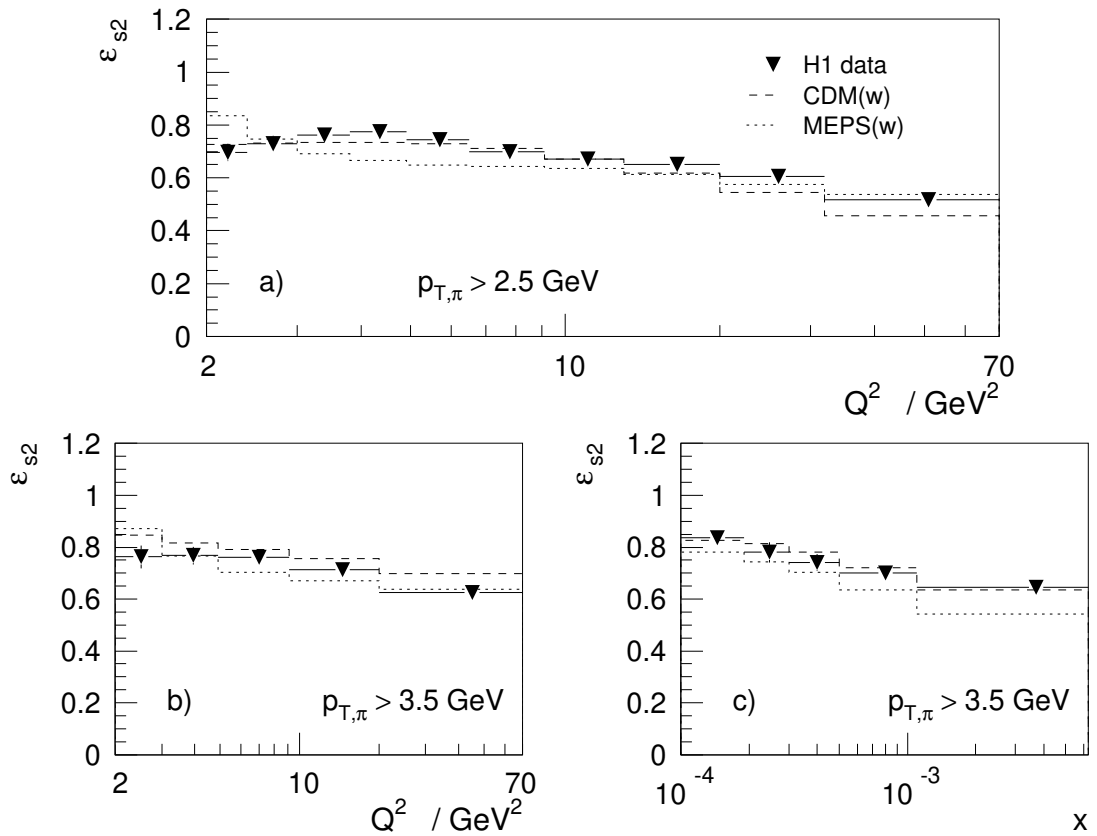

Figure 6.3: Efficiency of trigger s002 *for $d\sigma_\pi/dQ^2$ ($p_{T,\pi} > 2.5$ GeV) (a), and for the higher threshold of $p_{T,\pi} > 3.5$ GeV for the observables $d\sigma_\pi/dQ^2$ (b) and $d\sigma_\pi/dx$ (c) as listed in Table 6.1. The efficiencies are determined from data only. The behavior of the simulated event samples is shown for comparison.*

The trigger efficiencies determined in this way for all distributions measured are shown in Figures 6.2 and 6.3. Efficiencies in the range of 60 to 80 % are obtained. A general tendency can be observed for ϵ_{s2} to decrease towards larger x. This can be understood in terms of the event kinematical properties, since the hadronic final state in this region tends to go more forward (e.g. small polar angles), making it less likely to fulfill the track based conditions of s002 which mainly rely on the central track detectors. Since the test for the success or failure of the trigger in each event is by nature a Bernoulli process, the error to be propagated for the efficiencies is given by the standard deviation of a binomial distribution.

For about 5 % of the 5.8 pb^{-1} included in this analysis, trigger s002 was operated with a prescale factor $p \neq 1$. In these runs the trigger fires only after p events have fulfilled its condition. The factor is nearly always $p = 2$ for these 5 % of the luminosity. Since s002 is the only trigger used, the prescales are compensated for

by simply applying the factor p as a weight to all events in these runs.

There is no Level 2 or Level 3 trigger requirement attached to s002 for the chosen run period. The influence of the Level 4 filter farm and the Level 5 event classification are checked using the respective reject tapes for each level. These tapes contain a certain percentage of the events rejected by L4 and L5 (see Section 3.4). For the present analysis they contain no event able to survive the selection chain.

6.3 The Unfolding Procedure

The unfolding of the data for the effects of finite detector resolution and acceptance and for the influence of QED radiation is described in this section. Note that all inefficiencies of the trigger system are already corrected for at this stage (see previous section). Bin-by-bin correction constants are employed for the unfolding procedure. The following strategy is used:

(1) A sample of generated events (including effects of QED radiation) is subjected to the full H1 detector simulation and reconstruction. The observables are obtained on the level of reconstructed objects (see Chapter 5) and on the level of generated hadrons. The level of generated hadrons is defined such that the effects of QED radiation as seen by the detector resolution and acceptance are roughly emulated (see below).

(2) Comparing the two levels in (1) reveals the influence of the detector on the observables.

(3) Two more sets of Monte Carlo events are generated: One set without the effects of QED radiation, and another set including QED radiation. For the latter the level of generated hadrons is defined as in (1). The set without QED radiation obviously does not need such a definition.

(4) Comparing the two levels in (3) reveals the influence of QED radiation on the observables.

(5) With the information of (2) and (4) the data is unfolded for detector effects and for the influence of QED radiation.

In principle the correction factors could be determined by directly comparing the observables obtained on the level of reconstructed objects in (1) and on the level of generated hadrons (without QED radiation) in (3). Introducing the intermediate level (generated hadrons including QED radiation) however has some technical advantages. Subjecting generated events to a full H1 simulation and reconstruction procedure as needed for the sample in (1) is by far the most time-consuming step

in calculating the correction factors. Depending on the CPU used, up to 30 seconds are needed for a single event. The available statistics for this sample therefore must not be arbitrarily large. By using events from the same sample for the comparison in (2), remaining statistical fluctuations are canceled out to a certain extent. There is no need for simulated and reconstructed objects for the comparison in (4). Much larger event samples can therefore be made available in (3) until statistical fluctuations become insignificant.

To determine the correction constants according to the strategy outlined above, four samples from a Monte Carlo event generator are needed to calculate the following cross sections for each bin i:

(I) $(\sigma^{rec}_{\pi,rad,i})$: obtained on the level of reconstructed objects using a sample of events generated including the effects of QED radiation and subjected to a full H1 detector simulation and reconstruction.

(II) $(\sigma^{gen}_{\pi,rad,i})$: calculated from the same sample of events as used in (I), but on the level of generated hadrons including QED radiation; final state photons are merged with the scattered positron if closer than five degrees; events with an initial state photon of more then 3 GeV energy and polar angle larger than 178° are rejected to emulate the situation in the detector.

(III) $(\sigma^{gen}_{\pi,rad,i})$: defined identical to (II), but calculated from a different sample with much higher statistics.

(IV) $(\sigma^{gen}_{\pi,i})$ obtained from a sample generated without the effects of QED radiation but otherwise identical to (III) on the level of generated hadrons (also with very high statistics).

The correction factor $C_{b,i}$ for bin i in any of the measured distributions is then calculated from these four samples as

$$C_{b,i} \;=\; \left(\frac{\sigma^{gen}_{\pi,rad,i}}{\sigma^{rec}_{\pi,rad,i}}\right) \;\cdot\; \left(\frac{\sigma^{gen}_{\pi,i}}{\sigma^{gen}_{\pi,rad,i}}\right) \tag{6.5}$$

The intermediate level $(\sigma^{gen}_{\pi,rad,i})$ emulates the situation in the detector after the selection has been applied. Due to the finite resolution of the backward calorimeter, the scattered positron and a final state photon will be returned as one reconstructed cluster if both are reasonably close together [36]. Hence the merging of positron and photon for $(\sigma^{gen}_{\pi,rad,i})$ if their relative angle is less than five degrees. Events with a very energetic initial state photon on the other hand might be rejected during the event selection by, for example, the cut on $\sum (E - p_z)$ as described in Section 4.3. Hence events with an energetic initial state photon are rejected for $(\sigma^{gen}_{\pi,rad,i})$. Note that the definition of $(\sigma^{gen}_{\pi,rad,i})$ is rather arbitrary, but cancels in (6.5). The corrected

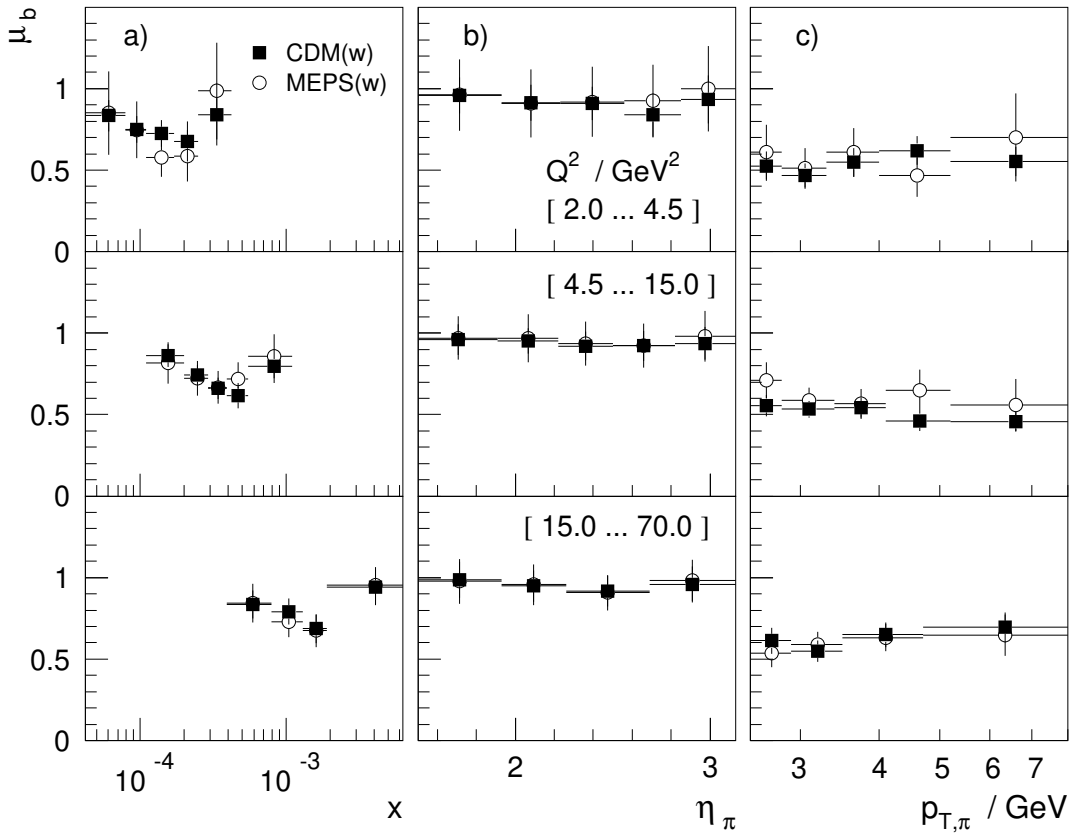

Figure 6.4: Bin migrations for $d\sigma_\pi/dx$ (a), $d\sigma_\pi/d\eta_\pi$ (b), and $d\sigma_\pi/dp_{T,\pi}$ (c) for the three regions in Q^2 listed in Table 6.1 ($p_{T,\pi} > 2.5$ GeV). μ_b is determined using the levels of stable hadrons and simulated and reconstructed objects of CDM(w) and MEPS(w).

cross section in each bin can now be determined by

$$\sigma_{\pi,i} \;=\; C_{b,i} \;\cdot\; \sigma_{\pi,i}^{raw} \tag{6.6}$$

where $\sigma_{\pi,i}^{raw}$ is the cross section as measured experimentally and $\sigma_{\pi,i}$ is the unfolded experimental value.

The bin-by-bin correction procedure can be used when it is a good approximation to unfolding with a matrix $\mathcal{M}$: $\vec{u} = \mathcal{M} \cdot \vec{m}$, where the vector $\vec{m}$ represents the experimental data and the vector $\vec{u}$ is the unfolded distribution related to $\vec{m}$ by $\mathcal{M}$. The finite resolution of the detector implies that an element in a certain bin in $\vec{m}$ might migrate to a different bin in $\vec{u}$. The bin-by-bin correction is an adequate alternative to the matrix method if the bin-to-bin migrations are reasonably small and therefore the matrix $\mathcal{M}$ is approximately diagonal. To study the size of the

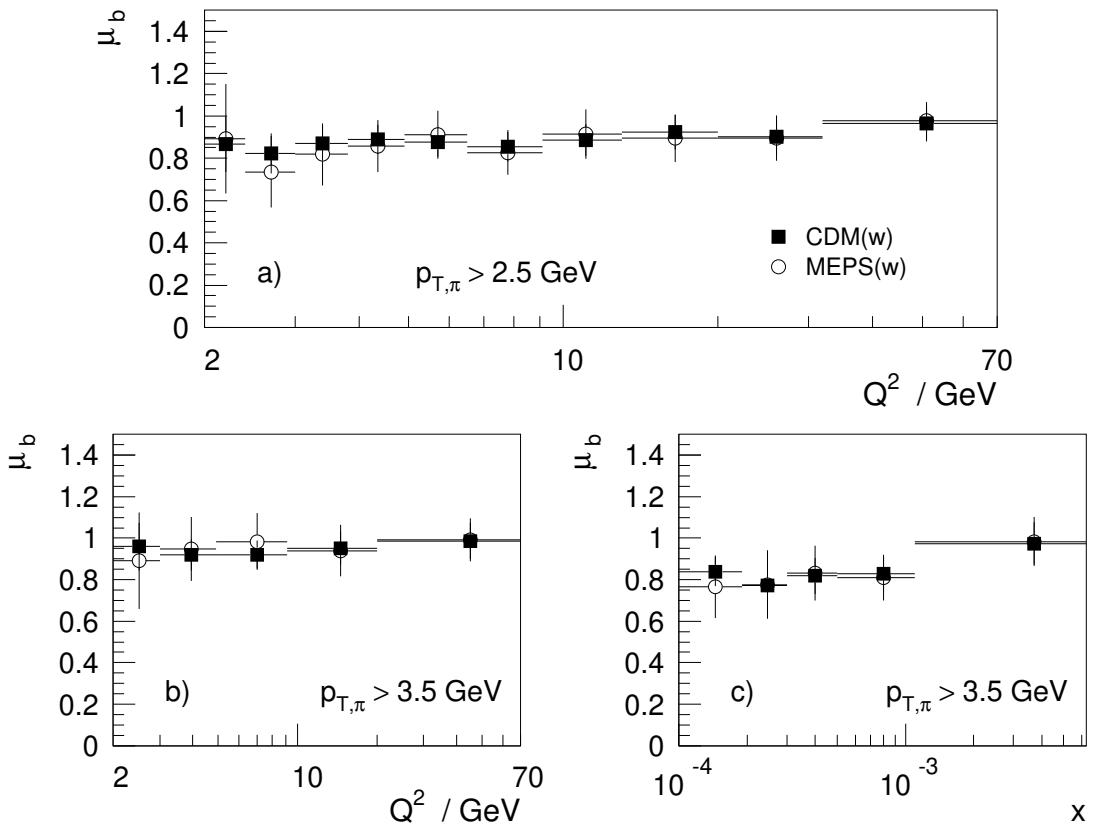

Figure 6.5: Bin migrations for $d\sigma_\pi/dQ^2$ ($p_{T,\pi} > 2.5$ GeV) (a), and for the higher threshold of $p_{T,\pi} > 3.5$ GeV for the observables $d\sigma_\pi/dQ^2$ (b) and $d\sigma_\pi/dx$ (c) as listed in Table 6.1. μ_b is determined using the levels of stable hadrons and simulated and reconstructed objects of CDM(w) and MEPS(w).

migrations they are quantified as

$$\mu_{b,i} = \left(\frac{K_{gen+rec}}{K_{rec}}\right), \tag{6.7}$$

where K_{rec} is the number of entries in bin i found among the simulated and reconstructed objects after the π° selection, and $K_{gen+rec}$ denotes the corresponding subsample of those entries which stem from the same bin on the level of generated hadrons. Events are included in which a suitable candidate is identified on both levels. The value of μ_b is then required to be above 0.5 for any bin included in the measurement. The result for all observables can be seen in Figures 6.4 and 6.5 for both CDM(w) and MEPS(w). It should be noted that μ_b for any particular variable is a function of the achieved resolution and (since migrations mostly affect entries in the vicinity of the bin boundaries) the bin width. It can thus be understood why μ_b

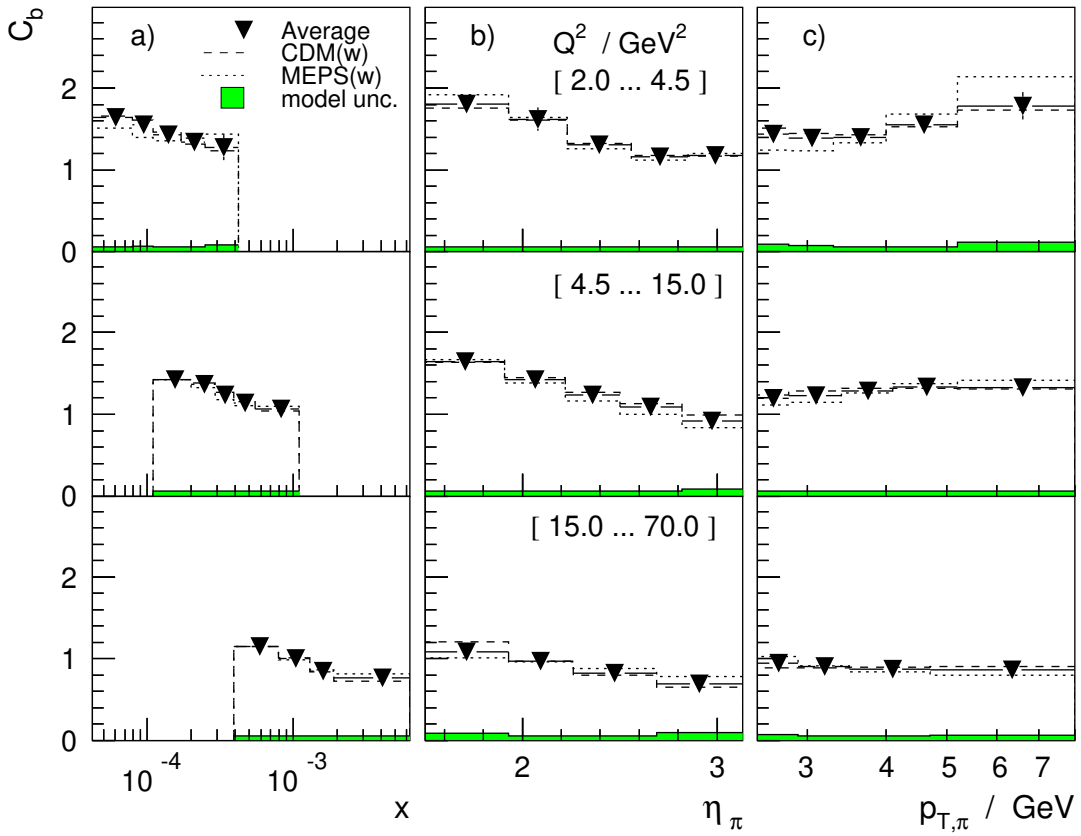

Figure 6.6: Correction functions for $d\sigma_\pi/dx$ (a), $d\sigma_\pi/d\eta_\pi$ (b), and $d\sigma_\pi/dp_{T,\pi}$ (c) for the three regions in Q^2 listed in Table 6.1 ($p_{T,\pi} > 2.5$ GeV). C_b is determined using the levels of stable hadrons and simulated and reconstructed objects of CDM(w) and MEPS(w) respectively. Their average is calculated according to (6.8). The shaded histogram represents the error arising from the remaining difference of the two models.

for $d\sigma_\pi/d\eta_\pi$ is significantly higher than for $d\sigma_\pi/dp_{T,\pi}$, since the ratio of resolution to bin width is smaller for η_π than for $p_{T,\pi}$ (see Section 5.5).

Because in reality the bins are not completely independent of each other, the quality of the correction procedure described above depends on how well the samples of simulated events are able to reproduce the migrations for the relevant variables. Hence the emphasis put on the modeling of the detector response in Section 5.4. Remaining deficiencies in describing the behavior of the data might lead to systematic effects which are specific to the model used to determine the correction factors. It is therefore important to use two different models for the determination of the correction factors to obtain a measure of the systematic uncertainty introduced at this step. CDM(w) and MEPS(w) are used for this purpose in this analysis.

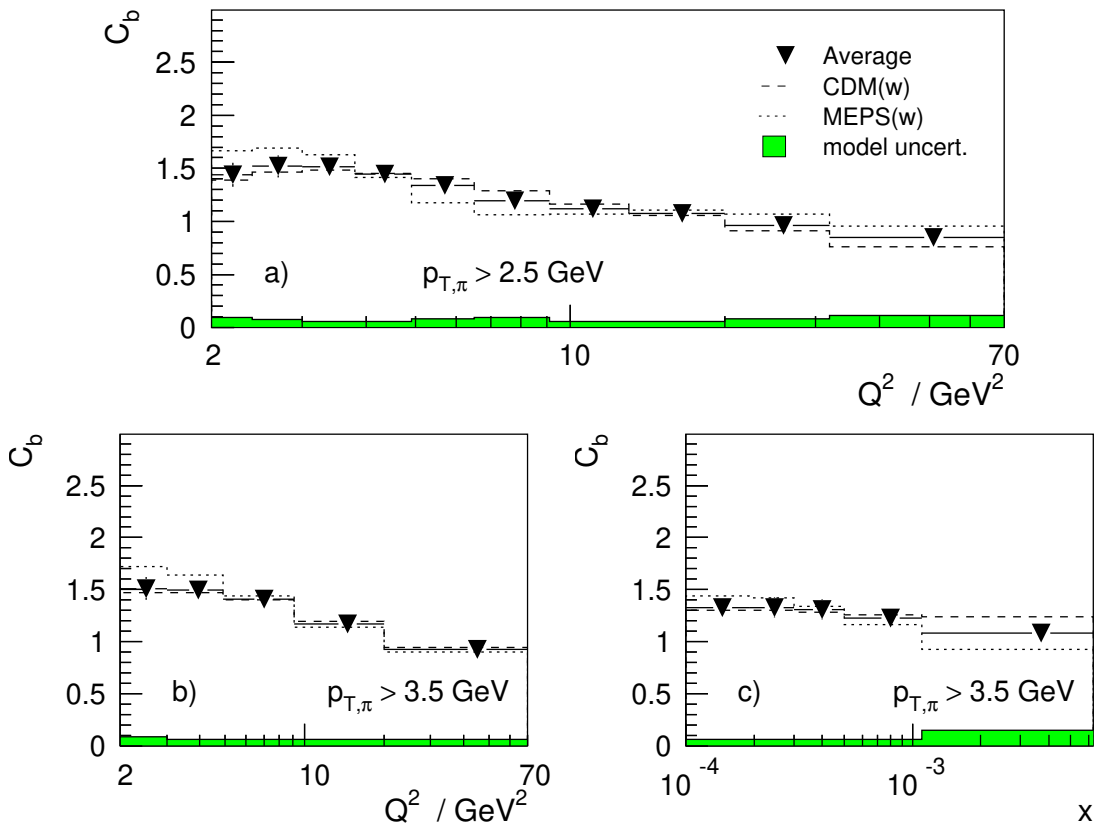

Figure 6.7: Correction functions for $d\sigma_\pi/dQ^2$ ($p_{T,\pi} > 2.5$ GeV) (a), and for the higher threshold of $p_{T,\pi} > 3.5$ GeV for the observables $d\sigma_\pi/dQ^2$ (b) and $d\sigma_\pi/dx$ (c) as listed in Table 6.1. C_b is determined using the levels of stable hadrons and simulated and reconstructed objects of CDM(w) and MEPS(w) respectively. Their average is calculated according to (6.8). The shaded histogram represents the error arising from the remaining difference of the two models.

A total of about 100 M Monte Carlo events were generated for this analysis, representing an integrated luminosity of more than $\mathcal{L} = 160$ pb^{-1}. Samples representing $\mathcal{L} = 12.4$ pb^{-1} (CDM(w)) and $\mathcal{L} = 18.3$ pb^{-1} (MEPS(w)) are subjected to a full H1 detector simulation and reconstruction to calculate ($\sigma^{rec}_{\pi,rad,i}$). To save CPU time the samples are preselected for events likely to survive the selection procedure. A probability in the range [0...1] is calculated for every event depending on its kinematical properties and the amount of energy carried by particles in the forward direction. The higher the probability, the more likely the event is to survive the event selection. The probability obtained is then compared to a random number in the same range and the event is only kept if the probability turns out to be larger than the random number. If the event is kept, the inverse of the probability is assigned to the event as weighting factor. The maximum weight is limited to be less

than 20. If the weighting procedure is adequate, it keeps nearly all the events with a suitable π° candidate. These events should have small weights or no weights at all (i.e. the weighting factor equals one). For more than 85 % of the events in the final π° selection the weight is indeed one, with less than 1 % featuring a weighting factor larger than five. Using this weighting procedure one can control the distributions outside the selected phase space without having to process large numbers of events irrelevant to the measured observables. For both Monte Carlo samples combined 1.8 M events were finally simulated and reconstructed out of 27 M events originally generated. The remaining 73 M events constitute samples (III) and (IV).

The correction is carried out independently for both models resulting in two correction factors for every bin. The final correction constants are obtained by calculating an inverse error squared weighted average [3] and error according to

$$\bar{C}_b \pm \delta\bar{C}_b = \frac{\sum_i w_i C_{b,i}}{\sum_i w_i} \pm \left(\sum_i w_i\right)^{-1/2} \qquad \text{with} \qquad w_i = \frac{1}{(\delta C_{b,i})^2} , \tag{6.8}$$

where the sum extends over the Monte Carlo samples used, in this case CDM(w) and MEPS(w). It was argued in Section 5.4 that comparing the influence of choosing either CDM(w) or MEPS(w) can be used to estimate the model dependence of the final results. The systematic uncertainty arising from the difference between the two models is estimated by taking half of the distance between the correction factors in each bin. The two sets of correction factors and the resulting average can be seen in Figures 6.6 and 6.7. The shaded histogram represents the systematic uncertainty as described above.

6.4 Background and Systematic Uncertainties

The measurement of cross sections is of course subject to systematic uncertainties. One of the main tasks of any analysis is to keep the size of these uncertainties to a minimum. Several separate working groups exist to improve the precision of, for example, the absolute energy scale of the calorimeters and the luminosity measurement, which constitute sources of systematic errors for almost any analysis. The remaining influence on the observables of all uncertainties combined is a measure of the quality of the results. The sources of systematic uncertainties considered in this analysis include:

- Precision of the luminosity measurement
- Statistical uncertainty of the trigger efficiency ϵ_{s2}
- Uncertainty of the electromagnetic energy scale of the LAr calorimeter
- Uncertainty of the electromagnetic energy scale of the backward calorimeter

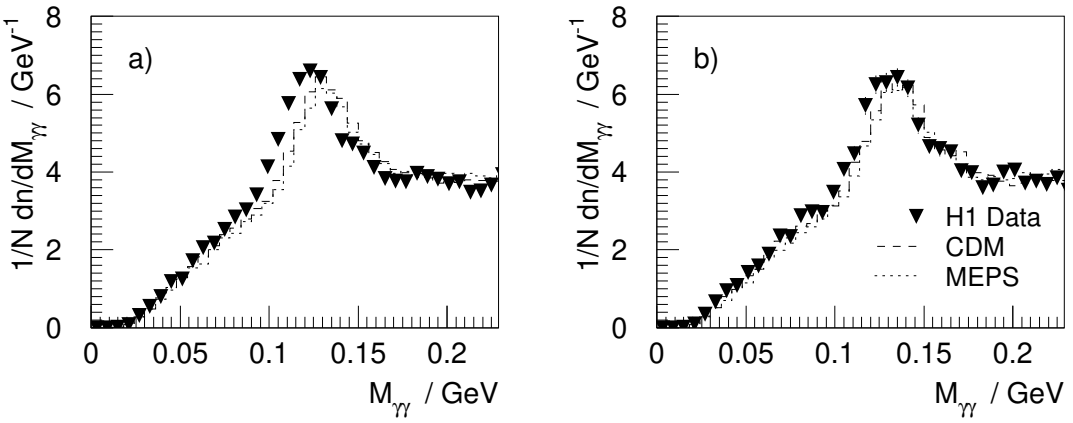

Figure 6.8: Effect of calibration factors on the distribution of the two photon invariant mass: (a) before, (b) after applying the calibration. This recalibration increases the electromagnetic energies measured in the LAr calorimeter by about 5-10 %. The distributions are normalized to the number N of $\gamma\gamma$ candidate combinations entering the distribution.

- Selection of π° candidates
- Acceptance for π° candidates
- Model dependence of the unfolding procedure
- Contributions from photoproduction processes

The following paragraphs describe how the influence of these uncertainties on the observables is estimated. Table 6.3 summarizes typical values of the contributions to the systematic error. They are added in quadrature (for each bin) to obtain the total systematic uncertainty for each observable.

The electromagnetic energy scale of the LAr calorimeter

The energies of the candidate clusters are taken on the electromagnetic scale of the calorimeter after the application of dead material corrections (see Section 3.2.1). Additional calibration factors are applied as obtained from the analysis of the scattered positron [37]. This recalibration increases the electromagnetic energies measured in the LAr calorimeter by about 5-10 %. For the small polar angles considered in this analysis, kinematical constraints however require the scattered positron to have much larger energies than the mean energy of the π° candidates entering the analysis. It is therefore advisable to verify whether or not these calibration factors are applicable here. In order to do so the cuts on energy and transverse momentum of the candidate clusters are lowered to 1 GeV and 0.5 GeV respectively, while keeping

the other requirements listed in Tables 5.1 and 5.2. The opening angle of the two photons from a π° decay is now in most cases large enough for the two photons to be separated by the LAr reconstruction. The distribution of the invariant mass calculated from the combination of any two cluster candidates (here taken to be single photons) in the event should consequently show the characteristic peak at the π° mass. This distribution can be seen in Figure 6.8 (a) before and 6.8 (b) after the application of the calibration factors. As in the study of the scattered positron the prediction of two simulated samples serves as a reference. The data is compatible with this reference after the application of the calibration factors. It can therefore be concluded that the application of the calibration factors provided by the analysis of the scattered positron is applicable and leads to a satisfactory energy calibration.

The absolute scale uncertainty of the LAr calorimeter is hence taken from the positron analysis to be 3 % for the measurement of electromagnetic energies (see Section 3.2.1). To determine the influence of this uncertainty, the energies of the cluster candidates are shifted by ± 3 % before they enter the selection. For each bin the maximum deviation from the central value for the uncorrected cross sections is taken as the systematic error, which is typically less than 5-10 %.

The electromagnetic energy scale of the backward calorimeter

The scattered positron is measured exclusively in the backward calorimeter. Here the absolute energy scale uncertainty is less than 1 %. The energy measurement of the scattered positron enters the measurement via the determination of the event kinematics and is also used to boost the π° transverse momentum into the hadronic cms. As for the LAr calorimeter, the effect on the observables is studied by shifting the measured energies for the scattered positron in the data by ± 1 % before the events enter the selection. This shift is found to cause a systematic uncertainty of less than 5-10 %.

π° selection and acceptance

The influence of π° selection and acceptance requirements on the level of reconstructed objects may also systematically shift the results. The stability of the results with respect to the cuts applied in the selection of π° candidates is studied with the following procedure:

(1) The criteria for the π° selection on the level of reconstructed objects are varied by $\pm\delta_v$ both for the data and the simulated samples. The variation is performed separately for the selection criteria (shower shape cuts) and the π° acceptance (π° phase space). For the latter δ_v is equal to the resolutions determined in Section 5.5. The shower shape cuts are varied by $\delta_v = 5$ %.

(2) The selection criteria on the level of generated hadrons are not changed. They remain as defined in Table 6.1.

(3) New correction functions are determined using the definitions of (1) and (2) (see Section 6.3).

(4) The data as selected in (1) are unfolded using the corresponding correction function determined in (3).

(5) The result is compared to the central value at $\delta_v = 0$. The maximal difference between the central value and the values obtained with $\delta_v \neq 0$ is used as an estimate of the systematic uncertainty for the π° selection and acceptance respectively.

If the unfolding procedure is stable, the change in the uncorrected cross section determined in (1) is compensated for by the change in the correction functions in (3). The systematic uncertainty estimated as described in (5) is typically $5 - 10$ %.

Model dependence of the unfolding procedure

The dependence of the results on the models used for the unfolding procedure is studied in detail in Section 6.3. The unfolding was performed with two models, CDM(w) and MEPS(w), both of which were reweighted for a better modeling of the detector response. The remaining uncertainty for the reweighted sets is estimated

Source of systematic uncertainty	Typical effect on observables
Luminosity measurement:	3 %
Stat. uncertainty of trigger efficiency:	5 %
Uncertainty of LAr el.-mag. scale (3%):	5-10 %
Uncertainty of SPACAL el.-mag. scale (1%, measurement of scat. positron):	5-10 %
Variation of π° selection:	5-10 %
Variation of π° acceptance:	5-10 %
Model dep. of correction functions:	5-10 %
Contribution from photoproduction:	negligible

Table 6.3: Typical contributions to the systematic error. Except for the luminosity measurement, which is a global factor, the uncertainties are determined separately for each bin.

by half the difference between the two models for each bin. The justification for using these two models for this estimate is given in Section 5.4 by demonstrating that the behavior of the data in critical quantities (the transverse shower shape estimators) is in between the behavior visible for the two simulated sets CDM and MEPS. Differences in the shape of the distributions as given by the two models may lead to very small differences in some bins. The corresponding small systematic uncertainty in these cases is considered unrealistic and an average uncertainty as given by the neighboring bins is assigned instead. The uncertainties caused by the model dependence is typically 5-10 %.

Other contributions to the systematic error

Additional uncertainties to be considered are the uncertainty in the determination of the trigger efficiency (less than 5 %, see Section 6.2), and the precision to which the luminosity can be determined (better than 3 %). The influence of remaining events from photoproduction processes, which constitute a type of background in this analysis, is studied using a sample of photoproduction Monte Carlo events (generated with PHOJET [34]) representing an integrated luminosity of about 1 pb^{-1}. After all selection requirements are applied, the contribution from such events to the cross sections measured is found to be negligible.

6.5 Results

By applying the various corrections and assigning the appropriate error as described in the previous sections, the final experimental results of the analysis are obtained as differential cross sections of forward π° production as a function of Q^2, and as a function of x, η_π and $p_{T,\pi}$ in three regions of Q^2 for $p_{T,\pi} > 2.5$ GeV. In addition the π° cross sections as a function of x and Q^2 are measured for a scenario where the lower threshold of the π° transverse momentum is raised to $p_{T,\pi} > 3.5$ GeV. The precise definition of all observables is summarized in Table 6.1.

The measurement extends down to values of $Q^2 > 2$ GeV^2 and $x > 5{\cdot}10^{-5}$, covering two orders of magnitude in x. From 5.8 pb^{-1} of data collected by H1 during the 1996 HERA running period about 1700 π° candidates remain after the selection in this phase space for the lower threshold of $p_{T,\pi} > 2.5$ GeV. These candidates populate the binned distributions such that no less than 100 enter every bin, keeping the statistical uncertainty at a reasonable level. After raising this threshold to $p_{T,\pi} > 3.5$ GeV about 600 candidates are left.

The cross sections as a function of x shown in Figure 6.9 exhibit a strong rise towards small x, as is the case for the total cross section of deep-inelastic ep scattering [8]. The relation of $d\sigma_\pi/dx$ and $d\sigma_\pi/dQ^2$ to the total cross section will be studied in the next chapter. For the region $15.0 < Q^2 < 70.0$ GeV^2 a direct comparison is

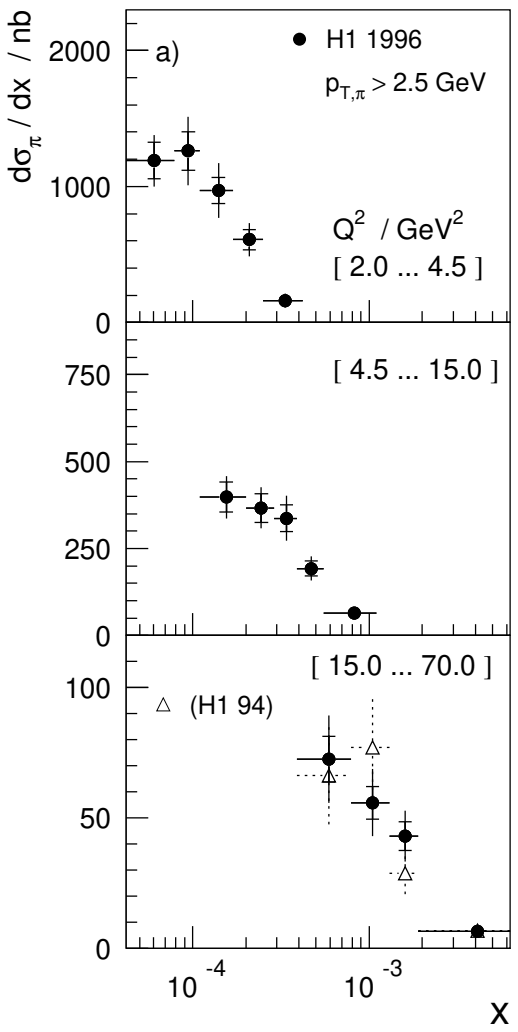

Figure 6.9: Differential π°-meson production cross sections as a function of x in three regions of Q^2 for $p_{T,\pi} > 2.5$ GeV. The inner error represents the statistical uncertainty, the outer error is the quadratic sum of the statistical and the systematic error. The triangles represent the cross sections as determined from the 1994 H1 data. Here only the statistical errors are shown.

possible with results obtained by the author of the present analysis for a previous publication [19] based on data taken during the 1994 running period. The results in [19] are expressed in the form of different observables and exist in a different phase space than for the present analysis. The analysis of the 1994 H1 data was therefore repeated for $d\sigma_\pi/dx$ as defined in Table 6.1 for $15.0 < Q^2 < 70.0$ GeV^2. The results as shown in the lower plot of Figure 6.9 (with statistical errors only) are consistent

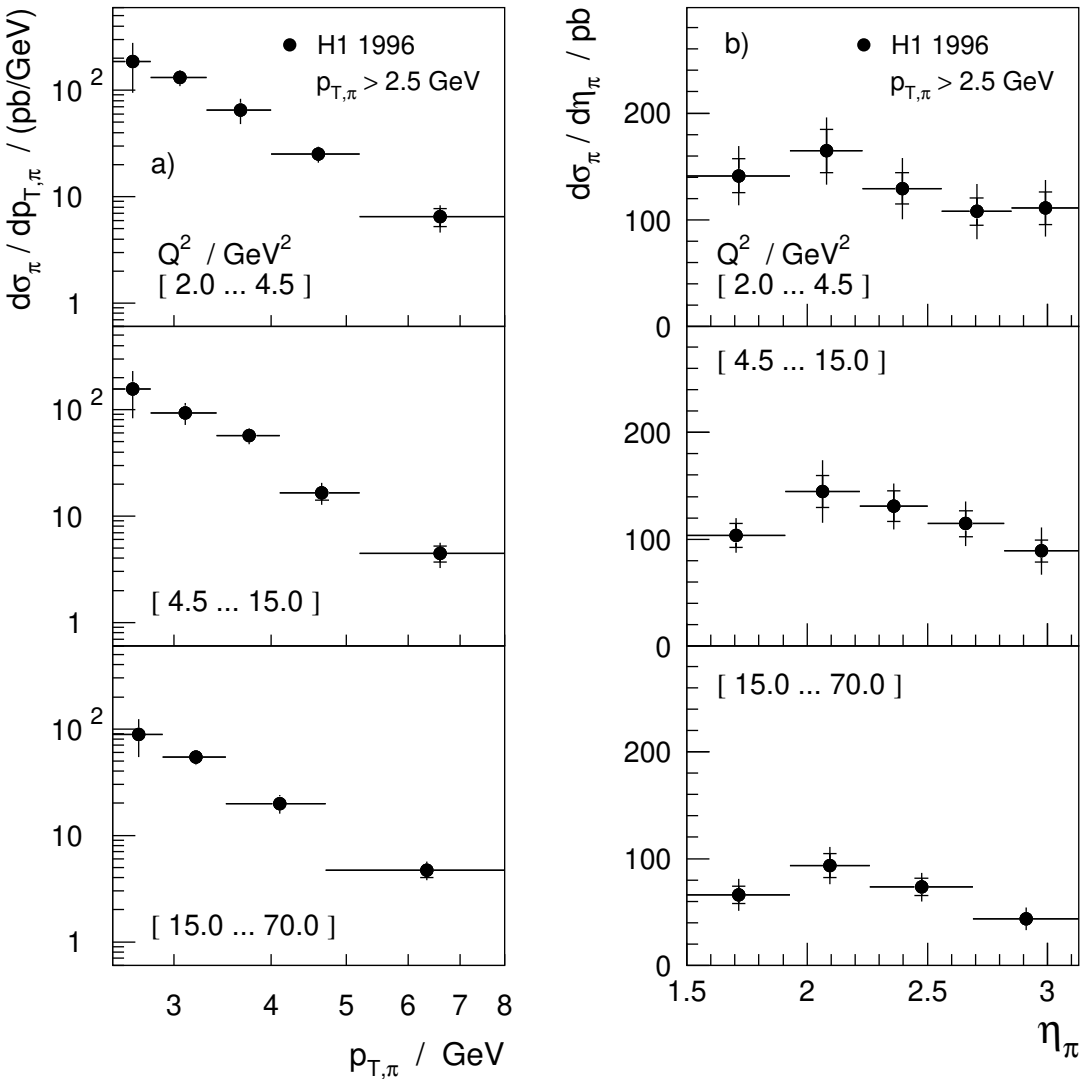

Figure 6.10: Differential π°-meson production cross sections as a function of $p_{T,\pi}$ (a) and η_π (b) in three regions of Q^2 for $p_{T,\pi} > 2.5$ GeV. The inner error represents the statistical uncertainty, the outer error is the quadratic sum of the statistical and the systematic error.

with the cross sections which are the result of the present analysis. Due to the modified experimental apparatus (i.e. the new backward calorimeter SPACAL and the backward drift chamber which were installed in 1995) and the very different trigger conditions in 1994 (no 'hot spot' as in 1996, see Section 4.1) the agreement of the results obtained from the data sets from both years constitutes an important consistency check.

The shapes of $d\sigma_\pi/dp_{T,\pi}$ and $d\sigma_\pi/d\eta_\pi$ (Figure 6.10) show no significant depen-

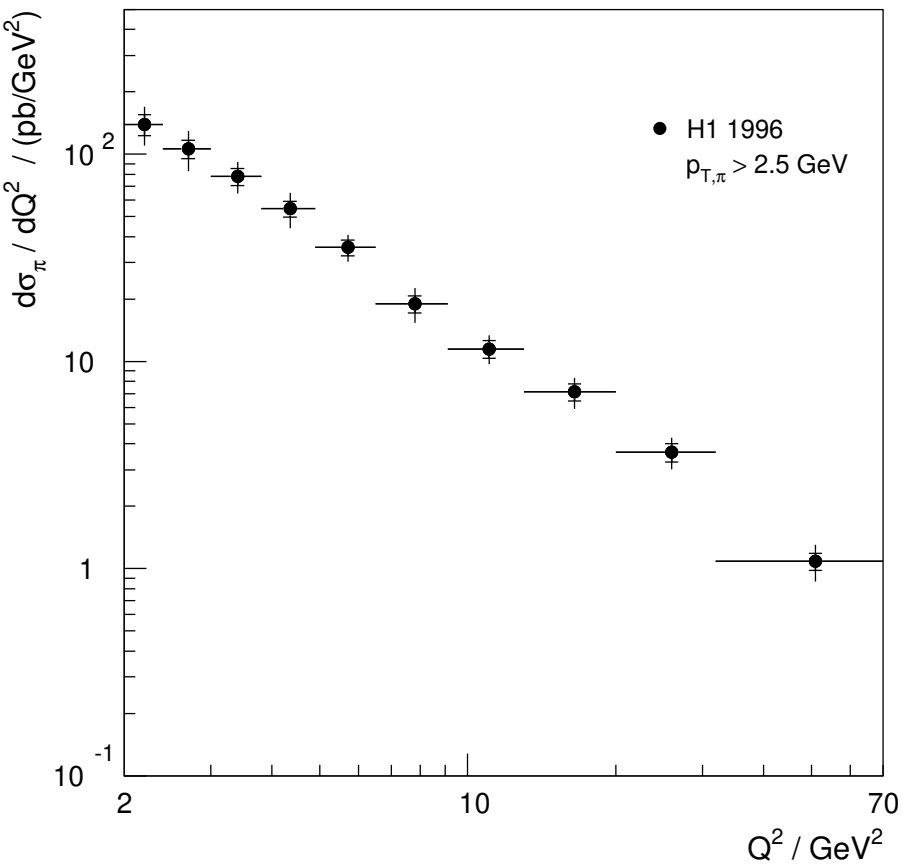

Figure 6.11: Differential π°-meson production cross sections as a function of Q^2. The inner error represents the statistical uncertainty, the outer error is the quadratic sum of the statistical and the systematic error.

dence on the regions of Q^2 in which they are measured. The size of the cross sections decreases towards smaller Q^2 as already visible in Figure 6.9. There is only a weak dependence of the cross sections on η_π. $d\sigma_\pi/dQ^2$ and $d\sigma_\pi/d\eta_\pi$ for the three regions of Q^2 combined both cover the entire phase space selected for this analysis. The integral of the respective distributions therefore has to yield compatible results since both represent the total π° cross section for the phase space $2.0 < Q^2 < 70.0$ GeV^2, $0.1 < y < 0.6$, $5^\circ < \theta_\pi < 25^\circ$ (lab), $x_\pi = E_\pi \,/\, E_{proton} > 0.01$ (lab) and $p_{T,\pi} > 2.5$ GeV (hadronic cms):

$$\sum_{i=1}^{3} \int \frac{d\sigma_\pi^i}{d\eta_\pi^i} d\eta_\pi^i \quad = \quad 513.5 \pm 16.2\,(\text{stat})\ \text{pb} \tag{6.9}$$

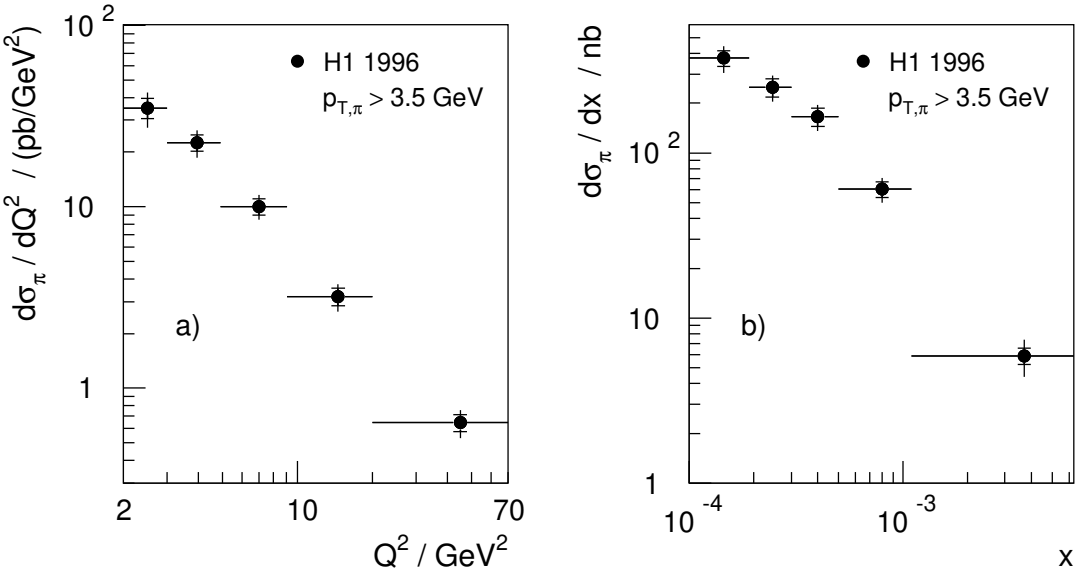

Figure 6.12: Differential π^0-meson production cross sections as a function of Q^2 (a) and x (b) for $p_{T,\pi} > 3.5$ GeV. The inner error represents the statistical uncertainty, the outer error is the quadratic sum of the statistical and the systematic error.

$$\int \frac{d\sigma_\pi}{dQ^2}\, dQ^2 \quad = \quad 527.7 \pm 16.4\,(\text{stat})\ \text{pb} \tag{6.10}$$

The sum in (6.9) extends over the three regions in Q^2 for $d\sigma_\pi/d\eta_\pi$. The two values are consistent with each other. It has to be noted, however, that the statistical errors given for both values are correlated, since the same events are used for both distributions. Figure 6.12 finally shows $d\sigma_\pi/dQ^2$ and $d\sigma_\pi/dx$ for the higher threshold of $p_{T,\pi} > 3.5$ GeV. No significant change in the shape of the distributions becomes evident when the $p_{T,\pi}$ threshold is raised, which in this case reduces the cross section by about a factor of three.

With this measurement it has become possible for the first time to measure observables of the hadronic final state in this region of the phase space with relatively small experimental uncertainties. It provides testing ground for any theory that claims to describe processes at small x with large phase space for parton emissions and a reasonably hard scale.

Chapter 7

Interpretation

Once the experimental results are available, one can set out to reach the goal formulated in the beginning: to learn something about the physics processes and dynamics involved in positron-proton scattering events at low x. In order to do so the predictions of several different approximations to QCD are tested against the distributions measured in the previous chapters. The ability of any given model or calculation to reproduce the experimental results is taken as a measure of how valid the mechanisms and assumptions used in each case are for the observables and phase space covered in this analysis. Unless stated otherwise the CTEQ4M parton densities are used in all calculations, which have been shown to be in good agreement with the total deep-inelastic cross section $\sigma^{eP}_{\text{incl}}$ as measured by H1 [38]. The relative rate of π° production in all deep-inelastic scattering events as a function of x and Q^2 is calculated from the measured cross sections. The behavior of the total deep-inelastic cross section can thereby be unfolded from the π° cross sections and one can study the probability of producing a high p_T π°-meson (and therefore a hard parton) in any region of x and Q^2 available. This chapter is structured as follows:

- The relative rate of π° production in all deep-inelastic scattering events is obtained from the π° cross sections.
- Phenomenological QCD models and an analytical calculation within the BFKL formalism in order $\mathcal{O}(\alpha_s)$ are introduced.
- Conclusions are drawn from the comparison of the available predictions to the data.

7.1 The Relative Rate of π° Production

Using the knowledge of the inclusive deep-inelastic cross section $\sigma^{eP}_{\rm incl}$ as measured by H1, the rate of π° production R_π in DIS events as a function of x and Q^2 can be calculated from the measured cross sections:

$$R_\pi(x,Q^2) \;=\; \frac{\sigma_\pi(x,Q^2)}{\sigma^{eP}_{\rm incl}(x,Q^2)}. \tag{7.1}$$

The phase space for the measurement of the inclusive cross section is subdivided into many more bins than available for the measurement of neutral pion cross sections (σ_π). A Monte Carlo event generator is used to integrate $\sigma^{eP}_{\rm incl}$ for each bin of the neutral pion cross sections by reweighting every event to reproduce the distribution measured for $\sigma^{eP}_{\rm incl}$ [28]. The total error of the $\sigma^{eP}_{\rm incl}$ data points is usually between 5 and 10 %. An additional error of 10 % is therefore added in quadrature to the systematic error of the σ_π measurement to estimate the error associated with the π° production rates.

7.2 Phenomenological QCD Models

A number of Monte Carlo models implementing $\mathcal{O}(\alpha_s)$ matrix elements and a parton cascade are available as event generators. The partonic final state produced by these programs is interfaced with a hadronization model. Their predictions can therefore directly be compared to the measured cross sections.

DGLAP inspired models with and without resolved photons

Implementations of $\mathcal{O}(\alpha_s)$ matrix elements complemented by parton showers based on the DGLAP splitting functions are available in the programs LEPTO [23] and HERWIG [39]. The predictions of these models should be valid in the DGLAP phase space: $\alpha_s(Q^2)\ln(Q^2/Q_0^2) \sim 1$ and $\alpha_s(Q^2)\ln(1/x) \ll 1$ (see Section 1.5). In LEPTO the Lund string model as implemented in JETSET [24] is used to describe hadronization processes. HERWIG differs from LEPTO in that it also considers interference effects due to color coherence and uses the cluster fragmentation model for hadronization (Section 1.9). LEPTO and HERWIG as used in this context only consider DIS processes in which the virtual photon is point-like.

Recently a model has become available (RAPGAP [40]) which is also based on the DGLAP formalism but includes contributions from processes in which the virtual photon entering the scattering process is resolved. The relative contribution from resolved processes depends on the scale at which the virtual photon is probed. Direct interactions, where the photon is considered point-like, are taken from LEPTO.

The color dipole model

The color dipole model provides an alternative description of parton cascades (Section 1.9). The parton radiation is described starting from a color dipole formed between the struck quark and the hadron remnant. Subsequent gluon radiation emanates from color dipoles spanned between the newly created color charges and the original color charges. The gluon emissions from this type of cascade are not ordered in k_T. In this respect the CDM resembles a BFKL-like chain of parton emissions, but without in fact using BFKL dynamics. An implementation of the CDM is available in ARIADNE [33].

Implementation of CCFM/LDC

The linked dipole chain (LDC) model is a reformulation of the CCFM evolution equation (Section 1.7). The phase space for parton emissions is here given by considering the coherent radiation of gluons, which leads to an angular ordering of the gluons along a chain of multiple emissions. The LDC is available as an event generator via the program LDCMC [41].

7.3 BFKL Calculation in Order $\mathcal{O}(\alpha_s)$ and Fragmentation Functions

The method of folding a perturbative calculation with fragmentation functions to obtain predictions for the hadronic final state was recently used by Kwiecinski, Martin and Outhwaite [42] to predict the π° cross sections within the BFKL formalism in order $\mathcal{O}(\alpha_s)$. As in the strategy outlined in [43, 44], kinematical constraints (which should perhaps more appropriately be called consistency constraints) are applied which restrict the phase space for gluon emissions. These constraints are believed to embody a major part of the non-leading $\ln(1/x)$ contribution. Since now the evolution is from the virtual photon end of the gluon chain, there is no longer any need for the free parameter z_0. Previously this parameter specified the starting point of the BFKL evolution and had to be matched to the data [10, 19]. The parton densities and fragmentation functions used in the calculation are taken from [45] and [46] respectively.

7.4 Comparisons to the Data

Before the theoretical predictions are compared to the data, it is useful to recall that the production of π°-mesons at high p_T is strongly correlated to the underlying parton dynamics (Section 1.8). The cross sections measured in this analysis can therefore be used to test the parton dynamics implemented in the QCD models and calculations. The following distributions have been measured in this analysis and are now available for further studies:

- *Differential π° cross sections as a function of Bjorken-x*: The phase space for different approximations of QCD covers different regions in x. DGLAP neglects $\ln(1/x)$ terms, while BFKL takes them to be dominant. The dependence of the cross sections on x is therefore a natural place to test where these approximations are applicable.

- *Differential π° cross sections as a function of Q^2*: The momentum transfer Q^2 for some models determines the scale at which the strong coupling constant is taken. Perturbative calculations become more reliable as the scale increases. Q^2 is also important for the contributions of resolved processes which increase towards low Q^2.

- *Differential π° cross sections as a function of η_π:* The production of hard partons (leading to high p_T particles) is strongly suppressed at large pseudo-rapidities for models which assume strong ordering in decreasing k_T for parton emissions starting from the photon vertex. This is the case for DGLAP-like parton emissions, but not for BFKL.

- *Differential π° cross sections as a function of $p_{T,\pi}$:* The dependence on $p_{T,\pi}$ is interesting for similar reasons to those given for Q^2. $p^2_{T,\pi}$ is a possible choice of the scale and likely to be the relevant one at low values of Q^2.

  For the same reasons cross sections as a function of x and Q^2 are also studied for a higher threshold of $p_{T,\pi}$.

The behavior of the data: The π° cross sections rise strongly towards low x (Figure 7.1 (a)). This steep rise, however, can be attributed to the rise of the total deep-inelastic cross section. The rate of high p_T π°-meson production in fact shows no dependence on x in any given range of Q^2 in Figure 7.1 (b). In terms of parton dynamics the conclusion therefore is that the probability of producing hard partons at large rapidities does not change with x. The production rates do decrease with decreasing Q^2 for fixed x.

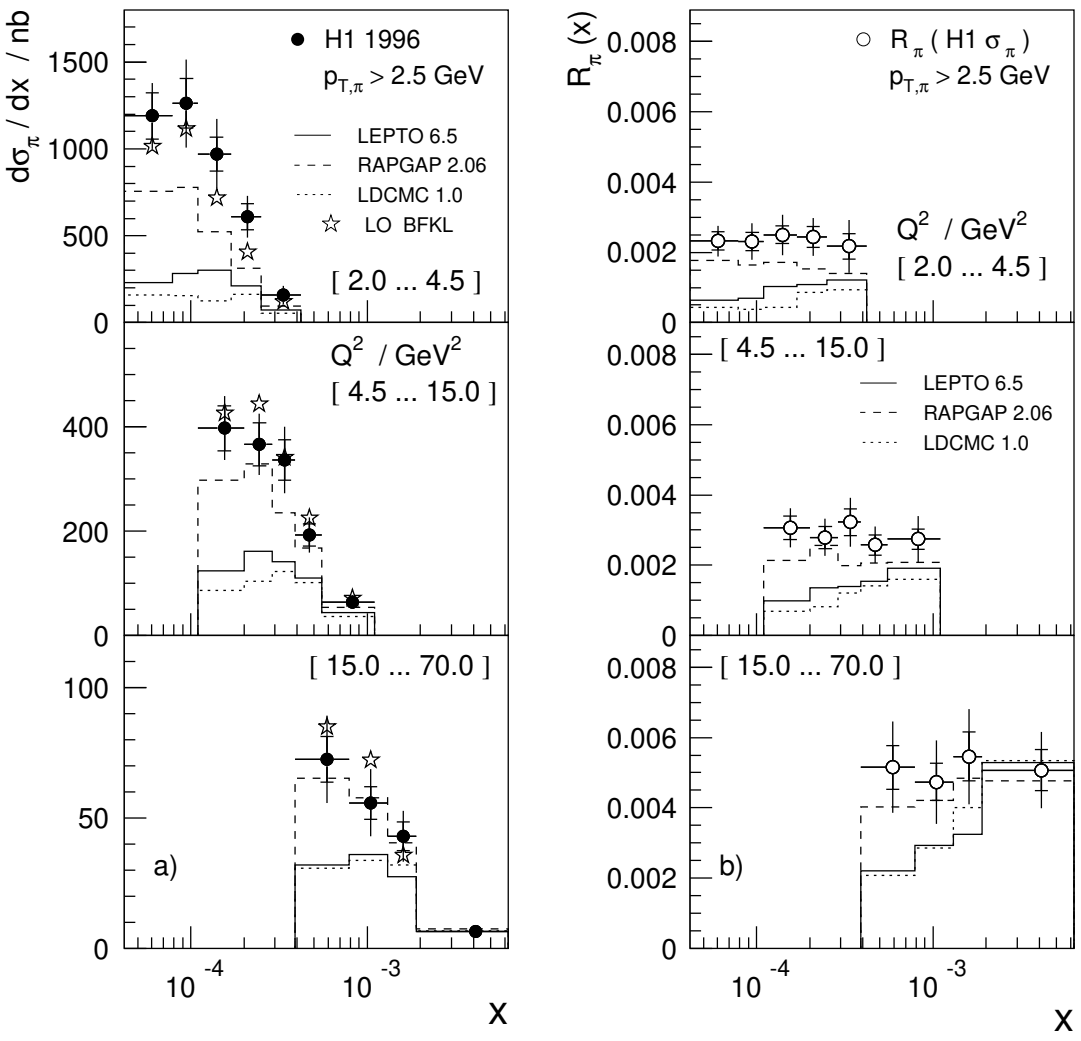

Figure 7.1: Differential π°-meson production cross sections (a) and the rate of π° production (b) as a function of x in three regions of Q^2 for $p_{T,\pi} > 2.5$ GeV. The phase space is given by $0.1 < y < 0.6$, $5^\circ < \theta_\pi < 25^\circ$ and $x_\pi > 0.01$ in addition to the restrictions given in the figure. θ_π and x_π are taken in the H1 laboratory frame, $p_{T,\pi}$ is calculated in the hadronic cms. The three QCD models LEPTO, RAPGAP and LDCMC are compared to the data. Also shown is the prediction of the LO BFKL calculation by Kwiecinski, Martin and Outhwaite [42].

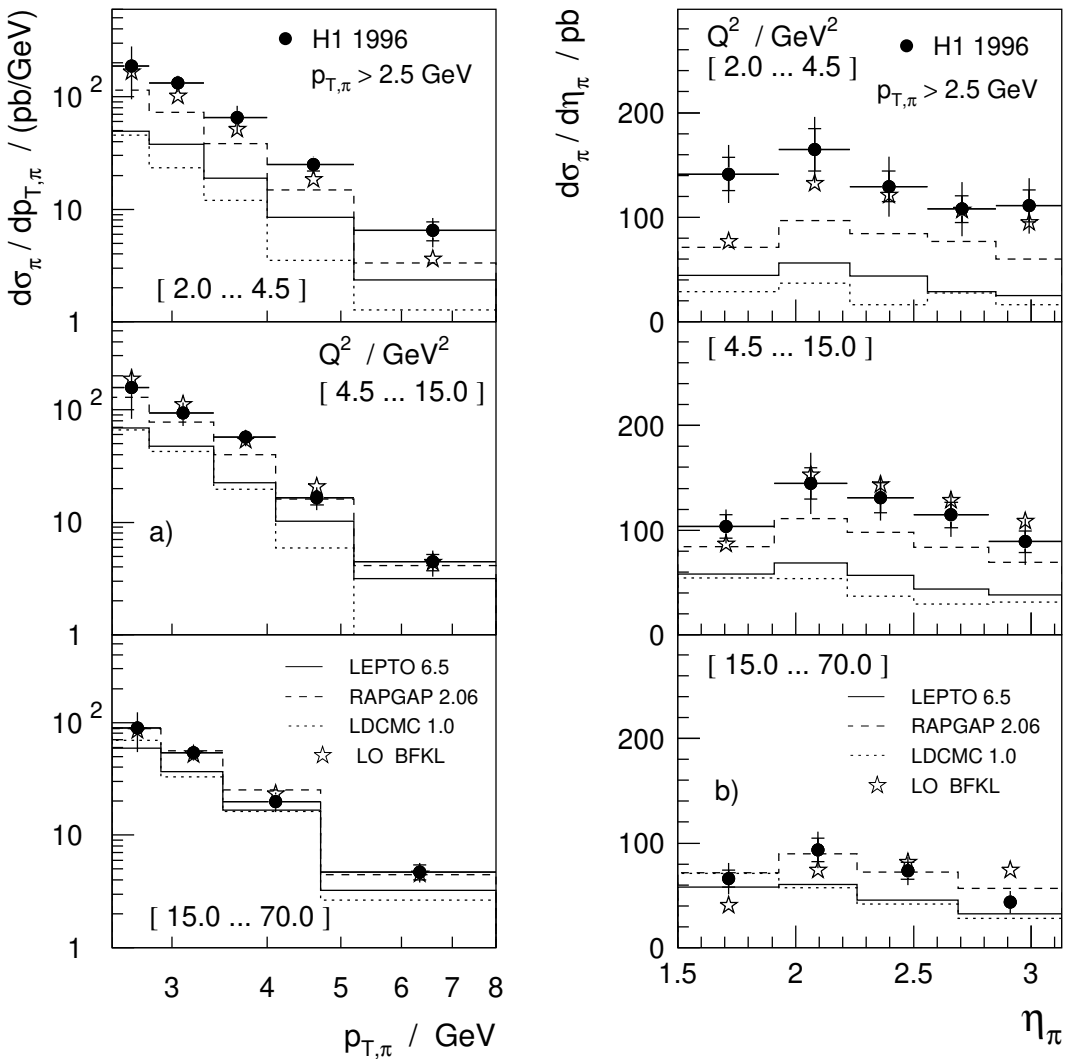

Figure 7.2: Differential π°-meson production cross sections as a function of $p_{T,\pi}$ (a) and η_π (b) in three regions of Q^2 for $p_{T,\pi} > 2.5$ GeV. The phase space is given by $0.1 < y < 0.6$, $5^\circ < \theta_\pi < 25^\circ$ and $x_\pi > 0.01$ in addition to the restrictions given in the figure. θ_π and x_π are taken in the H1 laboratory frame, $p_{T,\pi}$ is calculated in the hadronic cms. The three QCD models LEPTO, RAPGAP and LDCMC are compared to the data. Also shown is the prediction of the LO BFKL calculation by Kwiecinski, Martin and Outhwaite [42].

Comparison to DGLAP models: In Figure 7.1 (a) the π°-meson cross sections are shown as a function of x for $p_{T,\pi} > 2.5$ GeV. The DGLAP prediction (represented by LEPTO) is clearly below the data. While there is still reasonable agreement for the bin at highest x and Q^2 in Figure 7.1 (a), differences between the LEPTO prediction and the data increase up to a very significant factor of five in the low x region. The mechanism of emitting partons according to the DGLAP splitting functions is clearly not supported by the data especially at low x. This mechanism limits the phase space for hard QCD radiation at large rapidities such that the rate of events with a high p_T forward π°-meson actually decreases towards low x. Comparisons to HERWIG lead to the same conclusions as shown in Appendix B (Figure B.1 (a)). The discrepancies between the DGLAP models and the data do not depend significantly on the transverse momentum and pseudorapidity of the π°-mesons, as shown in Figure 7.2 (a) and (b).

Predictions using the color dipole cascade: The color dipole model as implemented in ARIADNE predicts cross sections which are above the measured values. However, these predictions turn out to be very sensitive to the 'target extension' parameter as demonstrated in Appendix B (Figure B.2 (a,b)). Deductions from a comparison to the data would therefore not be meaningful. The strong dependence of the predictions on this parameter can possibly be used to fix the value of the parameter for future comparisons.

Including resolved photon processes: A considerable improvement of the description is achieved by considering processes where the virtual photon entering the scattering process is resolved. Such a prediction is provided by RAPGAP. In Figure 7.1 RAPGAP can be seen to predict cross sections very close to the measured distributions apart from being too low for the lowest bin in Q^2. The reason for the large effect of resolved processes in RAPGAP on the π° cross sections is twofold. First, the resolved component as implemented in RAPGAP constitutes an additional contribution and therefore always enlarges the cross sections. Furthermore the hard subprocess (and also the available phase space for DGLAP-type parton emissions) is moved towards larger rapidities by allowing resolved processes at the photon vertex [47]. The relative contribution from resolved processes depends on the scale at which the virtual photon is probed. As in [47] the factorization and renormalization scale is here taken to be $Q^2 + p_T^2$ (p_T^2 of the partons from the hard subprocess). The predicted cross sections increase by up to 30 % when increasing the scale to $Q^2 + 4p_T^2$, as demonstrated in Figure B.1 (b). Whether this mechanism is adequate to describe the π° cross sections down to the lowest available x therefore cannot finally be decided by RAPGAP. However, the concept of including contributions from resolved photon processes leads to an overall good description of the data. This is true not only for the π° cross sections, but also for the forward jet cross section and the rate of dijet production in DIS events at low Q^2 [19, 48].

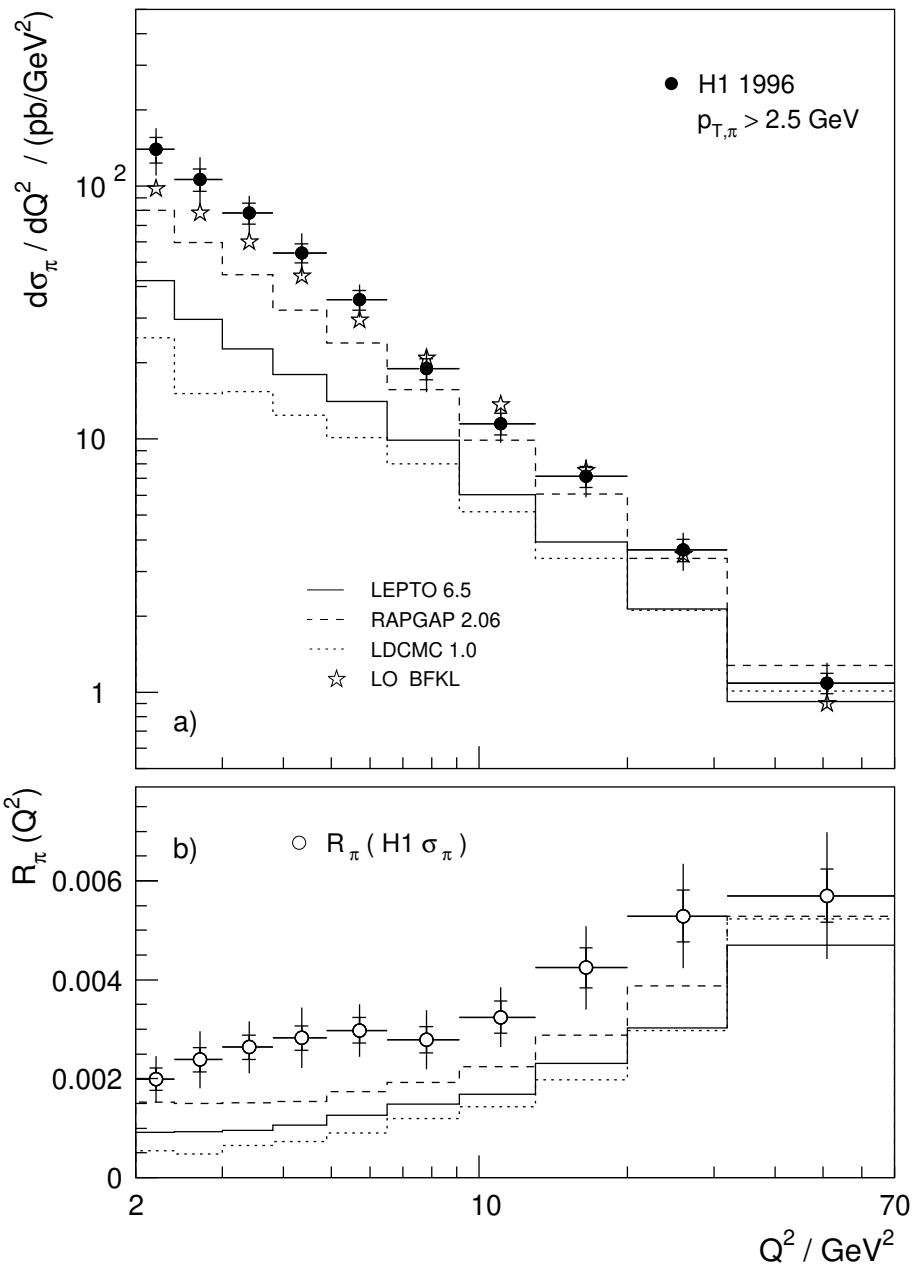

Figure 7.3: Differential π°-meson production cross sections (a) and the rate of π° production in DIS events (b) as a function of Q^2 for $p_{T,\pi} > 2.5$ GeV. The phase space is given by $0.1 < y < 0.6$, $5^\circ < \theta_\pi < 25^\circ$ and $x_\pi > 0.01$ in addition to the restrictions given in the figure. θ_π and x_π are taken in the H1 laboratory frame, $p_{T,\pi}$ is calculated in the hadronic cms. The three QCD models LEPTO, RAPGAP and LDCMC are compared to the data. Also shown is the prediction of the LO BFKL calculation by Kwiecinski, Martin and Outhwaite [42].

The importance of higher order calculations: Fixed order $\mathcal{O}(\alpha_s^2)$ calculations have been available for some time. Using fragmentation functions it should be possible to obtain predictions based on these calculations for the neutral pion cross sections. For these calculations the uncertainties associated with the choice of the renormalization and factorization scale as seen for the resolved contribution at leading order should be much reduced. Such calculations will hopefully be available in the near future.

The performance of LDC/CCFM: CCFM (and consequently LDC) is expected to be a good approximation of QCD at high x as well as at low x. Surprisingly, however, the LDCMC prediction is very close to the LEPTO prediction or even lower (i.e. further away from the data) as can be seen in Figures 7.1 – 7.4. It is as yet unclear whether the failure of LDCMC to describe the data really constitutes a failure of the implementation of the linked dipole chain model or even the CCFM equation, as additional assumptions are necessary to construct the event generator from the underlying model. Discrepancies between the LDCMC predictions and the measured values have been observed for other quantities as well, and are investigated in [49].

BFKL Calculation in order $\mathcal{O}(\alpha_s)$ and Fragmentation Functions: The most significant calculation so far uses the BFKL formalism in order $\mathcal{O}(\alpha_s)$. Fragmentation functions are used to calculate the π°-meson cross sections from the partonic final state. The predictions obtained with these calculations turn out to be in good agreement with the neutral pion cross sections measured in the entire available phase space with a slight tendency to be below the data at the lowest values of x available (Figures 7.1 (a), 7.2, 7.3 (a) and 7.4 (a,c)). Figure 7.2 (b) indicates that the existing discrepancies occur mostly at the largest accessible values of η_π. The calculation has one parameter k_0^2 which specifies the infrared cutoff for gluon emissions. This cutoff was chosen to be 0.5 GeV^2. Changing it to 1.0 GeV^2 results in a decrease of the predicted cross sections by about 10 %. The good description of the data can be interpreted as evidence that the major higher order contributions are indeed covered by imposing kinematical constraints according to [43, 44] in the calculation.

To summarize the discussion above: Models using $\mathcal{O}(\alpha_s)$ QCD matrix elements and parton cascades according to the DGLAP splitting functions cannot describe the differential neutral pion cross sections at low x. Including processes in which the virtual photon is resolved leads to an improved description of the data. Renormalization and factorization scale uncertainties however limit the precision of the predictions. $\mathcal{O}(\alpha_s^2)$ calculations are needed to reduce the dependency of the calculated cross sections on the scales. An implementation of the linked dipole

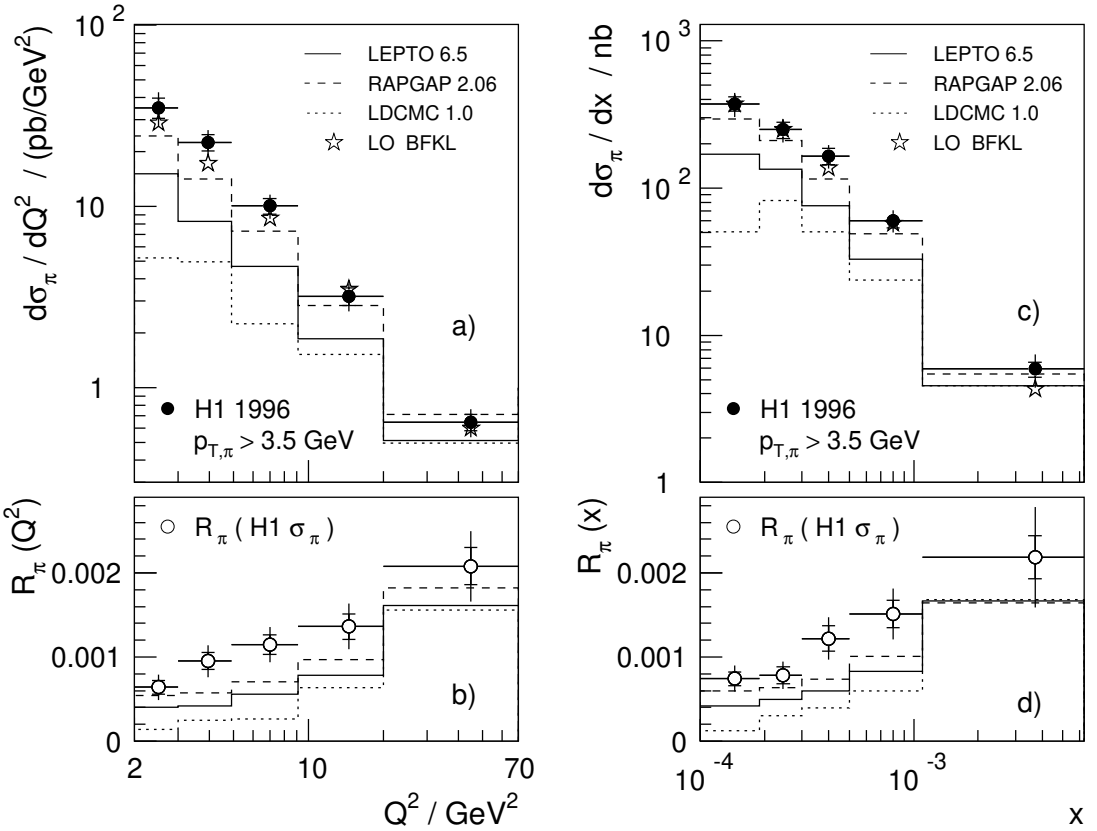

Figure 7.4: Differential π°-meson production cross sections (a,c) and the rate of π° production in DIS events (b,d) as a function of Q^2 and x for $p_{T,\pi} > 3.5$ GeV. The phase space is given by $0.1 < y < 0.6$, $5^\circ < \theta_\pi < 25^\circ$ and $x_\pi > 0.01$ in addition to the restrictions given in the figure. θ_π and x_π are taken in the H1 laboratory frame, $p_{T,\pi}$ is calculated in the hadronic cms. The three QCD models LEPTO, RAPGAP and LDCMC are compared to the data. Also shown is the prediction of the LO BFKL calculation by Kwiecinski, Martin and Outhwaite [42].

chain reformulation of the CCFM equation yields predictions for the measured cross sections even further away from the data than those based on DGLAP dynamics. A calculation based on the BFKL formalism is in good agreement with the data. Considering the relatively small uncertainties given for this calculation it is the best available approximation of QCD in the considered phase space.

Summary

The aim of the present analysis has been to study experimentally the physics processes and dynamics involved in positron-proton scattering events at low x. Observables are defined which are sensitive to the parton dynamics and therefore can discriminate between the available models and approximations of QCD. Large differences are expected especially for the region close to the proton remnant. The production of single particles with high transverse momentum is shown to be strongly correlated to the underlying hard partons by studying their relationship in simulated DIS events. Experimentally the π°-meson is the most suitable particle for this measurement, since it can be identified and measured based on calorimetric information at high momenta and in an environment with high particle and energy density.

The observables are differential high p_T π°-meson production cross sections in deep-inelastic positron-proton scattering. The cross sections are measured as a function of the kinematical variables Q^2 and Bjorken-x and as a function of the transverse momentum $p_{T,\pi}$ and the pseudorapidity η_π of the π°-mesons. The DIS phase space considered covers the range $2.0 < Q^2 < 70.0$ GeV^2 and extends over two orders of magnitude in x down to $x \approx 5{\cdot}10^{-5}$. The π° cross sections are measured for small polar angles with respect to the incident proton direction and for two $p_{T,\pi}$ thresholds. Corrections are applied for detector effects and for the influence of QED radiation. Typical systematic uncertainties for the cross sections measured are around 15 %, compared to statistical uncertainties of about 10 %.

For the first time, observables of the hadronic final state have been measured which are sensitive to high p_T parton production at very low x and close to the proton remnant. Unlike in the forward jet measurement [19], no strong kinematical bias is introduced. The differential π° cross sections therefore provide novel testing ground for any theory that claims to describe processes at small x with high p_T parton emissions.

The π° cross sections rise strongly towards low x. The rate of high p_T π°-meson production, however, shows no dependence on x in any given range of Q^2. In terms

of parton dynamics the conclusion therefore is that the probability of producing hard partons at large rapidities does not change with x. The production rates do decrease with decreasing Q^2 for fixed x.

Comparisons to theoretical predictions lead to the following conclusions:

- Calculations using $\mathcal{O}(\alpha_s)$ QCD matrix elements and parton cascades based on the DGLAP splitting functions cannot describe the π° cross sections measured at low x.
- Including processes where the virtual photon is resolved leads to an improved description of the data. Renormalization and factorization scale uncertainties however limit the precision of the predictions especially for the resolved contributions.
- $\mathcal{O}(\alpha_s^2)$ calculations are needed to reduce the dependency of the calculated cross sections on the scales. Such calculations will hopefully be available in the near future.
- An implementation of the linked dipole chain reformulation of the CCFM equation fails to describe the data.
- A calculation within the BFKL formalism is in good agreement with the data, implying that this approach is a valid approximation of QCD in the phase space considered. It should be noted that the same BFKL calculation is also in good agreement with the forward jet cross section as measured by H1 [19, 42].

In the future it should be possible to draw firmer conclusions from comparisons to $\mathcal{O}(\alpha_s^2)$ calculations. It is worth recalling from Section 1.8 that the π° on average carries only 40 % of the transverse momentum of the original parton(-jet). The scale can therefore easily reach values of above 30 GeV^2, which should be sufficient for meaningful $\mathcal{O}(\alpha_s^2)$ predictions. It will be very interesting to see if these calculations give predictions as close to the data as the BFKL calculation described above.

Finally it should be noted that the concept of including resolved contributions in low Q^2 deep-inelastic scattering leads to a good description not only of the π°-meson cross sections, but also, for example, of the forward jet cross section and dijet event rate [19, 48] at low Q^2. Both observables are not described by DGLAP-type models including only direct interactions with a point-like photon. The dijet event rates, however, are also well reproduced by an order $\mathcal{O}(\alpha_s^2)$ calculation. Including resolved components is apparently an effective method of describing higher order effects.

Appendix A

Cross Sections

In this chapter the numerical values of the π° cross sections are given. The tables list the differential cross section for each bin of the distributions measured together with the respective statistical and total error. The following phase space definitions are common to all of the cross sections and are therefore not listed in the individual tables: $0.1 < y < 0.6$ (DIS phase space), $5^\circ < \theta_\pi < 25^\circ$ and $x_\pi = E_\pi \,/\, E_{proton} > 0.01$ (π° phase space, H1 laboratory frame of reference).

bin in Q^2 /GeV^2	$\mathrm{d}\sigma_\pi/\mathrm{d}Q^2$ / $\frac{\mathrm{pb}}{\mathrm{GeV}^2}$	$\pm\delta_{\mathrm{stat}}$ / $\frac{\mathrm{pb}}{\mathrm{GeV}^2}$	$\pm\delta_{\mathrm{tot}}$ / $\frac{\mathrm{pb}}{\mathrm{GeV}^2}$
$2.0 < Q^2 < 70.0$ GeV^2	$p_{T,\pi} > 2.5$ GeV (hcms)		
2.00 – 2.40	139	16	29
2.40 – 3.00	106	11	23
3.00 – 3.80	78.2	7.3	13.3
3.80 – 4.90	54.5	4.8	10.5
4.90 – 6.50	35.5	3.1	5.3
6.50 – 9.10	19.0	1.8	3.6
9.10 – 13.0	11.5	1.1	1.8
13.0 – 20.0	7.12	0.68	1.23
20.0 – 32.0	3.64	0.36	0.63
32.0 – 70.0	1.08	0.10	0.22

Table A.1: The numerical values of the differential π° cross section as a function of Q^2 for $p_{T,\pi} > 2.5$ GeV (hadronic cms) as shown in Figure 6.11. The value of the cross section is presented together with the respective statistical and total error.

bin in x	$\mathrm{d}\sigma_\pi/\mathrm{d}x$ /nb	$\pm\delta_{\mathrm{stat}}$ /nb	$\pm\delta_{\mathrm{tot}}$ /nb
$2.0 < Q^2 < 4.5$ GeV^2 $\quad p_{T,\pi} > 2.5$ GeV (hcms)			
0.000042 – 0.000079	1189	134	188
0.000079 – 0.00011	1261	143	253
0.00011 – 0.00017	970	96	201
0.00017 – 0.00025	609	75	121
0.00025 – 0.00042	160	27	52

bin in x	$\mathrm{d}\sigma_\pi/\mathrm{d}x$ /nb	$\pm\delta_{\mathrm{stat}}$ /nb	$\pm\delta_{\mathrm{tot}}$ /nb
$4.5 < Q^2 < 15.0$ GeV^2 $\quad p_{T,\pi} > 2.5$ GeV (hcms)			
0.00011 – 0.00020	398	43	61
0.00020 – 0.00029	366	41	59
0.00029 – 0.00039	337	39	64
0.00039 – 0.00055	193	21	34
0.00055 – 0.0011	63.5	6.8	13.8

bin in x	$\mathrm{d}\sigma_\pi/\mathrm{d}x$ /nb	$\pm\delta_{\mathrm{stat}}$ /nb	$\pm\delta_{\mathrm{tot}}$ /nb
$15.0 < Q^2 < 70.0$ GeV^2 $\quad p_{T,\pi} > 2.5$ GeV (hcms)			
0.00039 – 0.00079	72.4	8.7	16.8
0.00079 – 0.0013	55.8	6.3	12.9
0.0013 – 0.0019	43.1	5.5	9.8
0.0019 – 0.0063	6.44	0.74	1.23

Table A.2: The numerical values of the differential π° cross section as a function of x for $p_{T,\pi} > 2.5$ GeV (hadronic cms) in three regions of Q^2 as shown in Figure 6.9. The value of the cross section is presented together with the respective statistical and total error.

bin in $p_{T,\pi}$ /GeV	$\mathrm{d}\sigma_\pi/\mathrm{d}p_{T,\pi}$ / $\frac{\mathrm{pb}}{\mathrm{GeV}}$	$\pm\delta_{\mathrm{stat}}$ / $\frac{\mathrm{pb}}{\mathrm{GeV}}$	$\pm\delta_{\mathrm{tot}}$ / $\frac{\mathrm{pb}}{\mathrm{GeV}}$
$2.0 < Q^2 < 4.5$ GeV^2 $\quad p_{T,\pi} > 2.5$ GeV (hcms)			
2.50 – 2.80	187	20	92
2.80 – 3.30	132	13	22
3.30 – 4.00	65.3	7.5	17.5
4.00 – 5.20	25.1	3.4	4.2
5.20 – 8.00	6.48	1.23	1.86

bin in $p_{T,\pi}$ /GeV	$\mathrm{d}\sigma_\pi/\mathrm{d}p_{T,\pi}$ / $\frac{\mathrm{pb}}{\mathrm{GeV}}$	$\pm\delta_{\mathrm{stat}}$ / $\frac{\mathrm{pb}}{\mathrm{GeV}}$	$\pm\delta_{\mathrm{tot}}$ / $\frac{\mathrm{pb}}{\mathrm{GeV}}$
$4.5 < Q^2 < 15.0$ GeV^2 $\quad p_{T,\pi} > 2.5$ GeV (hcms)			
2.50 – 2.80	157	15	74
2.80 – 3.40	93.5	7.8	21.7
3.40 – 4.10	56.9	6.4	9.5
4.10 – 5.20	16.6	2.4	3.8
5.20 – 8.00	4.45	0.75	1.18

bin in $p_{T,\pi}$ /GeV	$\mathrm{d}\sigma_\pi/\mathrm{d}p_{T,\pi}$ / $\frac{\mathrm{pb}}{\mathrm{GeV}}$	$\pm\delta_{\mathrm{stat}}$ / $\frac{\mathrm{pb}}{\mathrm{GeV}}$	$\pm\delta_{\mathrm{tot}}$ / $\frac{\mathrm{pb}}{\mathrm{GeV}}$
$15.0 < Q^2 < 70.0$ GeV^2 $\quad p_{T,\pi} > 2.5$ GeV (hcms)			
2.50 – 2.90	89.0	9.5	34.7
2.90 – 3.50	54.0	5.9	8.4
3.50 – 4.70	19.9	2.5	3.9
4.70 – 8.00	4.72	0.72	0.94

Table A.3: The numerical values of the differential π° cross section as a function of $p_{T,\pi}$ (hadronic cms) for $p_{T,\pi} > 2.5$ GeV (hcms) in three regions of Q^2 as shown in Figure 6.10 (a). The value of the cross section is presented together with the respective statistical and total error.

bin in η_π	$d\sigma_\pi/d\eta_\pi$ /pb	$\pm\delta_{stat}$ /pb	$\pm\delta_{tot}$ /pb
$2.0 < Q^2 < 4.5$ GeV^2		$p_{T,\pi} > 2.5$ GeV (hcms)	
1.50 – 1.93	141	16	28
1.93 – 2.23	165	20	31
2.23 – 2.56	129	15	29
2.56 – 2.85	108	13	26
2.85 – 3.13	111	15	26

bin in η_π	$d\sigma_\pi/d\eta_\pi$ /pb	$\pm\delta_{stat}$ /pb	$\pm\delta_{tot}$ /pb
$4.5 < Q^2 < 15.0$ GeV^2		$p_{T,\pi} > 2.5$ GeV (hcms)	
1.50 – 1.91	103	11	16
1.91 – 2.22	145	15	29
2.22 – 2.50	131	14	21
2.50 – 2.82	115	12	21
2.82 – 3.13	89.0	10.2	22.1

bin in η_π	$d\sigma_\pi/d\eta_\pi$ /pb	$\pm\delta_{stat}$ /pb	$\pm\delta_{tot}$ /pb
$15.0 < Q^2 < 70.0$ GeV^2		$p_{T,\pi} > 2.5$ GeV (hcms)	
1.50 – 1.93	66.2	7.9	14.9
1.93 – 2.26	93.5	11.2	17.5
2.26 – 2.69	73.2	8.1	13.5
2.69 – 3.13	43.6	5.4	10.6

Table A.4: The numerical values of the differential π° cross section as a function of η_π for $p_{T,\pi} > 2.5$ GeV (hadronic cms) in three regions of Q^2 as shown in Figure 6.10 (b). The value of the cross section is presented together with the respective statistical and total error.

bin in x	$\mathrm{d}\sigma_\pi/\mathrm{d}x$ /nb	$\pm\delta_{\mathrm{stat}}$ /nb	$\pm\delta_{\mathrm{tot}}$ /nb
$2.0 < Q^2 < 70.0$ GeV^2 $\quad p_{T,\pi} > 3.5$ GeV (hcms)			
0.00010 – 0.00019	374	41	70
0.00019 – 0.00030	249	32	45
0.00030 – 0.00050	165	21	30
0.00050 – 0.0011	60.3	6.5	10.5
0.0011 – 0.0063	5.90	0.69	1.50

Table A.5: The numerical values of the differential π° cross section as a function of x for $p_{T,\pi} > 3.5$ GeV (hadronic cms) as shown in Figure 6.12 (a). The value of the cross section is presented together with the respective statistical and total error.

bin in Q^2 /GeV^2	$\mathrm{d}\sigma_\pi/\mathrm{d}Q^2$ / $\frac{\mathrm{pb}}{\mathrm{GeV}^2}$	$\pm\delta_{\mathrm{stat}}$ / $\frac{\mathrm{pb}}{\mathrm{GeV}^2}$	$\pm\delta_{\mathrm{tot}}$ / $\frac{\mathrm{pb}}{\mathrm{GeV}^2}$
$2.0 < Q^2 < 70.0$ GeV^2 $\quad p_{T,\pi} > 3.5$ GeV (hcms)			
2.00 – 3.00	35.0	4.4	7.7
3.00 – 4.90	22.5	2.3	3.9
4.90 – 9.10	10.0	1.0	1.5
9.10 – 20.0	3.20	0.35	0.55
20.0 – 70.0	0.64	0.07	0.11

Table A.6: The numerical values of the differential π° cross section as a function of Q^2 for $p_{T,\pi} > 3.5$ GeV (hadronic cms) as shown in Figure 6.12 (b). The value of the cross section is presented together with the respective statistical and total error.

Appendix B

Variation of Model Parameters

Implementations of the QCD models compared to the data in Chapter 7 are investigated for their sensitivity to some of their input parameters.

LEPTO

LEPTO [23] models DIS interactions using $\mathcal{O}(\alpha_s)$ matrix elements and Leading Log $\ln(Q^2)$ parton showers. No mechanism was originally foreseen to generate events with a large rapidity gap as observed at HERA. The concept of soft color interactions (SCI) is used in LEPTO to describe the appearance of such events. All partons and the proton remnant constitute a set of color charges. Each pair of charges can make a soft interaction (changing only the color but not the momenta) by a soft non-perturbative gluon exchange. The exchange probability cannot be calculated but is described by a parameter. In some cases color singlet subsystems arise from such interactions which are separated in rapidity. Rapidity gaps may occur when a gap is not spanned by a string. SCI also gives rise to string topologies without gaps where the string goes back and forth in rapidity between the partons. In such cases, there will be more particles and energy per unit rapidity and hence a higher energy flow. In particular this last feature makes it interesting to study the effect of SCI on the neutral pion cross sections. Comparing the LEPTO predictions in Figure B.1 (a) with (+SCI) and without (-SCI) the soft color interaction switched on demonstrates that the observables are not very sensitive to the effects of SCI.

The other label of the LEPTO prediction in Figure B.1 (a) – SQT – denotes the treatment of sea quarks as implemented in LEPTO. Starting from version LEPTO 6.3 the sea quark partner of a struck sea quark will be at the end-point of a color string and not, as previously, go directly into a hadron together with another spectator parton. Through hadronization this string will contribute to the forward transverse energy flow [50]. The new sea quark treatment however has no significant effect on the predictions for the π° cross sections as can be seen in Figure B.1 (a).

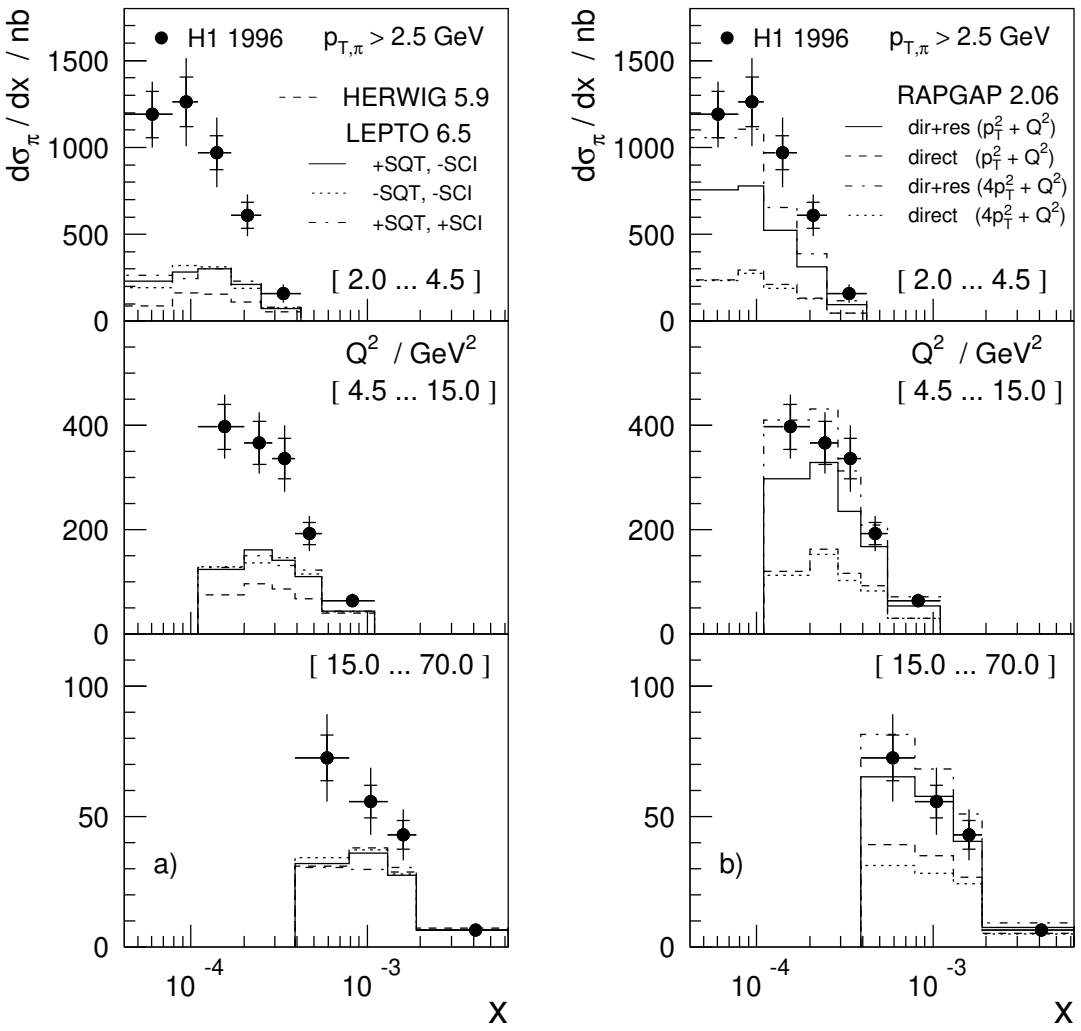

Figure B.1: The effect of input parameter variations for QCD models: Figure (a) compares LEPTO with/without soft color interaction (SCI) and with/without the new sea quark treatment (SQT) to the differential π°-meson cross sections as a function of x in three regions of Q^2. Also shown in Figure (a) is the HERWIG prediction. Figure (b) demonstrates the dependence of the RAPGAP prediction on the choice of renormalization and factorization scale. The contribution from direct processes is shown as well as the sum of direct and resolved contributions.

HERWIG

HERWIG [39] is based on very similar model assumptions to LEPTO. As in LEPTO, matrix elements up to $\mathcal{O}(\alpha_s)$ and parton showers in the Leading Log $\ln(Q^2)$ approximation of QCD are used to generate the partonic final state. HERWIG, however,

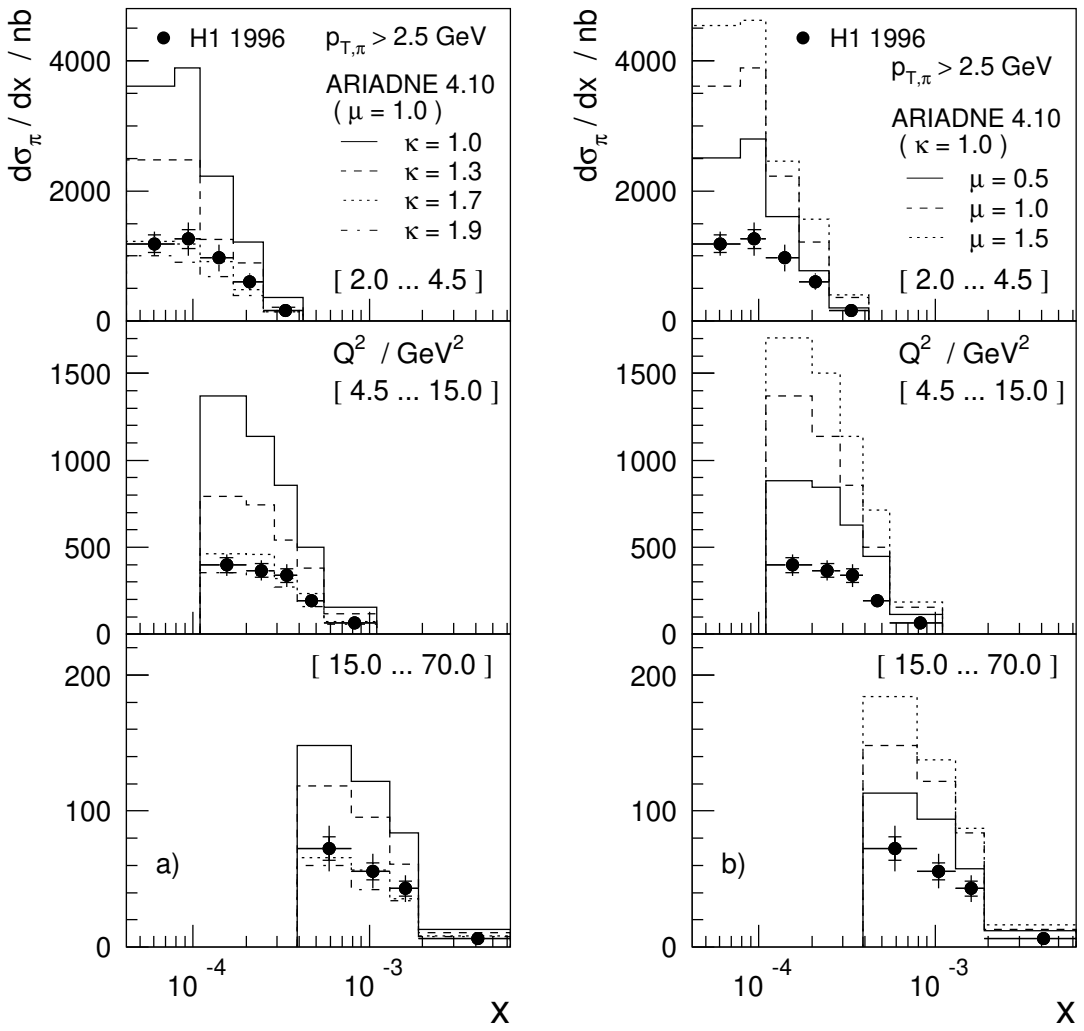

Figure B.2: The effect of input parameter variations for QCD models: The fraction of the proton remnant as a color antenna involved in the radiation is governed by $a = (\mu/k_T)^\kappa$. Figure (a) shows the dependency of the ARIADNE prediction on κ with μ at its default value. Figure (b) shows the dependency on μ with κ at its default value.

also considers interference effects due to color coherence. Hadronization processes in HERWIG are based on an implementation of the cluster fragmentation model (see Section 1.9). The HERWIG prediction is shown in Figure B.1 (a). HERWIG shows no significant difference from LEPTO in the region $15 < Q^2 < 70$ GeV^2, but falls below LEPTO (i.e. further away from the data) when moving towards lower Q^2. The differences between HERWIG and LEPTO are likely to arise from the different choice of renormalization and factorization scale made in the two programs. While

Q^2 is used in LEPTO, HERWIG takes the p_T^2 of the hard subprocess. The latter is on average constant while the decreasing Q^2 causes larger values of α_s and therefore larger values of the predicted π° cross sections in LEPTO.

ARIADNE

An alternative approach to model QCD radiation is implemented in ARIADNE [33]. Radiating color dipoles are used according to the CDM (Section 1.9). Since Ariadne only handles the QCD cascade it has to be interfaced with other programs which handle hard interactions and hadronization. The former is usually supplied by running ARIADNE in the LEPTO framework. Hadronization processes are modeled by JETSET (string fragmentation). A target extension parameter is introduced to account for the extended nature of the proton remnant as a color charge. The extension of the proton remnant causes a suppression of short wavelength radiated from a color dipole spanned between the remnant and another color charge. This phase space restriction is governed by $a = (\mu/k_T)^\kappa$ [51], where a is the fraction of the color antenna involved in the radiation, μ (`PARA(14)` in ARIADNE) is related to the typical inverse size of a hadron and κ (`PARA(10)`) governs the distribution of the energy along the dipole. Figures B.2 (a) and (b) demonstrate a strong dependence of the predicted π° cross sections on both μ and κ. Although making the predictions themselves rather uncertain, this strong dependence can be used to fix the values of μ and κ for future comparisons.

RAPGAP

As the name suggests, RAPGAP [40] was originally intended to model events with a large rapidity gap. They are described by scattering on a color neutral object, the pomeron. The present version also offers standard DIS event generation, very similar to LEPTO. First order α_s matrix elements are matched with Leading Log parton showers based on the DGLAP splitting functions. In addition to photon-proton scattering where the photon is point-like (direct interaction), RAPGAP also includes processes where the hadronic structure of the photon is resolved (resolved interaction). Such contributions are well known from photoproduction, but may also be important in DIS when Q^2 is small and the scale of the hard subprocess is larger than Q^2. In leading order α_s the renormalization scale and factorization scale are not well defined. RAPGAP therefore allows the variation of the scales to study the uncertainty associated with the respective choice. It should be noted that these uncertainties also apply to the leading order α_s implementations used in the other programs discussed in this chapter. Figure B.1 (b) shows the effect of changing the renormalization and factorization scale from $Q^2 + p_T^2$ (p_T^2 of the partons from the hard subprocess) to $Q^2 + 4p_T^2$ [47]. The effect is quite sizeable, increasing the predictions by up to 30 %. The direct contributions in RAPGAP especially at low x

are not significantly affected by increasing the scales. They are indeed very close to the LEPTO predictions in Figure B.1 (a). The contribution of resolved processes in RAPGAP is governed by the scale which determines whether the virtual photon can be resolved or not. Order $\mathcal{O}(\alpha_s^2)$ calculations are needed to reduce the uncertainties associated with the choice of renormalization and factorization scale. This will then also reduce the uncertainties visible in Figure B.1 (b).

Bibliography

[1] F. Halzen and A.D. Martin, Quarks and Leptons, Wiley & Sons, New York, 1984.

[2] O. Nachtmann, Elementary Particle Physics, Springer, New York, 1990.

[3] Review of Particle Physics, PDG, Eur. Phys. J. **C3** (1998) 1.

[4] R.P. Feynman, Phys. Rev. Lett. **23** (1969) 1415.

[5] J.D. Bjorken, Phys. Rev. **179** (1969) 1547.

[6] M. Breidenbach et al., Phys. Rev. Lett. **23** (1969) 935.

[7] M. Gell-Mann, Phys. Lett. **8** (1964) 214.

[8] F. Eisele, Invited Talk at XVIII Physics in Collision, Frascati, Italy, 1998; hep-ex/9807028.

[9] V.N. Gribov and L.N. Lipatov, Sov. J. Nucl. Phys. **15** (1972) 438 and 675; Yu. L. Dokshitzer, Sov. Phys. JETP 46 (1977) 641; G. Altarelli and G. Parisi, Nucl. Phys. 126 (1977) 297.

[10] J. Kwiecinski, S.C. Lang and A.D. Martin, Phys. Rev. **D55** (1997) 1273; hep-ph/9707240.

[11] E.A. Kuraev, L.N. Lipatov and V.S. Fadin, Sov. Phys. JETP **45** (1972) 199; Y.Y. Balitsky and L.N. Lipatov, Sov. J. Nucl. Phys. **28** (1978) 822.

[12] L.N. Lipatov, Perturbative QCD, edited by A.H. Mueller, World Scientific, Singapore, 1989.

[13] V.S. Fadin and L.N. Lipatov, Phys. Lett. **B429** (1998) 127.

[14] M. Ciafaloni, Nucl. Phys. **B296** (1988) 49; S. Catani, F. Fiorani and G. Marchesini, Phys. Let. **234B** (1990) 339 and Nucl. Phys. **B336** (1990) 18.

[15] P.J. Sutton, Acta Phys. Pol. **B27** (1995) 1323.

[16] B. Andersson, G. Gustafson, J. Samuelsson, Nucl. Phys. **B467** (1996) 443;
B. Andersson, G. Gustafson, H. Kharraziha, J. Samuelsson, Z. Phys. **C71** (1996) 613.

[17] G. Gustafson and Ulf Petterson, Nucl. Phys. B 306 (1988);
G. Gustafson, Phys. Lett. B 175 (1986) 453;
B. Andersson, G. Gustafson, L. Lönnblad, Ulf Petterson, Z. Phys. C 43 (1989) 625.

[18] H1 Collab., C. Adloff et al., contrib. paper pa02-073 to ICHEP'96, Warsaw 1996; M.F. Hess, Dissertation Univ. Hamburg, 1996.

[19] H1 Collab., C. Adloff et al., DESY-98-143, Submitted to Nucl. Phys. B.

[20] M. Kuhlen, Habilitation, Univ. Hamburg, 1997; hep-ph/9712505.

[21] A. H. Mueller, Nucl. Phys. B (Proc. Suppl.) **18C** (1990) 125;
J. Phys. **G17** (1991) 1443.

[22] ZEUS Collab., J. Breitweg et al., DESY-98-050, hep-ex/9805016.

[23] G. Ingelman, A. Edin and J. Rathsman, Comp. Phys. Comm. **101** (1997) 108.

[24] T. Sjöstrand, Comp. Phys. Comm. **39** (1986) 347;
T. Sjöstrand and M. Bengtsson, ibid. **43** (1987) 367.

[25] S.D. Ellis and D.E. Soper, Phys. Rev. **D48** (1993) 3160;
S. Catani, Yu.L. Dokshitzer, M.H. Seymour and B.R. Webber, Nucl. Phys. **B406** (1993) 187.

[26] R.K. Ellis, W.J. Stirling and B.R. Webber, QCD and Collider Physics, Cambridge University Press, Cambridge, 1996.

[27] B.R. Webber, Nucl. Phys. B 238 (1984) 492.

[28] A.A. Glazov, Dissertation, Univ. Berlin, 1998.

[29] H1 Collab., I. Abt et al., Nucl. Instr. and Meth. **A386** (1997) 310 and 348.

[30] H1 SPACAL Group, R.D. Appuhn, et al., Nucl. Instr. and Meth. **A374** (1996) 149 and **A386** (1997) 397.

[31] R. Brun and F. Carminati, GEANT Detector Description and Simulation Tool, CERN Program Library W5013, 1993.

[32] K. Charchula, G. Schuler, H. Spiesberger, Comp. Phys. Comm. **81** (1994) 381.

[33] L. Lönnblad, Comp. Phys. Comm. **71** (1992) 15.

[34] R. Engel, Z. Phys. **C66** (1995) 203;
R. Engel and J. Ranft, Phys. Rev. **D54** (1996) 4244.

[35] H1 Calorimeter Group, B. Andrieu, et al., Nucl. Instr. and Meth. **A334** (1994) 492.

[36] M. Wobisch, Diploma Thesis, RWTH Aachen, PITHA 95/38, 1995.

[37] B. Heinemann, Dissertation, Univ. Hamburg, in preparation.

[38] CTEQ Collab., H.L. Lai et al., Phys.Rev. **D55** (1997) 1280.

[39] G. Marchesini et al., Comp. Phys. Comm. **67** (1992) 465;
M.H. Seymour, Nucl. Phys. **B436** (1995) 443.

[40] H. Jung, Comp. Phys. Comm. 86 (1995) 147;
(for update see http://www-h1.desy.de/~jung/rapgap/rapgap.html).

[41] H. Kharraziha and L. Lönnblad, Lund preprint LU-TP 97-21; hep-ph/9709424.

[42] J. Outhwaite, private communication.

[43] J. Kwiecinski, A.D. Martin and P.J. Sutton, Z. Phys. **C71** (1996) 585.

[44] J. Kwiecinski, A.D. Martin and A.M. Stasto, Phys. Rev. **D56** (1997) 3991.

[45] A.D. Martin, R.G. Roberts, W.J. Stirling, R.S. Thorne, Eur. Phys. J. **C4** (1998) 463.

[46] J. Binnewies, B.A. Kniehl and G. Kramer, Phys.Rev. **D52** (1995) 4947.

[47] H. Jung, L. Jönsson and H. Kuester, DESY 98-051, hep-ph/9805396.

[48] H1 Collab., C. Adloff et al., DESY-98-076, Submitted to Eur. Phys. J.

[49] H. Kharraziha and L. Lönnblad, J. High Energy Phys. **3** (1998) 6.

[50] A.Edin, G. Ingelmann and J. Rahtsman, Phys. Lett. **B366** (1996) 371.

[51] Future Physics at HERA, ed. by G. Ingelmann, A. De Roeck and R. Klanner, p. 613.

Acknowledgments

During my time with the H1 experiment I have profited very much from the open and friendly atmosphere in the collaboration and at my home institute in Heidelberg. Many people willingly provided help whenever necessary. Although this cannot be a complete list, I wish to take the time to thank a few of them.

First, many thanks to my advisor, Prof. Franz Eisele. There was never any mistaking exactly what his high standards were. His help (and funding) were invaluable to me.

Many people have put in years of work to construct and maintain the experimental apparatus that was used in this analysis. They are too numerous to be all listed here. Among them, I would like to mention the engineers, technicians and physicists at Heidelberg and in the North Hall involved in constructing, installing and maintaining the Backward Drift Chamber of H1. Thank you for the excellent work.

For the first two years I was supported by a scholarship for which I would like to thank the Hermann-Schlosser-Foundation, and especially Hermann Schlosser.

Fellow students are always the most efficient source of solutions for every day problems. Thanks for helping me find all those bugs (some of which you introduced in the first place...), for being patient office mates and for putting me up on occasions.

Special thanks to Martin Erdmann, Dave Milstead, Peter Schleper and Markus Wobisch for many interesting and useful discussions. Last but not least I am also very grateful to Joannah Caborn for correcting my Germanisms.

Thank you all, I'd do it again anytime ...

From the moment I picked your book up until I put it down I was convulsed with laughter. Some day I intend reading it. - Groucho Marx